Prediction of the Glass Temperature and Phase Behavior of Amorphous Solid Dispersions

Zur Erlangung des akademischen Grades eines
DOKTORS DER INGENIEURWISSENSCHAFTEN (DR.-ING.)

von der KIT-Fakultät für Chemieingenieurwesen und Verfahrenstechnik des
Karlsruher Instituts für Technologie (KIT)
genehmigte

DISSERTATION

von
M.Sc. Luis Miguel Gil-Rojo
aus Manizales, Kolumbien

Tag der mündlichen Prüfung:	17.12.2024
Erstgutachterin:	Prof. Dr. rer. nat. habil. Sabine Enders
Zweitgutachterin:	Prof. Dr. rer. nat. habil. Gabriele Sadowski

Acknowledgments

This thesis was developed during my tenure as a research associate at the Institute for Technical Thermodynamics and Refrigeration at the Karlsruhe Institute of Technology from September 2020 to August 2024.

I would like to extend my deepest gratitude to my supervisor, Prof. Sabine Enders, for providing me with the opportunity to explore the glassy state, for her leadership grounded in trust and independence and for our fruitful discussions on thermodynamics. I am also thankful for the opportunities she provided to present my findings at both national and international conferences.

Additionally, I would like to express my appreciation to Prof. Gabriele Sadowski for kindly agreeing to serve as the second evaluator of this thesis.

I would also like to extend my heartfelt thanks to my colleagues David Kruppa, Simon Leube, Fabian Brettschneider-Lazaro, Robin Rees, Andreas Roth, Annika Reinhardt, Richy Bergmann, Jonas Jaske, Eric Bahne and Sebastian Rauh. Their technical insights, support during challenging moments and the positive, collaborative atmosphere they fostered at ITTK greatly enriched my experience.

I am infinitely grateful to Ana Lucía Rojo for her unconditional belief in me and her constant encouragement over the years, which gave me the strength to tackle challenges I once thought were beyond my reach.

My special thanks are extended to Orlando Gil for his financial support, which made it possible for me to pursue my studies.

Words cannot express my gratitude to Laura León for standing by my side and offering support during the most challenging times.

Last but certainly not least, I am deeply thankful to everyone who, whether directly or indirectly, played a significant role in this journey.

Karlsruhe, August 2024
Luis Miguel Gil-Rojo

Kurzfassung

Das Verständnis des Glasübergangs und des Phasenverhaltens von amorpher Polymerdispersionen (ASDs) ist entscheidend für die Entwicklung neuer pharmazeutischer Formulierungen zur Behandlung verschiedener medizinischer Zustände. Während das Phasenverhalten von ASDs bereits mithilfe von Zustandsgleichungen berechnet und vorhergesagt wurde, wird die Glastemperatur in der Regel aufgrund des Mangels an physikalisch fundierten Modellen mittels empirischer Korrelationen geschätzt. Darüber hinaus beeinflusst die Anwesenheit von Feuchtigkeit während der Verarbeitung und Lagerung von ASDs sowohl die Glastemperatur als auch das Phasenverhalten erheblich, was von empirischen Gleichungen nur unzureichend erfasst wird. Um diese Herausforderungen zu bewältigen, wurde ein neuer theoretischer Ansatz zur Vorhersage der Glastemperatur von trockenen und feuchten ASDs entwickelt, indem die allgemeine Entropietheorie (GET) mit der Sanchez-Lacombe (SL) Zustandsgleichung gekoppelt wurde.

Die GET, ursprünglich für Polymerblends entwickelt, wurde verwendet, um die Entropiedichte mit der α Relaxationszeit zu korrelieren, indem nur ein Parameter an die experimentelle Glastemperatur des jeweiligen Reinstoffes angepasst wurde. Ferner muss der in der SL Zustandsgleichung inbegriffene binäre Wechselwirkungsparameter an binäre experimentelle Gleichgewichtsdaten angepasst werden, um dann die Glastemperatur der ASD vorherzusagen. Das Modell wurde zusätzlich für ternäre Mischungen erweitert, um den Einfluss von Feuchtigkeit ohne weitere anpassbare Parameter zu berücksichtigen.

Zunächst wurden die SL Reinstoffparameter des Polymers Polyvinylpyrrolidon (PVP) und der aktiven pharmazeutischen Wirkstoffen (APIs) Indometacin (IND) und Ibuprofen (IBU) an experimentelle Druck-Volumen-Temperatur (PVT) Daten angepasst. Die SL Parameter von Naproxen (NAP) und Griseofulvin (GRI) wurden an binäre experimentelle Flüssig-Fest Gleichgewichtsdaten (SLE) in reinen organischen Lösungsmitteln angepasst. Um die Genauigkeit des neuen Ansatzes zu testen, wurde der Einfluss des Druckes auf die α Relaxation und die Glastemperatur von IND und IBU vorhergesagt und mit experimentellen Daten validiert. Außerdem wurde die Glastemperatur der trockenen ASDs bestehend aus PVP und jeweils IND, IBU und NAP vorhergesagt und mit experimentellen Daten aus der Literatur verglichen, ebenso wie der Einfluss der Feuchtigkeitsaufnahme auf den Glasübergang und das SLE von IND-PVP und NAP-PVP. Der in dieser Arbeit entwickelte Ansatz kann zur qualitativen Beschreibung der α Relaxation und zur quantitativen Beschreibung des Druckeinflusses auf die Glastemperatur von IND und IBU verwendet werden. Darüber hinaus kann mit dem Modell die Glastemperatur von trockenen ASDs bestehend aus PVP und jeweils IND, IBU und NAP in Übereinstimmung mit experimentellen Daten quantitativ vorhergesagt werden. Ferner kann mit dem Modell der Einfluss der Feuchtigkeitsaufnahme auf die Glastemperatur von IND-PVP und NAP-PVP quantitativ vorhergesagt werden.

Folglich kann der in dieser Arbeit entwickelte Ansatz verwendet werden, um die Effekte von Verarbeitungs- und Lagerungsparametern auf die Glastemperatur und das Phasenverhalten der untersuchten ASDs genau zu analysieren.

Abstract

Understanding the glass transition and phase behavior of amorphous solid dispersions (ASDs) is crucial for designing and developing new pharmaceutical formulations employed in the treatment of various medical conditions. While the phase behavior of ASDs has been already calculated and predicted using equations of state (EOS), the glass temperature is usually estimated using empirical correlations due to the lack of physically grounded models. Furthermore, the presence of moisture during processing and storage of ASDs greatly influences both the glass temperature and phase behavior, and these effects are poorly captured by empirical equations. To address these challenges, a new theoretical approach for the prediction of the glass temperature of dry and humid ASDs was developed by combining the generalized entropy theory (GET) with the Sanchez-Lacombe (SL) EOS.

The GET, originally developed for polymeric blends, has been used to correlate the entropy density with the α relaxation time by adjusting only one parameter to the experimental glass temperature of the corresponding pure component. Furthermore, the binary interaction parameter used within the SL EOS must be fitted to equilibrium binary experimental data to then predict the glass temperature of the ASD. The model was additionally expanded for ternary mixtures to account for the influence of moisture without using any further adjustable parameters.

First, the SL pure-component parameters of the polymer poly vinyl pyrrolidone (PVP) and the active pharmaceutical ingredients (APIs) indomethacin (IND) and ibuprofen (IBU) were fitted to experimental pressure-volume-temperature (PVT) data. The SL parameters of naproxen (NAP) and griseofulvin (GRI) were fitted to binary experimental solid-liquid equilibrium (SLE) data in pure organic solvents. To test the accuracy of the new approach, the influence of pressure on the α relaxation and the glass temperature of the APIs IND and IBU was predicted and validated against experimental data. Moreover, the glass temperature of the dry ASDs composed of PVP and IND, IBU and NAP, respectively, as well as the influence of moisture sorption on the glass transition and the SLE of IND-PVP and NAP-PVP was predicted and compared to experimental data taken from the literature. The new approach developed in this work may be used to qualitatively describe the α relaxation and to quantitatively describe the influence of pressure on the glass temperature of IND and IBU. Besides, the model quantitatively predicts the glass temperature of dry ASDs containing IND, IBU and NAP in agreement the experimental data. Furthermore, the developed model is capable of quantitatively predict the influence of moisture sorption on the glass temperature of IND-PVP and NAP-PVP.

Consequently, the new approach developed in this work may be used to accurately analyze the effect of processing and storage parameters on the phase behavior and glass temperature of the investigated ASDs.

Table of Contents

List of Figures

Page

List of Tables

This page is intentionally left blank.

Abbreviations

AG Adam-Gibbs model

API active pharmaceutical ingredient

APS amorphous phase separation

ARD average relative deviation

ASD amorphous solid dispersion

BCS biopharmaceutical classification system

BDS broadband dielectric spectroscopy

CAS chemical abstracts service

CRR cooperative rearrenging regions

DMA dynamic-mechanical analysis

DSC differential scanning calorimetry

EOS equation of state

FTIR Fourier transform infrared spectroscopy

GD Gibbs-DiMarzio model

GET generalized entropy theory

GRI griseofulvin

GT Gordon-Taylor equation

IBU ibuprofen

IND indomethacin

KB Kirkwood-Buff formalism

LCT lattice cluster theory

LLE liquid-liquid equilibrium

mDSC modulated differential scanning calorimetry

NAP naproxen

NELF non-equilibrium lattice fluid

NR Newton-Raphson method

NSAID nonsteoridal anti-inflammatory drug

PC-SAFT perturbed chain statistical associating fluid theory

PVP poly vinyl pyrrolidone

PVP-VA poly vinyl pyrrolidone vinyl acetate

PVT pressure-volume-temperature

RH relative humidity

SL Sanchez-Lacombe theory

SLE solid-liquid equilibrium

SLVE solid-liquid-vapor equilibrium

UV ultraviolet

VFTH Vogel-Felcher-Tamman-Hesse equation

VLE vapor-liquid equilibrium

WLF Williams-Landel-Ferry equation

XRPD X-ray power diffraction

Symbols

Latin letters

Symbol	SI-unit	Description
A	J	Free energy
A_{VFTH}	-	Constant in Vogel-Felcher-Tamman-Hesse equation (2.1)
a	$\mathrm{J\,mol^{-1}}$	Molar free energy
a_T	-	Constant in Williams-Landel-Ferry equation (2.4)
a	-	Activity
$B_{0,i}$	$\mathrm{m^3\,mol^{-1}}$	Second virial coefficient of pure i
B_{VFTH}	-	Constant in Vogel-Felcher-Tamman-Hesse equation (2.1)
B_T	K	Constant in Vogel-Felcher-Tamman-Hesse equation (2.1)
c_1	-	Constant in Williams-Landel-Ferry equation (2.5)
c_2	K	Constant in Williams-Landel-Ferry equation (2.5)
c_p	$\mathrm{kJ\,kg^{-1}\,K^{-1}}$	Specific isobaric heat capacity
E	J	Potential energy
E_a	kJ	Molar activation energy in Arrhenius equation (4.1)
f	Pa	Fugacity
$\bar{f}$	Hz	Frequency
$f_{0,i}$	Pa	Fugacity of pure component i
G	J	Free enthalpy
g	$\mathrm{J\,mol^{-1}}$	Molar free enthalpy
H	J	Enthalpy
h	$\mathrm{J\,mol^{-1}}$	Molar enthalpy
K	-	Parameter contained in the Gordon-Taylor equation (2.6) defined in equations (2.7) and (2.8)
k_B	$\mathrm{J\,K^{-1}}$	Boltzmann's constant
k_{ij}	-	Binary interaction parameter between components i and j
$k_{ij,0}$	-	Constant in temperature-dependent binary interaction parameter in equation (3.12)
$k_{ij,T}$	$\mathrm{K^{-1}}$	Constant in temperature-dependent binary interaction parameter in equation (3.12)

k_p	-	Empirical coefficient used in equation (2.11)
m	-	Fragility index defined in equation (2.2)
$\bar{M}$	$\mathrm{kg\,mol^{-1}}$	Molecular weight
N	mol	Amount of substance
N_A	$\mathrm{mol^{-1}}$	Avogadro's constant
P	Pa	Pressure
$\tilde{P}$	-	Reduced pressure
P^{LV}	Pa	Vapor pressure of mixture
$P_{0,i}^{\mathrm{LV}}$	Pa	Vapor pressure of pure component i
P^*	Pa	Characteristic pressure in the Sanchez-Lacombe theory equation of state
$\dot{Q}$	mW	Heating or cooling rate
R	$\mathrm{J\,mol^{-1}\,K^{-1}}$	Universal gas constant
r	-	Segment number in the Sanchez-Lacombe theory
r_i^0	-	Segment number of pure component i in the Sanchez-Lacombe theory
S	$\mathrm{J\,K^{-1}}$	Entropy
s	$\mathrm{J\,mol^{-1}\,K^{-1}}$	Molar entropy
$\tilde{s}$	-	Reduced entropy
s^*	$\mathrm{J\,mol^{-1}\,K^{-1}}$	Entropy per segment in Adam-Gibbs model (2.10)
S_ρ	$\mathrm{J\,K^{-1}\,m^{-3}}$	Entropy density in the generalized entropy theory (2.11)
S_ρ^*	$\mathrm{J\,K^{-1}\,m^{-3}}$	Maximal entropy density in the generalized entropy theory (2.11)
T	K	Temperature
t	s	Time
$\tilde{T}$	-	Reduced temperature
T^*	K	Characteristic temperature in the Sanchez-Lacombe theory
T_A	K	Arrhenius temperature
T_G	K	Glass temperature
T_I	K	Crossover temperature
T_K	K	Kauzmann temperature
T_{mid}	K	Middle-point temperature defined in Figure 2.5
T_{on}	K	Onset temperature defined in Figure 2.5

T_{off}	K	Offset temperature defined in Figure 2.5
T_s	K	Reference temperature in Williams-Landel-Ferry equation (2.4)
T_0	K	Constant in Vogel-Felcher-Tamman-Hesse equation (2.1)
$T_{0,i}^{\mathrm{SL}}$	K	Fusion temperature of pure component i
V	m^3	Volume
V_{corr}	m^3	Correlation volume
v	$\mathrm{m}^3\,\mathrm{mol}^{-1}$	Molar volume
$v_{0,i}$	$\mathrm{m}^3\,\mathrm{mol}^{-1}$	Molar volume of pure component i
$\tilde{v}$	-	Reduced volume
$\bar{v}$	$\mathrm{m}^3\,\mathrm{mol}^{-1}$	Molar partial volume
w	-	Mass fraction
x	-	Molar fraction
Z	-	Partition function
z	-	Size of the cooperative rearrenging regions in Adam-Gibbs model
z^*	-	Critical size of the cooperative rearrenging regions in Adam-Gibbs model

Greek letters

Symbol	SI-unit	Description
$\Delta_{\mathrm{SL}}\bar{c}_{p,0,i}$	$\mathrm{kJ\,mol}^{-1}\,\mathrm{K}^{-1}$	Difference in the molar isobaric heat capacity of pure component i across the melting line
$\Delta_{\mathrm{SL}}h_{0,i}$	$\mathrm{kJ\,mol}^{-1}$	Molar fusion enthalpy of pure component i
ΔE	$\mathrm{J\,mol}^{-1}$	Molar activation energy of α relaxation
$\Delta\mu$	J	Activation energy of α relaxation in Adam-Gibbs theory
ϵ^*	$\mathrm{J\,mol}^{-1}$	Energy parameter in the Sanchez-Lacombe theory
η	Pa s	Dynamic (shear) viscosity
κ_T	Pa^{-1}	Isothermal compressibility
μ	$\mathrm{J\,mol}^{-1}$	Chemical potential
ρ	$\mathrm{kg\,m}^{-3}$	Specific density
$\rho_{0,i}$	$\mathrm{kg\,m}^{-3}$	Specific density of pure component i
$\tilde{\rho}$	-	Reduced density

ρ^*	$\mathrm{kg\,m^{-3}}$	Characteristic (close-packed) density in the Sanchez-Lacombe theory
$\hat{\rho}$	$\mathrm{mol\,m^{-3}}$	Molar density
τ	s	Relaxation time
τ_0	s	Constant in Vogel-Felcher-Tamman-Hesse equation (2.1) or Arrhenius equation
υ^*	$\mathrm{m^3\,mol^{-1}}$	Close packed volume in the Sanchez-Lacombe theory
ϕ	-	Volume fraction
ϕ^0	-	Segment fraction
φ	-	Relative humidity
Ω	-	Total number of configurations

Subscripts and superscripts

Symbol	Description
α	α relaxation process
β	β relaxation process
c	Critical quantity
$calc$	Calculated value
E	Excess quantity
exp	Experimental value
$gl.$	Glassy state
i, j, k	Component
L	Liquid phase
max	Maximal value
mix	Property of the mixture
S	Solid phase
V	Vapor phase

1 Introduction

Glasses are everywhere to be found in modern society and infrastructure ranging from common windows, tableware, lamps and decoration up to specialized equipment such as lenses, laboratory instruments and kitchen appliances. These type of glasses are in their majority made from oxides of the elements Si, B, Al among many others and mixed with additives such as lime to modify their physicochemical properties depending on the application. Moreover, glasses can be made of polymers, metals, biomolecules, and in principle of any known substance, provided that the cooling rate during their production is high enough to avert crystallization [1].

Although glasses appear to be a solid and posses solid-like mechanical properties, their molecular structure is amorphous and rather liquid-like [1]. Strictly speaking, a glass is still flowing over time, however, its viscosity is so high that it can be regarded as a solid for any practical purpose, given that its application takes place far below from the glass transition temperature, T_G [1], as is the case for silicate-based glasses [2]. The knowledge of T_G is therefore of utmost importance in applications where T_G may be near the ambient temperature as is the case for many pharmaceuticals, e.g. [3–5].

Such pharmaceutical compounds, known in the literature as active pharmaceutical ingredients (APIs), can crystallize into different polymorphs and may also build glasses, depending on the processing conditions [6, 7]. Since the amorphous form of the API has a higher solubility than the crystalline form, e.g. [8], enabling dissolution of the drug in amorphous form will improve its bioavailability after oral administration [6]. However, using the amorphous form of an API is challenging due to its metastable nature and tendency to recrystallize [6, 7]. Therefore, an additional component with a T_G higher than the ambient temperature can be used to form a mixture with the API and kinetically hinder their molecular movement, so that a potential recrystallization of the drug can be avoided [6, 7]. The additional component used to form the aforementioned mixtures, known as amorphous solid dispersions (ASDs), is usually an amorphous polymer with negligible crystallinity, since these polymers exhibit great glass-forming ability, e.g. [9], and some of them may be used in pharmaceutical applications or are even already commercially available, e.g. [10, 11].

Even though ASDs improve the bioavailability of poorly water soluble APIs, e.g. [6, 10, 12, 13], there are still some drawbacks associated with their use such as a lower physical stability, e.g.[12, 14], and the potential formation of glass suspensions [6], also known in the literature as amorphous phase separation (APS). The APS, which thermodynamically represents a liquid-liquid equilibrium (LLE), can be induced by the presence of moisture and has already been predicted, e.g. [15–18], using equations of state such as the perturbed chain statistical associating fluid theory (PC-SAFT) [19]. The presence of an LLE in a given ASD is undesired, since the API-rich phase can quickly recrystallize due to its lower T_G [6].

For instance, the isobaric phase diagram of an arbitrary ASD with non-negligible crystal solubility of the API in the polymer is qualitatively shown in Figure 1.1.

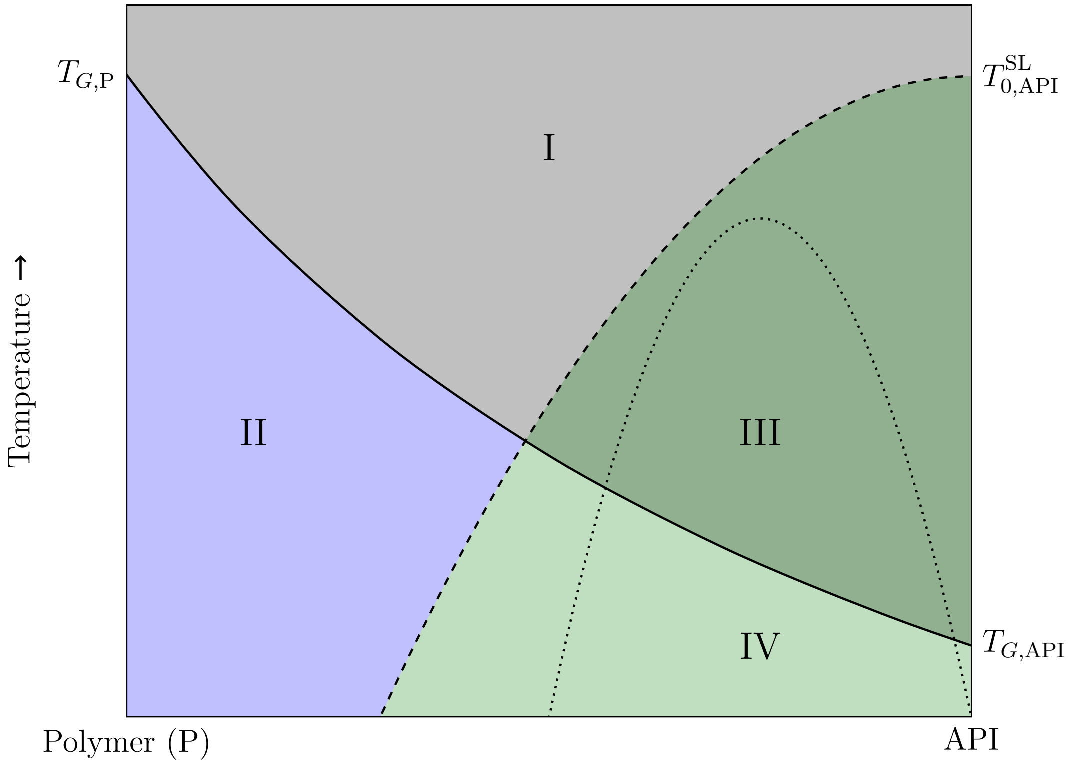

Figure 1.1: Schematic isobaric phase diagram of ASDs adapted from Prudic et al. [20]. Glass temperature (—), solid-liquid equilibrium (SLE) (– –) and possible LLE (···). $T_{G,i}$ denotes the glass and $T_{0,i}^{\mathrm{SL}}$ the fusion temperature of component i, respectively. Region I in gray denotes the stable liquid state, region II in blue the metastable glassy state, region III in dark green the meta- and unstable liquid state and region IV in light green the meta- and unstable glassy state.

The ASD is in a thermodynamically stable liquid state in region I, where both the polymer and the API are completely miscible. In region II, the polymer and the API are still completely miscible in the liquid phase, however, the ASD is kinetically hindered for every temperature below T_G. Consequently, after some time at constant temperature, the ASD must relax towards the corresponding thermodynamically metastable liquid state. On the other hand, in regions III and IV, the ASD is thermodynamically either metastable or unstable for all temperatures below the SLE line. In region III, the API recrystallizes and forms a solid phase containing only the API, as the polymer and API are completely inmiscible in the solid phase. In region IV, the API must recrystallize at a much lower rate than in region III, since the relaxation time of the ASD is greater in the glassy state below the solid black line in Figure 1.1. Furthermore, an LLE can be present in the dry ASD or be induced by moisture absorption as explained in section 2.2. The LLE region shown in Figure 1.1 must not be necessarily encapsulated under the SLE line and may be also present in region I. This last case is undesirable in pharmaceutical applications, as the ASD will separate into one API-rich and one API-poor phase modifying the intended correct dosage.

To this date, there are no physically grounded models available in the literature to predict the glass temperature of the ASD and only empirical correlations such as the Gordon-Taylor equation (GT) [21] are used instead. This empirical approach slows down the development of new potential pharmaceutical formulations and is more expensive, since the glass temperature of the ASD as a function of the drug load needs to be experimentally measured. The T_G of pure components can be theoretically calculated with an equation of state (EOS) via the generalized entropy theory (GET) [9, 22] by relating the entropy density to the relaxation time of the component as explained in detail in section 3.2. The GET requires an EOS capable of accurately describing the entropy of the system and its compressibility, such as the Sanchez-Lacombe theory (SL) [23, 24]. In the framework of the SL EOS, the polymer and the API are divided into equally large segments, respectively, and their thermodynamic properties are derived using statistical mechanics as explained in detail in section 3.1.

To close the knowledge gap regarding the theoretical prediction of the T_G, the main aim of this work consists on developing a physical model to predict the glass temperature and phase equilibria of dry and humid ASDs using the GET and the SL EOS. To achieve the main goal, four tasks are required. First, the SL parameters of the pure components forming the ASDs need to be fitted to suitable experimental data. For this purpose, the polymer poly vinyl pyrrolidone (PVP) and the APIs griseofulvin (GRI), ibuprofen (IBU), indomethacin (IND) and naproxen (NAP) were selected, since there is enough experimental data in the literature to adjust the SL parameters as explained in detail in section 3.5. Second, the glass temperature of the pure components and its pressure dependence need to be calculated by using the SL EOS within the GET framework as explained in detail in section 3.2. Third, the T_G of the dry ASDs needs to be predicted as explained in section 3.2 after fitting the binary interaction parameter contained in the SL EOS to suitable equilibrium binary data. Finally, the SL EOS needs to be expanded to ternary mixtures as explained in section 3.1 to predict the T_G and phase equilibria of the humid ASDs. It is worth mentioning that no further adjustable parameters were used to describe the ternary mixtures using the SL EOS and the binary interaction parameters were never fitted to the experimental glass temperature of the binary or ternary systems.

This work is structured as follows: A brief overview of what has already been done in the literature such as a brief description of the pure components used is given in chapter 2. Then, an explanation of the models and calculation approaches is presented in chapter 3. Subsequently, the core of this work is outlined in chapter 4, where the obtained results are divided into pure components, dry and humid ASDs. Finally, the most important insights derived from the results are summarized in chapter 5, whereas further key aspects requiring future investigation are also mentioned. The main focus of this thesis resides in the theoretical description of the glass transition from a thermodynamic perspective. Thus, even though pharmaceutical formulations are an important aspect, they are only used as a practical application of the developed model.

2 Background

In this chapter, a brief summary of key concepts regarding the glass transition and its empirical and theoretical description is first presented in section 2.1. Then, a description of the pure components used such as of amorphous solid dispersions and their advantages, challenges and current research topics is presented in section 2.2. Finally, a brief description of the experimental methods employed to estimate the reported data used in this work is presented in section 2.3.

2.1 Glass transition

In this section, a brief overview of the glassy state and the glass transition is given. First, basic concepts regarding the glass transition and the properties of glassy materials is given in section 2.1.1. Furthermore, the description of the relaxation of pure components such as the glass temperature of pure components and mixtures using empirical correlations is briefly elucidated in section 2.1.2. Thereafter, the theoretical descriptions of the glass transition proposed by Gibbs and DiMarzio [25] and Adam and Gibbs [26] are discussed in sections 2.1.3. Finally, the main characteristics of the GET [9, 22] used in this work and derived from the Gibbs-DiMarzio model (GD) and Adam-Gibbs model (AG) are briefly presented in section 2.1.4.

2.1.1 Fundamentals

First of all, the definition of the word “glass” needs to be settled. Commonly, glass is associated with several objects found in everyday life such as windows, bottles, laboratory and medical equipment, lenses, house decorations and all kinds of containers. These objects are usually made of silicate glasses produced from silicon dioxide and other excipients added to modify their physical properties according to the required application. However, in this work, the term glass refers to a metastable thermodynamic state of matter which polymers, pharmaceuticals and in principle any pure substance can attain under the right conditions [1]. Consequently, this interesting yet enigmatic glassy state needs to be precisely defined prior to its investigation, which unfortunately is no trivial task. For this purpose, the total volume of a pure substance as a function of temperature under constant pressure is schematically shown in Figure 2.1.

Lets assume that the pure substance can crystallize and exhibits a positive thermal expansion coefficient, as is the case for the pharmaceuticals studied in this work and presented in section 2.2. Initially, a defined mass of the pure substance is in a stable liquid state characterized by any point on the solid black line at $T > T_{0,i}^{\mathrm{SL}}$ shown in Figure 2.1. Then, the substance is carefully cooled down at a very low cooling rate until the fusion temperature, $T_{0,i}^{\mathrm{SL}}$, is reached, i.e. the intersection between the dashed and solid black lines in Figure 2.1. During this first cooling step, the total volume of the substance continuously decreases and its specific density increases, since the mass is constant. Upon reaching the fusion temperature at a very low cooling rate, crystals begin to form at constant temperature until the whole sample has fully crystallized and a stable solid phase is formed. Thereafter and upon further cooling, the temperature and the total volume gradually decrease along the horizontal dashed black line shown in Figure 2.1, however, the rate at which the volume decreases with temperature is usually lower than in the liquid state [1]. The fusion enthalpy can be estimated by calculating the amount of energy released by the sample alongside the vertical dashed black line. Thus, the crystallization event of a pure substance may be characterized by both the fusion temperature and enthalpy as explained in section 2.3.3.1, which are unique to the corresponding polymorphic form of each pure component, given that it can crystallize.

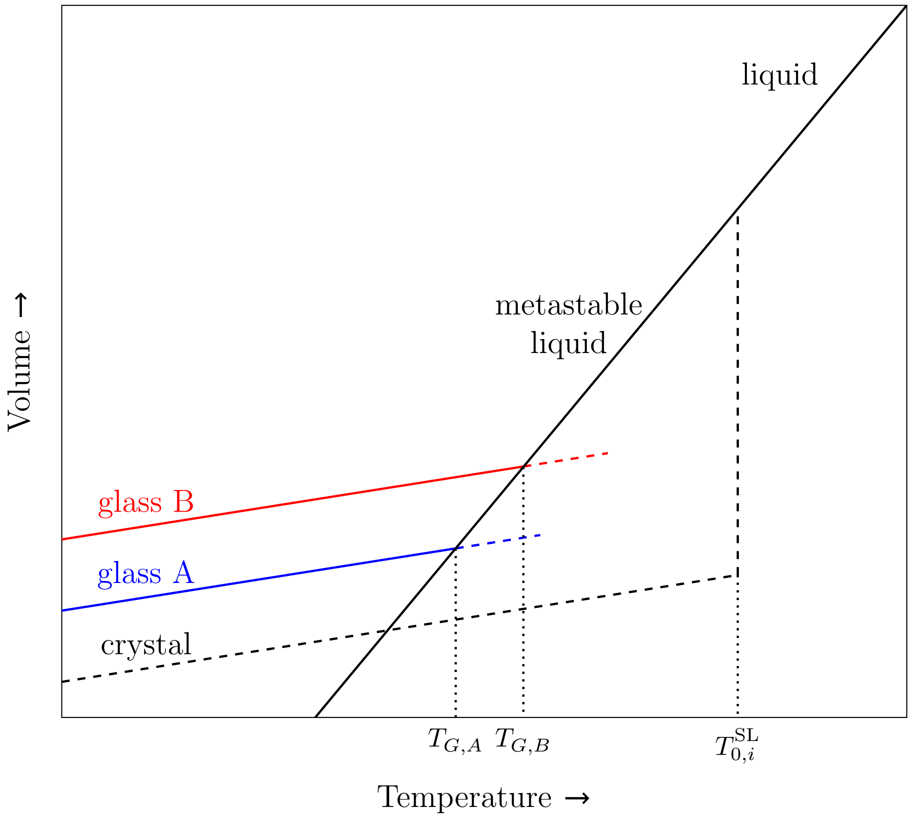

Figure 2.1: Isobaric volume change of a pure substance across the fusion and glass temperatures adapted from Debenedetti [27]. The (—) line describes the volume decrease by averting crystallization, the (– –) line describes the volume decrease including complete crystallization, the (—) line describes the volume decrease of the glass formed using the cooling rate $\dot{Q}_B$ and the (—) line describes the volume decrease of the glass formed using the cooling rate $\dot{Q}_A$. Given that both glasses, A and B, were formed upon cooling under the same constant pressure, the cooling rates at which the glasses were formed obey $\dot{Q}_A < \dot{Q}_B$. T_G denotes the glass temperature of the corresponding glass and $T_{0,i}^{\mathrm{SL}}$ the fusion temperature of the pure substance.

Lets repeat the previous thought experiment beginning again from a stable liquid state, however, increasing the cooling rate to a value $\dot{Q}_A$, so that no crystals can form upon reaching the fusion temperature. In this case, the volume further continuously decreases below the fusion temperature along the solid black line in Figure 2.1 [1]. This thermodynamic state is known as a metastable (also supercooled) liquid, since the substance eventually has to reach its equilibrium solid state found on the dashed black line in Figure 2.1 at the same temperature [1]. Upon further cooling of the sample at $\dot{Q}_A$ through the metastable liquid state, a point is reached where the slope of the volume-temperature diagram clearly changes over a narrow temperature range [1] and the glass A characterized by the solid blue line shown in Figure 2.1 is formed [1, 28]. It must be pointed out that the change in the slope occurs within a temperature range [1] and not at a well-defined value as is the case for the crystallization event. Nonetheless, a single temperature value known as the glass transition temperature, T_G, is calculated from the measured data using different approaches as exemplary explained in section 2.3.3.1. Furthermore, the slope at which the volume changes with temperature is both for the crystal and glass A very similar and lower than the slope of the corresponding liquid [1].

Upon repeating the aforementioned experiment using an even higher cooling rate $\dot{Q}_B$, the glass temperature reached, $T_{G,B}$, is higher than the one attained using the lower cooling rate $\dot{Q}_A$, provided that crystallization is still averted [1]. Therefore, the measured T_G depends on the cooling rate used in the experiment [1, 28, 29] and it has undoubtedly both a thermodynamic and kinetic nature as exhaustively explained by Debenedetti [1]. Besides, it becomes clear why glasses possess a thermal history which depends on the cooling rate and method used in their production [1]. For instance, the specific density of the solid phase is highest followed by glass A and B, respectively, if compared at the same temperature as shown in Figure 2.1. Thus, the mechanical properties evaluated at the same temperature and pressure conditions of two glasses produced from the same substance may differ from one another depending on the method and conditions used in obtaining the glasses. Consequently, special care needs to be taken when comparing the properties of glasses produced from the same substance using different techniques and operating conditions.

The behavior shown in Figure 2.1 also means that a glass maintains the volume and molecular structure of the liquid from which it was formed, however, the changes in the volume with temperature and pressure are similar in magnitude to those of the crystalline solid [30]. The natural question arises as to how long it takes the glass to relax to its equilibrium crystalline state. For instance, regular household glassware made of silicate glass is used about 500 °C below its T_G and makes it stable for all designed practical purposes [2]. Consequently, the relaxation time of glasses is so large that it is not possible to experimentally observe its relaxation on experimental time scales [28]. The relaxation time can be measured using, for instance, broadband dielectric spectroscopy (BDS) as briefly described in section 2.3.3.2. From the experimental relaxation time obtained, it is possible to calculate the glass temperature by fitting the data to empirical equations such as the Vogel-Felcher-Tamman-Hesse equation (VFTH) [31–33] or Williams-Landel-Ferry equation (WLF) [34, 35] as explained in section 2.1.2. However, the relaxation time at the glass temperature needs to be previously defined. Pragmatically, T_G is defined as the temperature at which the shear viscosity, η, is equal to 1×10^{12} Pa s [36], i.e. the relaxation time is within the experimental time scale and equal to 100 s [36, 37]. For instance, the relaxation time around the fusion temperature is in the order of a few picoseconds, 14 orders of magnitude lower than near T_G [28]. Consequently, it can be said that a glass is a liquid frozen in experimental time scales that behaves mechanically like a solid [1, 38]. Strictly speaking, several relaxation processes can be observed experimentally depending on the frequency at which the experiment is carried out [39]. However, the glass temperature is associated to the α (also known in the literature as primarily, slow or segmental) relaxation process. Therefore, the relaxation time mentioned throughout this work is always related to the α process and denoted as τ_α unless otherwise explicitly stated.

Another important concept regarding the glass transition is the temperature at which the metastable liquid line (solid black) shown in Figure 2.1 intercepts the crystalline line (dashed black), given that no glass is formed and the entropy instead of the volume is plotted on the y-axis. This conceptual yet experimentally inaccessible temperature is known as Kauzmann's temperature, T_K [1, 40]. The implication of an amorphous disordered phase having the same entropy as the crystalline ordered phase at the same temperature and pressure is odd enough, yet not forbidden by thermodynamics [1]. However, assuming that the extrapolation of both the metastable and crystalline lines is valid and the formed crystal is perfect (zero entropy at $T = 0\,\mathrm{K}$), there must be a positive value of the temperature at which the metastable liquid phase exhibits a negative entropy value, which is thermodynamically impossible [1]. An extensive discussion of the roots and implications of Kauzmann's temperature can be found elsewhere, e.g. [1, 41].

On the other hand, polymers with negligible crystallinity, such as PVP [42–45], do not exhibit a crystallization event and eventually form glasses upon isobaric cooling from the melt [38]. The glass transition of polymers using different operational conditions was studied in detail for instance by McKinney and Goldstein [46]. Consequently, the volume evolution of a polymer with negligible crystallinity cooled down isobarically from the melt is described by Figure 2.1 after completely removing the dashed black line. As for non-polymeric substances, the lower the cooling rate, the lower the glass temperature and the higher the specific density of the glass.

Extensive and comprehensive explanations of the aforementioned and further topics can be found in the literature, for instance, regarding the physicochemical roots of the glass transition [29], theoretical models to describe the glass transition [28], relaxation in complex systems [47, 48], metastable states including the glassy state [1], the dynamics and thermodynamics of polymer glasses [38] and glass aging [2].

2.1.2 Empirical equations

In this section, the empirical equations used in this work to predict the relaxation time of pure components and the glass temperature of dry and humid ASDs are briefly introduced.

2.1.2.1 Vogel-Fulcher-Tammann-Hesse

The VFTH equation [31–33] describes the behavior of the viscosity, η, of a material as a function of temperature. The VFTH equation [31–33] can also be used to describe the relaxation time, τ_α, via [49]

$$\tau_\alpha = \tau_0 \exp\left(\frac{B_T}{T - T_0}\right), \tag{2.1}$$

where A_{VFTH}, B_{VFTH} and T_0 are material-specific constants. Care must be taken when performing calculations with reported values of the constant B_T in equation (2.1). Since the term $1/\ln(10)$ appears multiplying the second expression on the rhs of equation (2.1) after applying the decimal logarithm, some authors report the fitted parameter B_T already containing this factor and others do not include it. As pointed out by Hodge [50], defining the parameter $B_T = DT_0$ in equation (2.1) implies that it cannot mathematically reduce to the Arrhenius form when $T_0 = 0\,\mathrm{K}$. Therefore, in this work, B_T is always reported as a constant and not as a function of T_0, even though the original authors who fitted the parameters may have separately reported the magnitudes D and T_0 in equation (2.1).

A popular way introduced by Angell [49] of characterizing liquids according to their ability to form glasses, is to use the fragility index defined as the slope of the relaxation time on the so called Arrhenius plot $\log_{10}\tau_\alpha$ vs T_G/T evaluated at T_G and mathematically defined as

$$m = \left.\frac{d\log_{10}\tau_\alpha}{d(T_G/T)}\right|_{T=T_G}. \tag{2.2}$$

The fragility index can be calculated from equation (2.1) by applying the definition as

$$m = \frac{B_T}{T_G(\ln 10)\left(1 - T_0/T_G\right)^2}. \tag{2.3}$$

The reported fragility indexes used in this work were calculated from VFTH parameters fitted exclusively to α relaxation times, since determining it from heat capacity measurements is disputed [51]. Furthermore, the form of the VFTH equation (2.1) in terms of the relaxation time is used throughout this work in spite of the form including the viscosity, since the viscosity of polymers depends on the polydispersity, the molecular weight distribution and the shear rate. Thus, the Arrhenius plot $\log_{10}\eta$ vs T_G/T should be avoided for polymers [52].

2.1.2.2 Williams-Landel-Ferry

The WLF equation [34, 35] was derived from the VFTH equation [31–33] as

$$\log_{10} a_T = \frac{-c_1(T - T_s)}{c_2 + T - T_s}, \tag{2.4}$$

where $a_T = \tau_\alpha(T)/\tau_\alpha(T_s)$, T_s is a reference temperature and c_1, c_2 are constants. Several temperatures can be chosen as the reference temperature [9], however, the glass temperature is the most popular option, since the relaxation time at T_G was set to be 100 s to describe the overlapping of the molecular relaxation and experimental time scales. Therefore, the WLF equation can be written as

$$\log_{10}\left[\frac{\tau_\alpha(T)}{\tau_\alpha(T_G)}\right] = \frac{-c_1(T - T_G)}{c_2 + T - T_G}. \tag{2.5}$$

Even tough the WLF equation describes the relaxation time of a large number of substances taking T_G as the reference temperature, $c_1 = 17.44$ and $c_2 = 51.6\,^{\circ}\mathrm{C}$ [35], the "universality" of the constants is disputed [26, 53]. For instance, Dudowicz et al. [53] pointed out that both constants, c_1 and c_2, depend on the chosen reference temperature. Thus, they cannot be universal, since the experimental glass temperature depends on the conditions used, i.e. heating/cooling rate in differential scanning calorimetry (DSC) experiments.

2.1.2.3 Gordon-Taylor

The GT equation [21] was developed to describe the glass temperature of copolymers by treating them as solutions of small molecules, as a function of the glass temperature, $T_{G,i}$, and the glassy densities, $\rho_i^{gl.}$, of the pure polymers i and j respectively formed from the monomeric units conforming the copolymer as

$$T_G = \frac{\mathrm{w}_i T_{G,i} + K \mathrm{w}_j T_{G,j}}{\mathrm{w}_i + K \mathrm{w}_j} \tag{2.6}$$

where K is defined as

$$K = \frac{\rho_{0,i}^{gl.} T_{G,i}}{\rho_{0,j}^{gl.} T_{G,j}}, \tag{2.7}$$

and w_i denotes the mass fraction of component i in the mixture. Since its introduction, the GT equation has been widely applied in the literature to predict the T_G of ASDs, e.g. [3, 43, 54–63]. Furthermore, the GT equation (2.6) can be expanded to ternary mixtures [64] composed of components i, j and k to account for humidity in the ASDs, e.g. [16], or the T_G of pharmaceuticals in the presence of excipients, e.g. [64], as

$$T_G = \frac{\mathrm{w}_i T_{G,i} + K_{ij} \mathrm{w}_j T_{G,j} + K_{ik} \mathrm{w}_k T_{G,k}}{\mathrm{w}_i + K_{ij} \mathrm{w}_j + K_{ik} \mathrm{w}_k} \tag{2.8}$$

whereas

$$K_{ij} = \frac{\rho_{0,i}^{gl.} T_{G,i}}{\rho_{0,j}^{gl.} T_{G,j}} \quad \text{and} \quad K_{ik} = \frac{\rho_{0,i}^{gl.} T_{G,i}}{\rho_{0,k}^{gl.} T_{G,k}}. \tag{2.9}$$

Equations (2.6) and (2.8) were used to calculate the T_G of ASDs shown in sections 4.2 and 4.3, respectively. The pure component parameters used alongside the reference from which they were taken are cited in the corresponding sections.

2.1.3 Gibbs-DiMarzio and Adam-Gibbs theories

There are several approaches to address the theoretical description of the glass transition using physically grounded models as described in detail elsewhere, e.g. [1, 52, 65] and references therein. In this section, the Gibbs-DiMarzio model (GD) [25] and Adam-Gibbs model (AG) [26] are briefly elucidated, since the generalized entropy theory (GET) [9, 22] used in this work was mainly derived by employing concepts from these two models. Following the classification proposed by Debenedetti [1], the GD and AG theories belong to the thermodynamic viewpoint to address the glass transition, since they both use the configurational entropy as the key magnitude to explain the transition.

The configurational entropy in the framework of the GD model [25] is assumed to be the portion of the total entropy due to the different configurations available to a system and neglecting any vibrational contributions. However, the term configurational entropy is actively avoided throughout this work, since the definition of the total entropy of a system after Boltzmann arises from the different number of configurations available to the system, i.e. the same magnitude used in the GD model [25]. The term entropy mentioned in this work is therefore always related to Boltzmann's definition, unless otherwise explicitly stated. GD [25] used lattice calculations employing concepts originally proposed by Meyer [66, 67], Huggins [68] and Flory [69] to derive an expression of the free energy of a pure monodisperse polymer. The obtained expression for the free energy in the GD model [25] differs from that proposed by Flory [69] in two important aspects; first, the inclusion of holes in the lattice construction to account for effects due to the compressibility of the system and second, the use of a more exact expression, originally proposed by Huggins [70], to calculate the expectancy that a specified site is available to a chain segment after several molecules have been already placed on the lattice. The entropy can be then obtained in the classical way as the temperature derivative of the free energy [25]. Furthermore, GD associated the experimentally observed glass temperature to their [25] predicted second-order transition [71] temperature, T_2. According to GD, the entropy becomes exactly zero at T_2, when the polymer fluid is cooled isobarically from the melt [25]. Therefore, there are two different expressions to calculate the entropy [25], avoiding Kauzmann's paradox [40]. Accordingly, GD regarded the glass temperature as the point at which the number of configurations available to the system dramatically decreases to exactly only one possible available configuration [25]. An extensive discussion of the advantages and disadvantages such as the inherent assumptions made by GD is presented elsewhere, e.g. [9].

On the other hand, the AG theory correlates the relaxation time of the system with the entropy via the cooperative rearrenging regions (CRR) [26]. A CRR is a subsystem of the sample which can rearrange into another configuration independently of its environment, given that the required enthalpy fluctuation also takes place [26]. At T_G, the size of the CRR, z, must be equal to the whole sample or at least a macroscopic portion of it, since the available configurations must be equal to one, as already pointed out by Gibbs and DiMarzio [25]. After a statistical mechanical derivation departing from the isothermal-isobaric ensemble and differentiating between the number of subsystems able and those unable to undergo a transition as explained in detail by Adam and Gibbs [26], a critical lower size of the CRR which can undergo a transition at all, z^*, is obtained [26]. Furthermore, z^* is inversely proportional to the entropy of the system, S, and directly proportional to the entropy per segment, s^* [26]. It must be pointed out that even though AG did not state a value for s^*, they did mention that a system must have at least two configurations available for a transition to take place at all [26]. Therefore, a value can be estimated by using Boltzmann's equation for the entropy, however, this value is not universal for all species as originally implied by Adam and Gibbs [26] and explained in detail by Johari [72]. Finally, since the relaxation time, τ_α, is inversely proportional to the average probability of a transition, the well-known AG equation [26]

$$\tau_\alpha = \tau_0 \exp\left(\frac{\Delta\mu z^*}{k_B T}\right) \quad \text{with} \quad z^* = \frac{N_A s^*}{s}, \tag{2.10}$$

is obtained. In equation (2.10), τ_0 denotes a factor whose dependence on temperature is negligible compared to the exponential term and $\Delta\mu$ denotes the potential energy hindering the cooperative rearrangement per segment [26]. A detailed discussion regarding the advantages, disadvantages, successes and challenges of the AG theory can be found elsewhere, e.g. [1, 9, 73]. Furthermore, it must be pointed out that the AG relation may be converted into the WLF equation as shown by Adam and Gibbs [26] themselves and into the VFTH equation as shown for instance by Angell [74]. Consequently, the AG equation (2.10) explained for the first time the empirical relations used to describe the relaxation of pure fluids by employing a physically grounded approach. It must be pointed out that experimental data on the relaxation of the system is required to use equation (2.10) to calculate the glass temperature. AG [26] used for instance the calculations obtained with the WLF equation (2.5) to estimate the order of magnitude of $\Delta\mu$ using $s^* = k_B \ln 2$ as a first approximation.

2.1.4 Generalized entropy theory

The generalized entropy theory (GET) was first developed to theoretically explain the glass transition of pure polymers by Dudowicz et al. [22] and was later explained in more detail by Dudowicz et al. [9]. Then, Dudowicz et al. [75] presented some advances in the mathematical tractability of the theory and references to previous applications. In general terms, the GET uses the concepts presented by GD [25] to evaluate the entropy of the system using the lattice cluster theory (LCT) [76–79] to then apply the AG equation (2.10) [26] to calculate the relaxation time [9, 22]. However, Dudowicz et al. [9, 22] used the entropy density rather than the entropy in the AG equation (2.10) [26] to also account for the compressibility of the system and suggested a way to calculate $\Delta\mu$ in equation (2.10) so that the T_G can be predicted. A schematic representation of the isobaric change of the reduced entropy, dashed line, and the reduced entropy density, solid line, over the temperature is shown in Figure 2.2.

The reduced entropy is a monotonic function of temperature which always increases with temperature at constant pressure, unlike the reduced entropy density which exhibits a maximum as explained in detail by Dudowicz et al. [9, 22]. Furthermore, three characteristic temperatures can be identified by comparison with experimental data, as explained in detail by Dudowicz et al. [9], from the plot of the reduced entropy density over the temperature at constant pressure [9, 22] as shown in Figure 2.2.

The crossover temperature, T_I, is defined as the inflection point of the temperature times the reduced entropy density over the temperature and the Arrhenius temperature, T_A, is defined as the temperature value at which the reduced entropy density is maximal [9, 22].

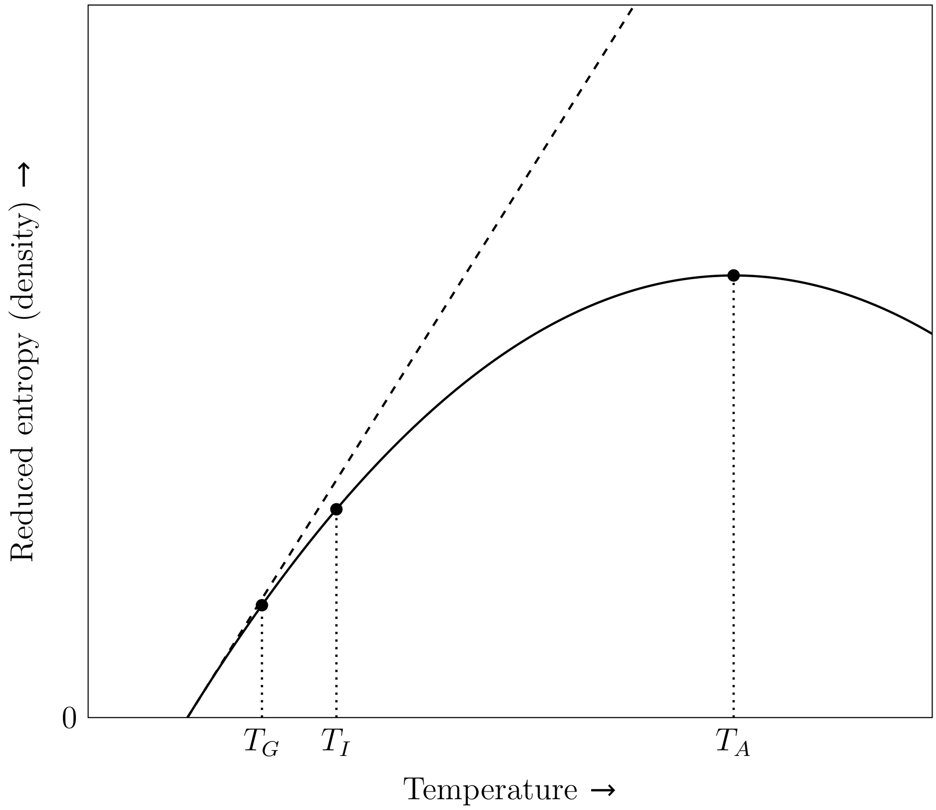

Figure 2.2: Schematic isobaric change in the reduced entropy (– –) and entropy density (—) over the temperature adapted from Dudowicz et al. [9]. T_G denotes the glass temperature, T_I the crossover temperature and T_A the Arrhenius temperature.

The glass temperature can be then calculated at $\tau_\alpha = 100\,\mathrm{s}$ from equation (2.11) as [9]

$$\tau_\alpha = \tau_0 \exp\left(\frac{\Delta\mu S_\rho^*}{k_B T S_\rho}\right) \quad \text{and} \quad \frac{\Delta\mu}{k_B} = k_p T_I, \tag{2.11}$$

whereas S_ρ^* denotes the maximal entropy density at T_A, $\tau_0 = 10^{-13}\,\mathrm{s}$ and $k_p \approx 6$. The value of $k_p \approx 6$ in equation (2.11) is an empirical relation for polymers which arised from comparisons to experimental data as explained in detail by Dudowicz et al. [80]. Another approach used to calculate the activation energy is to fit the coefficient k_p in equation (2.11) to match the experimentally measured glass temperature as already performed by Roericht [81]. Furthermore, a physical interpretation of the characteristic temperatures shown in Figure 2.2 is given in detail by Dudowicz et al. [9]. For instance, T_I denotes the temperature at which the relaxation time exhibits changes in its behavior over the temperature [9], whereas T_A denotes the onset temperature of glass formation in a polymer melt [9].

The GET was applied by Dudowicz et al. [82] to predict the T_G of blends composed of model polymers. For this purpose, the concentration fluctuations in the blend were considered [82] by using the Kirkwood-Buff formalism (KB) [83] in reverse as first proposed by Ben-Naim [84]. The KB formalism [83] correlates the integral of the radial distribution function to thermodynamic properties which can be computed from a thermodynamic model. Dudowicz et al. [82] used the LCT EOS to calculate both the KB integrals and the entropy density required within the GET framework. On the other hand, Roericht [81] independently used the SL and the PC-SAFT EOS to predict the T_G of various polymeric and copolymeric blends in agreement with experimental data. In these approaches [81, 82], the correlation length needs to be calculated using properties available from the EOS and the Kuhn lengths of the polymers which need to be either assumed or experimentally estimated. Since the Kuhn length is defined only for polymeric molecules, these approaches [81, 82] cannot be applied to mixtures containing APIs. The procedure used in this work to circumvent the Kuhn length issue is explained in detail in section 3.2.

2.2 Amorphous solid dispersions

APIs are classified in the biopharmaceutical classification system (BCS) after their solubility and gastrointestinal permeability in four classes as first proposed by Amidon et al. [85]. Class I APIs are both classified as highly soluble and permeable, class II are lowly soluble and highly permeable, class III highly soluble and lowly permeable and class IV both lowly soluble and permeable [85]. Depending on this classification, pharmaceutical formulations may be produced using different techniques. In this work, formulations containing only class II APIs, which may represent up to 70 % of formulations in development [6], are further investigated.

The bioavailability, defined as the fraction of an orally administered pharmaceutical formulation that reaches the systemic circulation, of class II APIs may be limited either by their solubility or their dissolution rate [6]. Furthermore, the solubility of APIs in crystalline form is in principle lower than that of the amorphous form [8]. Thus, ensuring that the API dissolves in amorphous rather than in its crystalline form will improve the bioavailability of class II pharmaceuticals [6, 7]. Unfortunately, the amorphous form of APIs is thermodynamically metastable and prone to relax towards its stable state, the crystalline form, e.g. [1, 86], known in the literature as recrystallization. One way of circumventing the potential recrystallization is to kinetically hinder the molecular movement of the API by dispersing it inside a glassy hydrophilic polymeric matrix to form an ASD [6, 7]. Examples of polymers recently used to stabilize different APIs such as the preparation methods were mentioned for instance by Baghel et al. [13], whereas already commercially available ASDs alongside their manufacturing technique and the approval year were mentioned for instance by Bhujbal et al. [10] and Tambe et al. [11]. Moreover, a recent update on the available experimental methods to characterize ASDs was presented for instance by Ma and Williams [87] and Dedroog et al. [88]. An overall classification of solid dispersions depending on the number of phases and the state of the API was presented for instance by Shah et al. [6].

One very important aspect in the development of ASDs is the effect that ambient moisture has on the physical properties of the formulation, e.g. [86, 89–91]. Many low molecular weight substances plasticize the amorphous material into which they absorb, reducing their glass temperature and inducing the glass transition at ambient temperature for a given composition and vapor pressure of the sorbed component [86]. Water is one of the most important plasticizers of hydrophilic components due to its low glass temperature, e.g. [86, 91, 92]. For instance, Hancock and Zografi [86] found out that amorphous metastable materials between the glass and fusion temperatures usually absorb considerably greater quantities of water than their respective glasses. On the other hand, crystalline materials adsorb water vapor in small quantities at their surfaces or take up larger stoichiometric quantities to form solvates, whereas amorphous materials absorb water vapor in relatively large amounts up to 100 % by weight [86]. Moreover and as a consequence of the greater free volume in amorphous materials, diffusive transport processes are usually significantly more rapid than in crystals leading to different diffusion rates above and below T_G, with significantly faster diffusion rates occurring above the glass temperature [86]. Furthermore, Levine and Slade [91] stressed out the importance of the temperature range in which water sorption experiments are carried out, since it may be possible that no true thermodynamic equilibrium is attained as a consequence of the plasticization due to sorbed water. Additionally, moisture sorption may induce the formation of an APS, e.g. [16]. Therefore, the correct description of the effects of water sorption in the ASD is of utmost importance to also correctly predict the plasticization effect.

Oksanen and Zografi [93] observed that the amount of water vapor absorbed at a particular relative humidity increases with decreasing temperature, along with a significant change in the shape of the absorption isotherm. However, since the glassy state is not at equilibrium, EOSs cannot be used without additional modifications to calculate the water sorption in polymers below T_G. Nevertheless, Doghieri and Sarti [94] developed the non-equilibrium lattice fluid (NELF) model to account for the reduced water uptake by amorphous materials below their glass temperature. The main idea behind this approach, as summarized later by Sarti and Doghieri [95], consists on replacing the true equilibrium density of the system with the experimentally measured density, using however the already derived expressions for systems at equilibrium as explained in detail by Doghieri and Sarti [94]. This approach [94] has been already applied in the literature, e.g. by Grassia et al. [96], using the SLE EOS. Moreover, Borrmann et al. [97, 98] and Grönniger et al. [99] used the PC-SAFT EOS to calculate the thermodynamic properties in their approach which is known as the non-equilibrium thermodynamics of glassy polymers. However, it must be pointed out that the glassy density of the polymer as a function of the absorbed water, and therefore of the relative humidity, is usually unknown and difficult to experimentally obtain. Therefore, the glassy density of the polymer as a function of the relative humidity has been fitted to the water sorption experimental data [97–99], undermining the prediction capability of the model. To the best of my knowledge, there is no other model available in the literature which can successfully predict the water sorption in glassy polymers without adjusting further parameters to the water sorption data.

In this work, the APIs GRI, IBU, IND and NAP were investigated in detail. All four APIs belong to the class II pharmaceuticals according to the BCS [85]. Their molecular structures are shown in Figure 2.3.

GRI is an antifungal [100] pharmaceutical (chemical abstracts service (CAS) $126-07-8$) used in the treatment of ringworm in animals and humans via oral administration since its marketing in 1959 [101]. In recent years, GRI has regained attention due to its antiviral and anticancer effect [101]. A large compilation of studies related to the biological activity, e.g. [100], and regarding the physicochemical properties such as synthesis paths, e.g. [101], were reported in the literature.

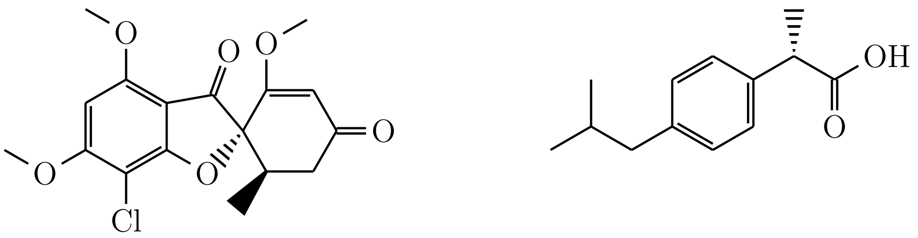

griseofulvin (GRI) ibuprofen (IBU)

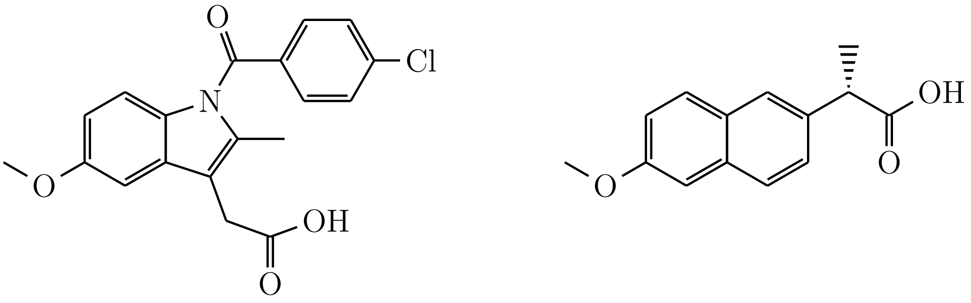

indomethacin (IND) naproxen (NAP)

Figure 2.3: Molecular structures of the APIs investigated in this work. GRI, IBU and NAP exhibit enantiomeric behavior.

The polymorphic forms of the studied APIs are particularly relevant for the calculations performed in this work, as experimental SLE data was used to fit both pure component and binary interaction parameters. The fusion properties (enthalpy and temperature) of the APIs, which depend on the polymorphic form used in the experiments, are required to perform SLE calculations with an EOS as explained in detail in section 3.3. Therefore, the fusion properties of the polymorphs of GRI, IBU, IND and NAP known to this date, to the best of my knowledge, are reported in Table 2.1, whereas only studies explicitly studying the polymorphs of the APIs and reporting both the fusion enthalpy and temperature were regarded.

Form I of GRI (Table 2.1) is the most stable polymorph and also exhibits the largest fusion enthalpy [102]. For a detailed discussion about the differences of all polymorphs, the reader is referred to the original sources.

IBU is a nonsteoridal anti-inflammatory drug (NSAID) (CAS of racemate 15687−27−1) with similar effects as aspirin [103]. It is readily used in many countries as analgesic without prescription at low doses under $1200\,\mathrm{mg\,d^{-1}}$ [104]. Chemically speaking, both enantiomers of IBU exhibit different pharmacological properties [105], however, the marketed product consists of the racemic mixture [105]. An extensive discussion of the pharmacological properties of the enantiomers and the racemate can be found in the literature, e.g. [105]. Furthermore, a compendium of studies regarding the clinical effects of IBU, e.g. [103], such as studies on the efficacy and safety of the drug, e.g. [104], can also be found in the literature. In regard to the polymorphs of IBU listed in Table 2.1, form I is stable, whereas form II is metastable [106].

IND is also a NSAID (CAS $53-86-1$) widely used in the treatment of arthritis [107, 108]. The pharmacological properties, e.g. [107, 109], such as its physicochemical properties and synthesis paths, e.g. [108], can be found in the literature.

Table 2.1: Polymorphs and fusion properties of GRI, IBU, IND and NAP.

API	Polymorph[*]	$\Delta_{\mathrm{SL}}h_{0,i}$ [$\mathrm{kJ\,mol^{-1}}$]	$T_{0,i}^{\mathrm{SL}}$ [K]	Reference
GRI[a]	I	$40 \pm 3\,\%$	494.15	[102]
	II	$30 \pm 3\,\%$	488.15	
	III	$28 \pm 3\,\%$	480.15	
	IV	$28 \pm 3\,\%$	478.15	[110]
	V	$26 \pm 3\,\%$	462.15	
IBU[b]	I	$26.4 \pm 0.3\,\%$	348.4 ± 0.3	[111]
	II	Not reported	291.0 ± 0.3	
IND[c]	I	39.2	431.1 ± 0.4	[112]
	II	37	424.6 ± 0.6	
	III	26.53 ± 0.69	407.32 ± 0.76	[113]
	IV	30.78 ± 0.38	406.72 ± 0.29	
NAP[d]	I	26[e]	429.35	[114]
	II	22[e]	421.35	
	III	23[e]	413.15	
	IV	32[e]	349.15	

[*] The designation of polymorphs using roman numbers is arbitrary and is reported in descending order relative to the fusion temperature.

[a] The fusion properties correspond to the enantiomer shown in Figure 2.3.

[b] The fusion properties correspond to the racemic mixture of both (S) and (R) enantiomers.

[c] Three further polymorphs were reported by Surwase et al. [115], however, the fusion enthalpies were not estimated.

[d] The fusion properties correspond to the (S) enantiomer as confirmed by Maxwell and Chickos [116].

[e] These values were estimated by graphical numerical integration from the thermographs shown in Figure 2 in the publication of Song and Sohn [114] using a sample mass of 5 mg and heating rate of $5\,\mathrm{K\,min^{-1}}$. Thus, they are a rough approximation and must be taken with care.

The marketed product contains the stable polymorph known in the literature as γ and corresponding to the form I in Table 2.1.

NAP is also a NSAID (CAS of (S) enantiomer $22204-53-1$) used in painful and inflammatory rheumatic conditions which may be orally or rectally administered [117]. The pharmacological properties of NAP, e.g. [117–119], the first synthesis paths, e.g. [120, 121], such as recent advances in its synthesis, e.g. [122], are readily found in the literature. Form I (Table 2.1) is the most stable polymorph of NAP [114]. A discussion of DSC thermographs and X-ray power diffraction (XRPD) patterns of NAP polymorphs can be found for instance in Song and Sohn [114].

In this work, PVP (CAS 9003 − 39 − 8) was selected as polymer to study the phase behavior of ASDs due to the large number of experimental studies regarding the glass temperature of pure PVP, e.g. [3, 43, 45, 57, 58, 60, 123–135], the T_G of ASDs, e.g. [16, 54–56, 58, 59, 64, 136, 137], SLE with APIs, e.g. [16, 44], moisture sorption in the pure polymer, e.g. [56, 93], and in the ASDs, e.g. [138–142], such as the glass temperature of ASDs as a function of relative humidity, e.g. [56, 142], available in the literature. The constitutive monomeric structure of PVP is presented in Figure 2.4.

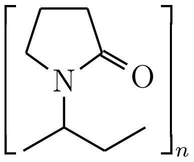

Figure 2.4: Constitutive monomeric structure of PVP.

PVP, also known in the market as Povidone®, Kollidon® and Plasdone®, is usually obtained by free-radical polymerization of vinyl pyrrolidone in water or 2-propanol [143] giving a Schulz-Flory molecular weight distribution [144]. Several other derivatives of vinyl pyrrolidone and copolymers are also used in pharmaceutical formulations [143]. PVP exhibits a relative universal solubility ranging from very hydrophilic solvents such as water to hydrophobic liquids such as butanol [143]. Furthermore, the glass temperature of high molecular weight PVP [144] is relatively high compared to the glass temperature of the APIs studied in this work. Therefore, PVP may be used as an antiplasticization agent to increase the glass temperature of the ASDs, as PVP is also non-toxic, can be quickly and completely excreted through the kidneys when orally administered and thus may be used in pharmaceutical formulations for humans [145].

2.3 Experimental techniques

The description of the techniques presented in this section is intended as a brief introduction into the experimental set up. The actual techniques used by the authors who measured the experimental data shown in chapter 4 may differ from the description given here. Furthermore, only the most relevant and used techniques are presented, however, other methods which are not described in this section may have been used in measuring the experimental data cited in this work.

2.3.1 Pressure-volume-temperature

2.3.1.1 Confining fluid method

This method can be used to measure the pressure-volume-temperature (PVT) behavior of polymers, e.g. [146], and APIs, e.g. [147]. The basic principle as explained in detail by Zoller et al. [148] consists on measuring the expansion or contraction of a flexible metallic bellows attached to one end of a rigid measuring cell where the sample and the confining fluid, usually mercury, are contained. The length change of the bellows is measured by a previously calibrated linear variable differential transformer [148]. The experimental set up allows measuring the volume change of the sample upon isothermal pressure changes or isobaric temperature changes, whereas the best way needs to be tested for each particular investigated component [148]. Since the expansion or contraction of the bellows is not only a function of the properties of both fluids, pressure and temperature, but also of the geometry of the experimental set up, a calibration run using only mercury needs to be performed prior to measurement on the sample [148]. Furthermore, the cross section of the bellows also needs to be precisely estimated as well as its variation with temperature due to the thermal expansion of the material, however, its pressure dependence is for all practical purposes negligible [148].

2.3.2 Solid-liquid equilibrium

2.3.2.1 Gravimetric method

This method can be used to measure the SLE of an API in organic solvents, e.g. [149, 150]. It consist on mixing known masses of a solute, the API, in a liquid solvent, so that the resulting mixture is supersaturated [149, 150]. The supersaturated mixtures are kept at constant temperature under permanent stirring for a fixed period of time [149, 150]. Gracin and Rasmuson [149] assumed that equilibrium of the solutions containing IND was reached after 72 h, whereas Zhao et al. [150] assumed that the equilibrium of solutions containing GRI was reached after 24 h. Then, the undissolved crystals were allowed to settle down for at least 2 h without stirring [149, 150]. A sample of the clear saturated solution is then taken using a preheated syringe and is placed in a preheated and previously weighed vial [149, 150]. The vial is thereafter placed in a vacuum oven at room temperature and the solvent is allowed to evaporate until no change in the sample weight is recorded [149, 150]. The solubility can then be computed from the known masses of the empty vial, vial plus saturated solution and vial plus dry residue [149, 150].

2.3.2.2 Ultraviolet spectrophotometry

The concentration of the API in the liquid phase of the saturated solutions can be also measured using the ultraviolet (UV) absorbance. First of all, a calibration curve is constructed by mixing known masses of solute and solvent together to then measure the UV absorbance of the mixture at the previously identified optimal wavelength [151–155]. A linear function is then fitted to the measured points of UV absorbance over the solute concentration. Subsequently, an excess mass of the solute is diluted in the solvent and allowed to reach equilibrium at constant temperature under stirring. The saturated solutions are then isothermally filtered to remove any undissolved crystals and are accordingly diluted to fall between the range of the calibration curve constructed. Finally, the UV absorbance of the liquid phase in the saturated solutions is measured at the optimal wavelength and constant temperature to then interpolate the solute concentration from the calibration curve. Since the calibration curve is often constructed using molarity to express concentration, the density of the saturated solutions at the given temperature is required to calculate the molar fraction. The density of the saturated solution may be calculated from correlations [155] or directly measured using appropriate techniques [151]. For instance, a thorough description of the method and its variations was reported by Østergaard [156].

2.3.3 Glass temperature

2.3.3.1 Differential scanning calorimetry

This experimental technique can be used to estimate the fusion temperature of pure pharmaceuticals, e.g. [3, 116, 149, 150, 157], the SLE of APIs with polymers, e.g. [3, 16, 44, 59, 60, 136], the glass temperature of pure components, e.g. [3–5, 58, 106] such as the T_G of ASDs, e.g. [3, 16, 43, 54–60, 64, 92, 93, 136, 137, 158–162].

The basic principle behind the method consists on isobarically measuring the heat flow through the sample and a reference as a function of time as explained in detail for instance by Höhne et al. [163] and Zheng et al. [164]. The different types and modes of operation in DSC are explained in detail by Höhne et al. [163]. The heat-flux method is briefly illustrated in the next lines as it was employed to gather most of the experimental data measured via DSC reported in this work. Two crucibles, one empty and one containing the sample, are placed inside a furnace with known thermal resistance in which the atmosphere can be modified using a purge gas [163]. The temperature of both the reference and the sample is measured over time using thermocouples of the same type upon applying a known heating rate [163]. The DSC signal, expressed as an specific heat flow usually in $\mathrm{mW\,g^{-1}}$, can be then computed from the measured temperatures and known thermal resistance via Fourier's law, provided that both crucibles inside the furnace are an exact copy of one another [163]. Prior to a DSC measurement, the apparatus needs to be calibrated to account for any heat losses by measuring the DSC output signal of a material with known heat capacity [163]. Common materials used in the calibration of the DSC apparatus are indium and sapphire.

The glass temperature can be measured using DSC by analyzing the output heat flow against the temperature. First of all, the thermal history of the sample needs to be erased by performing a first heating run up to a temperature above T_G in an inert atmosphere, usually using dry nitrogen. In the case of non-crystalline polymers, the relevant DSC run used to estimate T_G may be performed upon cooling, since there is no risk of crystallization at low heating rates, as is the case for APIs. Furthermore, the well-documented enthalpy overshoot observed by performing the DSC run upon heating [163] can be also avoided. The enthalpy overshoot, also known as enthalpy recovery and enthalpy relaxation, is proportional to the annealing time the sample has undergone as explained in detail elsewhere, e.g. [165]. The DSC thermograph obtained upon isobarically cooling a pure sample is schematically shown in Figure 2.5.

After performing the first heating run to erase the thermal history, the metastable liquid is cooled down exhibiting a linear decrease of the heat flow with temperature down to the onset temperature, T_{on}, where a sharper linear decrease in the output DSC signal is observed [163] as shown in Figure 2.5. The decrease in the measured heat flow flattens towards a less pronounced decrease of the heat flow at the offset temperature, T_{off}, after the glass is formed [163].

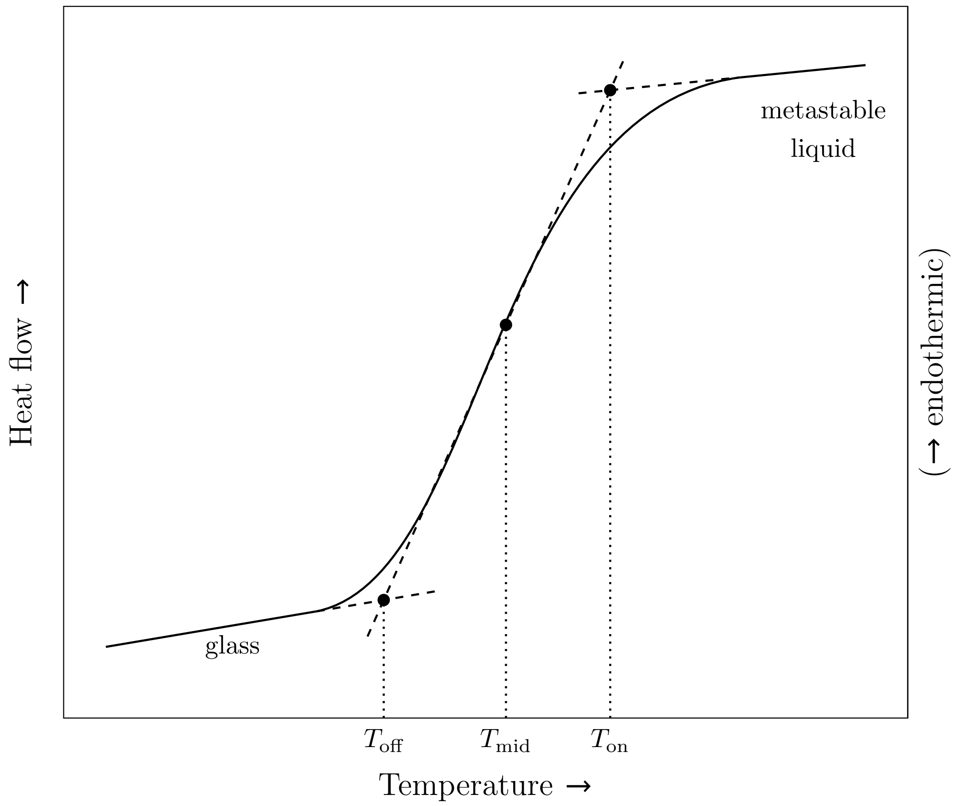

Figure 2.5: Schematic isobaric DSC thermograph of the glass transition upon cooling, where T_{on}, T_{mid} and T_{off} denote the onset, midpoint and offset (also known as endpoint) temperatures, respectively.

The region between T_{on} and T_{off} is known as the glass transition region. It must be pointed out that the designation of T_{on} and T_{off} is interchanged when the sampling run is measured upon heating. The glass temperature is calculated from the thermograph as the temperature at which the inflection point in the heat flow over the temperature is observed, i.e. at T_{mid} in Figure 2.5.

The T_G of APIs is usually measured upon heating to avoid recrystallization of the sample during the DSC scan upon cooling from the melt. The crystalline API is initially completely melted inside the calorimeter under an inert atmosphere of usually nitrogen. Then, the sample is quenched cooled by for instance submerging the sample pan in liquid nitrogen [4] to avert crystallization and ensure that a glass with no remaining crystals is formed. Thereafter, the amorphous sample is heated at a constant rate to then calculate the T_G from the thermograph as the onset temperature of the glass transition event [163].

As mentioned in section 2.1.1, the glass temperature depends on the cooling rate at which the glass was formed. Therefore, the thermograph shown in Figure 2.5 shifts towards lower temperatures when a lower cooling rate is used in the DSC run. In this work, the experimental T_G from different sources is compared, where possible, only when the heating/cooling rates used during measurement are similar.

DSC can also be used to measure the fusion temperature and enthalpy as shown in Figure 2.6.

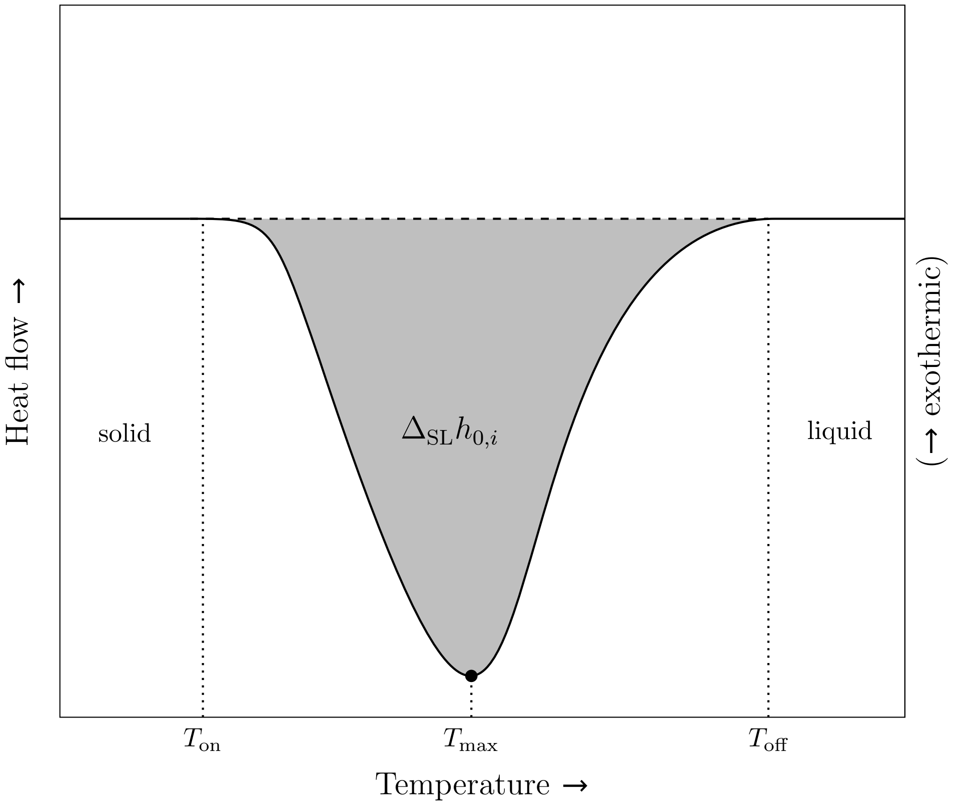

Figure 2.6: Schematic isobaric DSC thermograph of the solid-liquid transition of an API upon heating, whereas T_{on}, T_{max} and T_{off} denote the onset, peak maximum and offset (also known as endpoint) temperatures, respectively.

Given that the sample can crystallize, as is the case for the APIs investigated in this work, the thermograph shown in Figure 2.6 is found at temperatures above the glass transition event shown in Figure 2.5. At this point it is important to stress out that the scale of the heat flow in the fusion event shown in Figure 2.6 is much larger than in the glass transition event shown in Figure 2.5 as evidenced in the thermographs obtained by for instance Knopp et al. [44], Prudic et al. [60] and Lopez et al. [43]. Therefore, care must be taken when concluding from thermographs found in the literature that no glass transition took place. The schematic fusion event shown in Figure 2.6 measured upon heating also exhibits an onset temperature, where the completely crystalline sample begins to melt. The fusion event is complete upon reaching the offset (also known as endpoint) temperature, where the whole sample already melted and no more crystals are present [163]. The peak maximum temperature is located where the DSC output signal of the fusion event is absolutely maximal [163]. The fusion temperature is often reported as the onset temperature of the fusion event, e.g. [3, 116], whereas the fusion enthalpy is assessed from the gray area shown in Figure 2.6 as explained in detail elsewhere, e.g. [163].

Furthermore, it is possible to estimate the SLE equilibrium temperature of ASDs, e.g. [3, 16, 44, 59, 60, 136], often called end point dissolution temperature, via DSC using different methods as explained in detail by for instance Mathers et al. [3]. For instance, the melting point depression method is based on the fact that the fusion temperature of the API decreases, provided the ASD formed is miscible, by increasing the content of the polymer in the ASD [3]. The fusion temperature can be then estimated from the corresponding thermograph (similar to that presented in Figure 2.6) as the onset, peak maximum or offset temperature [3]. It is still controversial which of the three temperatures illustrated in Figure 2.6 should be taken as the true fusion temperature [3]. For instance, Mathers et al. [3] assigned the fusion temperature to the peak maximum, whereas Prudic et al. [60] assigned it to the offset temperature. If mentioned by the authors, the point assigned to the fusion and glass temperatures in the DSC thermographs is mentioned where the corresponding experimental data is shown.

The DSC method can be improved by using a temperature modulation during measuring [163]. In modulated differential scanning calorimetry (mDSC), the same heat-flux DSC arrangement is used, however a different temperature (heating/cooling) profile is applied to the sample and reference via the furnace [163]. Specifically, a sinusoidal ripple (modulation) is overlaid on the standard linear temperature ramp as shown for instance by Gill et al. [166] and Zheng et al. [164].

2.3.3.2 Broadband dielectric spectroscopy

This technique consists on measuring the dielectric loss as a function of frequency usually at constant pressure over several temperatures to then obtain the relaxation time as a function of temperature from the measured data [147, 167–171]. A comprehensive description of the required theoretical background is outside the scope of this work and can be found elsewhere, e.g. [39]. The main idea behind the method consists on measuring the response of the examined dielectric material to an applied alternating electric field over a wide frequency range [172]. Specifically for BDS, a dielectric, defined as a material that can sustain polarization or surface charge without loss due to conductivity [39], is required. In practice, the polarization is lost due to conductivity and the term dielectric applies to those materials which can hold polarization for a certain amount of time [39]. Experimental set ups to apply the technique are described elsewhere, e.g. [147, 167–171]. For instance, the imaginary part of the isobaric dielectric loss spectra as a function of frequency at different temperatures is schematically shown in Figure 2.7.

Each dielectric loss spectra shown in Figure 2.7 exhibits a maximum at a certain frequency and temperature, $\bar{f}_{max}(T)$, which can be related to the relaxation time, τ_α, via

$$\tau_\alpha = \frac{1}{2\pi \bar{f}_{max}(T)}. \tag{2.12}$$

After measuring the dielectric loss spectra at different temperatures, the relaxation time can be computed from equation (2.12) and plotted against the temperature. The results are then often fitted using the empirical equations presented in section 2.1.2, i.e. the VFTH equation (2.1) or the WLF equation (2.5), to obtain the glass temperature at $\tau_\alpha = 100\,\mathrm{s}$.

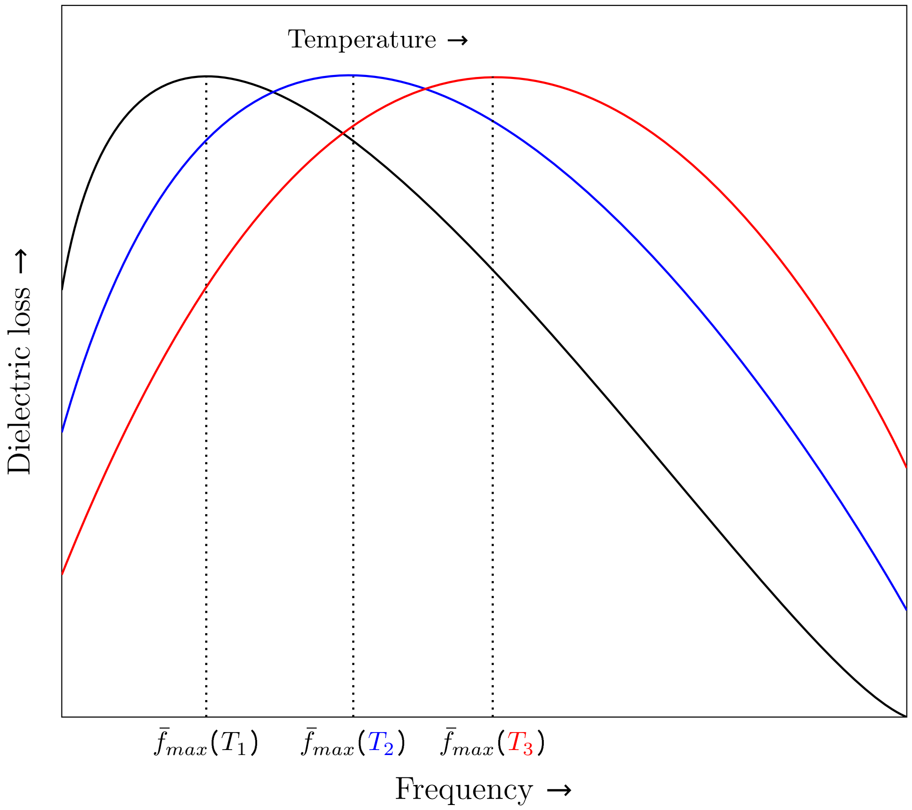

Figure 2.7: Schematic isobaric dielectric loss spectra of a pure component showing only the α relaxation. The dielectric loss is measured at constant temperature corresponding to the respective colors so that $T_3 > T_2 > T_1$. The relaxation time at a given pressure and temperature is calculated from the maximum value of the corresponding dielectric loss spectrum using equation (2.12).

2.3.4 Water sorption

2.3.4.1 Isopiestic method

The method consists on estimating the water activity at constant temperature in several solutions physically interconnected to each other to allow for mass transport between them as described in detail by Ochs et al. [173]. The isopiestic method can be applied to calculate the water sorption in polymers, for instance in PVP [174]. Sadeghi and Taghi Zafarani-Moattar [174] measured the water activity at constant temperature in four solutions contained in flasks connected via a five-leg manifold. Two of the flasks contained NaCl solutions, two other the water-PVP solutions and the fifth one was used as water reservoir [174]. Since the water activity of all interconnected solutions depend on each other, estimating the water sorption in the NaCl solutions enables indirect estimation of the water activity in the solutions containing PVP [174]. Equilibrium was assumed to be reached after 120 h and the water uptake was estimated gravimetrically [174]. Furthermore, Sadeghi and Taghi Zafarani-Moattar [174] calculated the vapor pressure of the PVP aqueous solutions, P^{LV}, from the measured water activity using the following relation

$$\ln \mathsf{a}_{\mathrm{W}} = \ln\left(\frac{P^{\mathrm{LV}}}{P^{\mathrm{LV}}_{0,\mathrm{W}}}\right) + \frac{\left(B^{\mathrm{V}}_{0,\mathrm{W}} - v^{\mathrm{L}}_{0,\mathrm{W}}\right)\left(P^{\mathrm{LV}} - P^{\mathrm{LV}}_{0,\mathrm{W}}\right)}{RT}, \tag{2.13}$$

where a_{W} denotes the water activity, $P^{\mathrm{LV}}_{0,\mathrm{W}}$ the vapor pressure of pure water, $B^{\mathrm{V}}_{0,\mathrm{W}}$ the second virial coefficient of water vapor and $v^{\mathrm{L}}_{0,\mathrm{W}}$ the molar volume of liquid water. The comprehensive derivation of equation (2.13) can be found in Pitzer [175]. In deriving equation (2.13), the standard pressure of the water activity was set to the vapor pressure of water at the temperature of the solution, the reality of the vapor phase was accounted for using the virial EOS expanded in the pressure truncated to the second term, the liquid phase was assumed incompressible and the partial molar volume of water was assumed equal to the molar volume [175]. Furthermore, the virial coefficient used was taken from Le Fevre et al. [176], the molar volumes of saturated liquid water from Kell [177] and the vapor pressure of pure water from Wexler and Greenspan [178] as described in Table 1 on page 219 in Pitzer [175].

2.3.4.2 Desiccator method

This method can be used to investigate the vapor sorption in polymers, for instance in PVP [92, 93, 158]. It consists on placing previously dried samples of the polymer in desiccators containing saturated salt solutions under humid air [92, 93, 158]. The polymer samples are usually dried over P_2O_5 [158] or under vacuum at elevated temperature [93] prior to analysis. Then, hygroscopic salts such as, amongst others, sodium hydroxide, sodium bromide and potassium nitrate are placed in sealed desiccators at a known constant temperature [92, 93, 158]. The humidity absorbed by the salts at different temperatures is well documented in the literature, e.g. [93], and cited references, so that the relative humidity prevailing in the atmosphere within each desiccator containing a different salt is known. Thereafter, the dried polymer samples are placed in the desiccators after previous equilibration and the weight gain is monitored over time until no change or certain weight gain conditions are met. For instance, Oksanen and Zografi [93] assumed equilibrium was reached after the weight gain was less than $5\,\mathrm{mg\,g^{-1}}$ compared to the previous measurement, whereas Buera et al. [158] let the samples equilibrate for at least a week. The measured weight after equilibrium is reached can be then correlated to the relative humidity (RH) prevailing inside each desiccator [92, 93, 158].

2.3.4.3 Dynamic gravimetric methods

Unlike the desiccator method, the experimental set ups mentioned in this section allow for a dynamic change in the RH over the investigated sample without removing it from the measuring cell, e.g. [56, 98, 140, 142, 159, 179, 180]. Andronis et al. [159] used a self-made set up developed and depicted by Kontny et al. [181], where the water sorption can be dynamically measured using an electrobalance. On the other hand, there is the possibility of performing the measurements inside commercially available units equipped with a balance inside the measuring chamber in which the partial pressure of water can be conveniently set up [56, 98, 140, 142, 179, 180]. The sample weight gain over time is carefully monitored until no weight change is registered or a certain condition is met, whereas the initial humidity in the sample is previously removed after exposing it to a dry atmosphere until no weight change is registered [56, 98, 140, 142, 179, 180]. For instance, Crowley and Zografi [56] assumed equilibrium was reached after the weight change was less than 0.001 mg over 7 min, Dawson et al. [179] after a lower weight change than 0.005 % over 40 min and Borrmann et al. [180] after a lower weight change than 0.0001 % min^{-1}. The absorbed water at equilibrium can be then plotted against the corresponding RH to which the sample was exposed to.

3 Theory

In this chapter, an overview of the models used for calculations in this work is given. The derivation of the SL EOS for pure components and multicomponent mixtures is presented in section 3.1. The calculations of the glass temperature using the SL EOS for pure components and ASDs such as the influence of pressure on the glass temperature are considered in section 3.2. A brief introduction to the calculation of API crystal solubility (SLE) and moisture sorption (vapor-liquid equilibrium (VLE)) of polymers and APIs using the SL EOS is presented in sections 3.3 and 3.4, respectively. Finally, the parameter fitting approach used to fit the SL parameters of pure components is explained in detail in section 3.5.

3.1 Sanchez-Lacombe equation of state

The SL EOS was originally derived for pure components [23] and then extended to binary mixtures [182]. Later, mixing rules in the characteristic pressure, P^*, rather than in the interaction energy parameter, ϵ^*, were used to ensure quantitatively better results [24]. The derivation of the SL EOS for a pure substance and then for mixtures of C components using mixing rules in P^* is briefly discussed in the following paragraphs.

The main idea behind the model is to introduce an incompressible lattice with vacant sites, where equally large parts of a chain molecule are placed as schematically shown in Figure 3.1. The chain molecule, also known as r-mer [23], is composed of the compendium of all bonded chain segments represented by the filled circles in Figure 3.1, whereas the vacant sites are represented as empty circles.

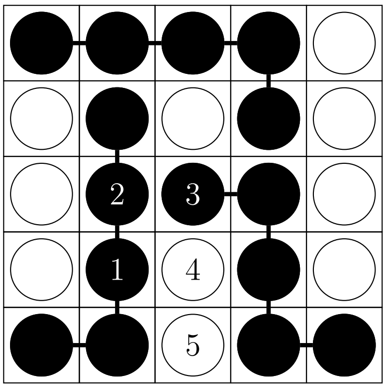

Figure 3.1: Schematic lattice construction of a chain molecule adapted from Sanchez and Lacombe [23]. Filled circles represent equally large chain segments, empty circles denote vacant lattice sites and thick lines denote chemical bonds. The volumes of the chain segments and vacant sites, v^* , are equal, whereas each of the three chain molecules is composed of r = 5 chain segments.

Several assumptions were made by Sanchez and Lacombe [23] in deriving their EOS. On one hand, only the nearest neighbor chain segment interactions were considered, indeed only the nearest neighbor energy pair interactions between non-bonded chain segments, ϵ^*, are non-zero ($2-3$ interaction in Figure 3.1) [23]. All other nearest neighbor interactions, i.e. bonded chain segments ($1-2$), vacant site and chain segment ($3-4$) and interactions between vacant sites ($4-5$) are assumed zero [23]. Each chain molecule has a number of chain segments, r, and each chain segment a volume, v^* [23]. Moreover, the volume of the vacant site is equal to the chain segment volume [23]. Additionally, it was assumed that the close-packed volume of the chain molecule, i.e. rv^*, is temperature and pressure independent [23]. On the other hand, the internal degrees of freedom exhibited by the chain molecules may be described by a flexibility parameter, δ, which was mentioned in the original publication [23]. However, this parameter was neglected for all practical calculations by Sanchez and Lacombe [23], as well as in this work. Furthermore, the compressibility of the system is described only by the variation in the number of the vacant lattice sites, as the lattice itself is assumed incompressible [23].

From a statistical mechanical point of view, the goal is to derive an adequate expression for the partition function Z in the Gibbs ensemble (constant number of molecules, N, pressure, P and temperature, T) for the chain molecule within the lattice, which is related to the free enthalpy, G, via [23]

$$G(T,P,N) = -k_B T \ln Z(T,P), \tag{3.1}$$

where k_B is Boltzmann's constant. The derivation can also be performed using the canonical ensemble (constant N, volume, V and T) which leads to the free energy A [183]

$$A(T,V,N) = -k_B T \ln Z(T,V). \tag{3.2}$$

The use of both partition functions $Z(T,P)$ and $Z(T,V)$ lead to the same results in the thermodynamic limit $N \approx 10^{23}$ [184]. For instance, the derivation of the SL EOS via the canonical ensemble was carried out by von Konigslow et al. [185]. An analytical expression of any of the thermodynamic potentials leads to the whole description of the thermodynamic behavior of the chain molecule, since all thermodynamic potentials can be calculated from each other via Legendre transformation and all thermodynamic properties follow from their derivatives.

Of course, an expression of the partition function in equation (3.1) has to be first estimated. Sanchez and Lacombe [23] further assumed random mixing of vacant sites and chain segments to derive an expression of the partition function as

$$Z(T,P) = \sum_{N_0=0}^{\infty} \Omega \exp\left[-\beta(E+PV)\right], \tag{3.3}$$

whereas N_0 denotes the total number of vacant sites, Ω the total number of configurations available to the chain molecule, E the potential energy of the lattice and $\beta = 1/(k_B T)$. Replacing equation (3.3) in equation (3.1) after using a mean-field random mixture assumption to estimate Ω leads to [23]

$$\tilde{G} = \frac{G}{rN\epsilon^*} = -\tilde{\rho} + \tilde{P}\tilde{v} - \tilde{T}\tilde{s}, \tag{3.4}$$

where $\tilde{\rho} = \rho/\rho^*$ is the reduced density, $\rho^* = \bar{M}/(rv^*)$ is the close-packed specific density, $\tilde{P} = P/P^*$ is the reduced pressure, $P^* = \epsilon^*/v^*$ is the characteristic pressure, $\tilde{T} = T/T^*$ is the reduced temperature, $T^* = \epsilon^*/R$ is the characteristic temperature, N the total number of chain molecules and $\tilde{s}$ the reduced entropy defined as [23]

$$\tilde{s} = \frac{s}{R} = -\left[\left(\frac{1}{\tilde{\rho}} - 1\right)\ln\left(1 - \tilde{\rho}\right) + \frac{1}{r}\ln\tilde{\rho}\right]. \tag{3.5}$$

It should be noted that the mean-field random mixture assumption leads to unreliable results when concentration fluctuations play a major role, i.e. thermodynamic properties at molecular level may not be assumed equal to the bulk properties. Therefore, the SL EOS is not expected to correlate well with experimental data near the critical point as pointed out by Sanchez and Lacombe [23] themselves. Equation (3.4) and (3.5) may be used to derive all other thermodynamic properties of interest, however, the corresponding reduced density needs to be first calculated via minimization of $\tilde{G}$ with respect to the reduced volume $\tilde{v} = 1/\tilde{\rho}$ to obtain the SL EOS as [23]

$$\tilde{\rho}^2 + \tilde{P} + \tilde{T}\left[\ln\left(1 - \tilde{\rho}\right) + \left(1 - \frac{1}{r}\right)\tilde{\rho}\right] = 0. \tag{3.6}$$

The reduced density, $\tilde{\rho}$, is also equal to the fraction of occupied lattice sites [23]. Therefore, it is very important to point out that the entropy calculated with equation (3.5) depends only on the possible configurations available to the system.

The thermodynamics of a pure component can be completely described by using equations (3.4), (3.5), (3.6) and either the molecular parameters r, ϵ^* and v^* or the scaling parameters ρ^*, T^* and P^*, which need to be fitted to experimental data. The SL parameter fitting approach used in this work is discussed in detail in section 3.5. Concerning the SL molecular parameters, fitting the segment number, r, to experimental data fixes the size of the chain molecule to a certain value. Therefore, only a description of monodisperse chain molecules is possible with the original SL EOS, even though it may be modified to account for polydispersity, e.g [186].

The extension of equation (3.6) to binary and multicomponent mixtures requires the calculation of the mixture parameters (r, v^* and ϵ^*), however, the functional form of the EOS remains unaltered [182]. Furthermore, equation (3.5) has to be extended to incorporate possible configurations between both components. For this purpose, the incompressible lattice construction of a binary mixture of chain molecules is considered in Figure 3.2.

The only nearest neighbor non-zero energy interactions in the mixture are the ones between non-bonded chain segments of the same species, ϵ^*_{ii}, and the chain segments of different species, ϵ^*_{ij} [182]. Furthermore, the volume of the vacant sites in the mixture, v^*, needs to be somehow estimated from the pure component segment volumes, v^*_i, which is not trivial. As in the case for pure components, the vacant site volume of the mixture is not a function of temperature or pressure, however, it must be a function of composition for it to correctly limit to the pure component segment volumes. As v^* is defined per lattice site, it is natural to take the average using the segment fraction $\phi^0_i = r^0_i N_i / \sum_i r^0_i N_i$ as first proposed by Lacombe and Sanchez [182] as

$$v^* = \sum_{i=1}^{C} \phi_i^0 v_i^* . \tag{3.7}$$

In equation (3.7), N_i is the number of molecules of species i and C denotes the total number of components in the mixture. Lacombe and Sanchez [182] further introduced the segment number of species i in the mixture as

$$r_i = \frac{r_i^0 v_i^0}{v^*}, \tag{3.8}$$

so that the close-packed volume of the chain molecule is conserved and defined the average segment number of the mixture as

$$r = \left(\sum_{i=1}^{C} \frac{\phi_i}{r_i} \right)^{-1}, \tag{3.9}$$

whereas ϕ_i denotes the volume fraction of component i.

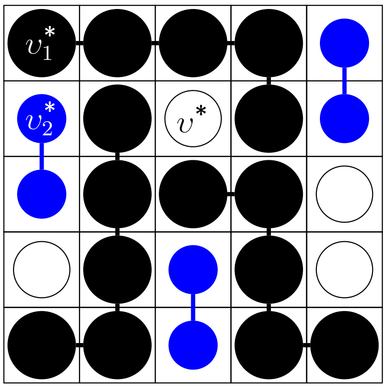

Figure 3.2: Schematic lattice construction of a binary mixture of chain molecules adapted from Sanchez and Lacombe [24]. Black and blue filled circles represent equally large chain segments of species 1 and 2, respectively. Species 1 is composed of $r_1^0 = 5$ and species 2 of $r_2^0 = 2$ chain segments. The volumes of the chain segments of each pure species are different, i.e. $v_1^* > v_2^*$, whereas the volume of the vacant lattice sites, v^*, is an arbitrary function of both v_1^*, v_2^* and the composition of the mixture, but not of temperature and pressure.

Furthermore, an additional mixing rule for the chain segment interaction energy of different species is required. Lacombe and Sanchez [182] first introduced a double sum over the volume fractions to calculate the interaction energy in the mixture. However, in a subsequent publication [24] the mixing rule in the interaction energy was replaced by applying the double sum mixing rule over the characteristic pressure as

$$P^* = \sum_{i=1}^{C} \sum_{j=1}^{C} \phi_i \phi_j P_{ij}^*, \tag{3.10}$$

where

$$P_{ij}^* = k_{ij} \sqrt{P_i^* P_j^*}, \tag{3.11}$$

k_{ij} is the binary interaction parameter of the mixture used to correct the mixing rule and $P^*_{ii} = P^*_i$. Sanchez and Lacombe [24] argued that mixing rules in P^* delivered quantitatively better results, since the energy interaction is normalized by the corresponding lattice site volume from the definition of P^*. In fact, calculations of the water sorption in PVP performed within this work using mixing rules in P^* delivered physically feasible results (shown in section 4.3), whereas calculations using mixing rules in ϵ^* (not shown) exhibited "forbidden sorption areas", which could not be reached using any value of the binary interaction parameter. The k_{ij} contained in equation (3.11) may be temperature-dependent. In this work, following temperature dependence was considered

$$k_{ij} = k_{ij,0} + k_{ij,T}T, \tag{3.12}$$

whereas T must be the thermodynamic temperature in K. Using mixing rules in P^*, the interaction energy is calculated as $\epsilon^* = P^* \upsilon^*$ using equations (3.7) and (3.10) [24].

With all mixing rules being defined, the extension of equation (3.5) to multicomponent mixtures yields [182]

$$\tilde{s} = \frac{s}{R} = -\left[\left(\frac{1}{\tilde{\rho}} - 1\right)\ln\left(1 - \tilde{\rho}\right) + \frac{1}{r}\ln\tilde{\rho} + \sum_{i=1}^{C}\frac{\phi_i}{r_i}\ln\phi_i\right]. \tag{3.13}$$

The contributions to the entropy calculated from equation (3.13) are, as for pure components, only of configurational nature.

For the description of multicomponent mixtures, equation (3.11) needs to be evaluated for each binary mixture. In this work, no further adjustable parameters were used to describe the thermodynamic properties of multicomponent mixtures, so that all calculations of ternary mixtures API-polymer-water are predictions.

The thermodynamic properties following from the derivatives of equations (3.4), (3.5), (3.6) and (3.13) were obtained analytically and were numerically proofed. Moreover, the chemical potential derived in this work for binary mixtures was equal to the expression reported by Sanchez and Lacombe [24]

$$\begin{aligned} \mu_i =& RT\left[\ln\phi_i + \left(1 - \frac{r_i}{r_j}\right)\phi_j + r_i^0\tilde{\rho}X_i\phi_j^2\right] + \\ & r_i^0 RT\left\{-\frac{\tilde{\rho}}{\tilde{T}_i} + \frac{\tilde{P}_i\tilde{v}}{\tilde{T}_i} + \tilde{v}\left[\left(1 - \tilde{\rho}\right)\ln\left(1 - \tilde{\rho}\right) + \frac{\tilde{\rho}}{r_i^0}\ln\tilde{\rho}\right]\right\}, \end{aligned} \tag{3.14}$$

where

$$X_i = \frac{\Delta P^* \upsilon_i^*}{RT} \tag{3.15}$$

and

$$\Delta P^* = P_i^* + P_j^* - 2P_{ij}^*. \tag{3.16}$$

The chemical potential of components in ternary mixtures was analytically derived as the partial molar property of the free enthalpy obtained from equation (3.4) using the reduced entropy estimated from equation (3.13) with $C = 3$ as

$$\mu_i = \tilde{G}\left[N\epsilon^*\left(\frac{\partial r}{\partial N_i}\right)_{P,T,N_{j\neq i}} + r\epsilon^* + Nr\left(\frac{\partial \epsilon^*}{\partial N_i}\right)_{P,T,N_{j\neq i}} + Nr\epsilon^*\left(\frac{\partial \tilde{G}}{\partial N_i}\right)_{P,T,N_{j\neq i}}\right], \tag{3.17}$$

whereas all involved expressions containing sums need to be evaluated with $C = 3$. Values obtained from equation (3.17) were compared to the ones obtained from the general expression for the chemical potential of species in a multicomponent mixture reported for instance by Xiong and Kiran [187] delivering the exact same results.

3.2 Glass temperature

For the calculation of the glass temperature of pure components at constant pressure using the SL EOS and the GET, the Arrhenius and crossover temperatures, T_A and T_I, respectively, are required as explained in section 2.1.4. For simplicity, the abbreviation GET means from here on the combination of the original theory [9, 22] with the SL EOS. Both T_A and T_I may be calculated with the SL EOS from the derivatives of the reduced entropy density, $\tilde{s}\tilde{\rho}$, with respect to the temperature as

$$\left(\frac{\partial \tilde{s}\tilde{\rho}}{\partial T}\right)_P\bigg|_{T=T_A} = 0 \tag{3.18}$$

and

$$\left(\frac{\partial^2 T\tilde{s}\tilde{\rho}}{\partial T^2}\right)_P\bigg|_{T=T_I} = 0. \tag{3.19}$$

Equations (3.18) and (3.19) were derived analytically from equations (3.5) and (3.6), to be then numerically solved to estimate T_A and T_I. Furthermore, the relaxation time may be calculated in terms of the SL EOS as

$$\tau_\alpha = \tau_0 \exp\left[\frac{\Delta E\tilde{s}(T_A)\tilde{\rho}(T_A)}{RT\tilde{s}\tilde{\rho}}\right], \tag{3.20}$$

where $\tilde{s}\tilde{\rho}$ is evaluated at T, $\tau_0 = 10^{-13}$ s [9] and ΔE is the molar activation energy

$$\Delta E = Rk_pT_I, \tag{3.21}$$

whereas k_p is an adjustable parameter which was fitted to the experimental value of T_G as discussed in detail in section 4.1.2. Moreover, the fragility index defined in equation (2.2) can be analytically calculated in terms of the SL EOS as

$$m = \frac{1}{\ln 10} \frac{\Delta E \tilde{s}(T_A)\tilde{\rho}(T_A)}{RT_G(\tilde{s}\tilde{\rho})^2} \left(\frac{\partial T \tilde{s}\tilde{\rho}}{\partial T} \right)_P \Bigg|_{T=T_G} . \tag{3.22}$$

The procedure for the calculation of T_G for binary and multicomponent mixtures is the same as for pure components. However, the molar activation energy of the mixture, ΔE_{mix}, needs to be somehow estimated from the pure molar activation energies, ΔE_i. In this work, two different approaches were considered without using further adjustable parameters. On one hand, ΔE_i was averaged over the volume fractions as

$$\Delta E_{mix} = \sum_{i=1}^{C} \phi_i \Delta E_i = R \sum_{i=1}^{C} \phi_i k_{p,i} T_{I,i}. \tag{3.23}$$

On the other hand, the crossover temperature of the mixture, $T_{I,mix}$, was calculated from equation (3.19) and the parameters $k_{p,i}$ were averaged over the volume fraction as

$$\Delta E_{mix} = RT_{I,mix} \sum_{i=1}^{C} \phi_i k_{p,i}. \tag{3.24}$$

The influence of moisture on the glass temperature of ASDs can be evaluated using the exact same procedure previously described for binary mixtures, however, setting $C = 3$ in equations (3.7), (3.10), (3.13) and (3.23). In this work, no further adjustable parameters were used to calculate the thermodynamic properties or the glass temperature of ternary systems API-PVP-water, therefore, the results presented in section 4.3 are all predictions.

The influence of pressure on the glass temperature was also calculated by combining the SL EOS and the GET. For this purpose, the procedure previously described for pure components was performed at several pressures by using the same k_p fitted to experimental values of the glass temperature at atmospheric pressure. Thus, the calculations shown in section 4.1.2.1 are also a prediction, since no further adjustable parameters were used.

3.3 Solid liquid equilibrium

The starting point to find an expression to calculate an SLE are the equilibrium conditions between a liquid, L, and solid phase, S, of a mixture containing C components

$$\begin{aligned} T^{\mathrm{L}} &= T^{\mathrm{S}} && \text{Thermal equilibrium} \\ P^{\mathrm{L}} &= P^{\mathrm{S}} && \text{Mechanical equilibrium} \\ \mu_i^{\mathrm{L}}(P^{\mathrm{L}}, T^{\mathrm{L}}, x_i^{\mathrm{L}}) &= \mu_i^{\mathrm{S}}(P^{\mathrm{S}}, T^{\mathrm{S}}, x_i^{\mathrm{S}}) \quad \forall\, i...C && \text{Material equilibrium,} \end{aligned} \tag{3.25}$$

where μ_i denotes the chemical potential of component i in the corresponding phase. The material equilibrium may be replaced by the isofugacity condition as

$$f_i^{\mathrm{L}}(P^{\mathrm{L}}, T^{\mathrm{L}}, x_i^{\mathrm{L}}) = f_i^{\mathrm{S}}(P^{\mathrm{S}}, T^{\mathrm{S}}, x_i^{\mathrm{S}}) \quad \forall\, i...C, \tag{3.26}$$

where f_i denotes the fugacity of component i in the mixture in the corresponding phase [188]. Furthermore, the fugacity is defined as [188]

$$d\mu_i = RT d \ln f_i. \tag{3.27}$$

Equation (3.27) may be isothermally integrated from a pure component standard state at P^0 to the equilibrium state of component i in the mixture at the pressure of the system, P, to obtain [188]

$$\mu_i(P, T, x_i) - \mu_{i,0}(P^0, T) = RT \ln \mathsf{a}_i(P, T, x_i), \tag{3.28}$$

where

$$\mathsf{a}_i(P, T, x_i) = \frac{f_i(P, T, x_i)}{f_{0,i}(P^0, T)}, \tag{3.29}$$

and a_i is the activity of component i in the mixture. Replacing equation (3.29) in equation (3.26) for each phase after defining $P^0 = P$ and assuming that the solid phase always solidifies as pure crystals ($\mathsf{a}_i^{\mathrm{S}} = 1$) follows

$$\mathsf{a}_i^{\mathrm{L}} = \frac{f_{0,i}^{\mathrm{S}}}{f_{0,i}^{\mathrm{L}}}, \tag{3.30}$$

whereas all quantities are to be evaluated at the equilibrium temperature and pressure of the mixture. Equation (3.30) relates the behavior of a component in a mixture described by the activity as a function of only properties of the pure component. Therefore, only a model to estimate a_i alongside some pure component properties, yet to be identified, are required to calculate the SLE. The ratio of both pure component fugacities in equation (3.30) can be related to the free enthalpy by isothermally integrating equation (3.27) to obtain [188]

$$\ln\left(\frac{f_{0,i}^{\mathrm{S}}}{f_{0,i}^{\mathrm{L}}}\right) = \frac{g_{0,i}^{\mathrm{S}} - g_{0,i}^{\mathrm{L}}}{RT}, \tag{3.31}$$

whereas the pure component chemical potential was replaced by the corresponding molar free enthalpy. The right hand side of equation (3.31) can be then evaluated by integrating the Gibbs-Helmholtz equation for the free enthalpy [188]

$$\left(\frac{\partial(G/T)}{\partial T}\right)_{P,N} = -\frac{H}{T^2} \tag{3.32}$$

at constant pressure to correct the deviations of both fugacities from the fusion temperature, $T_{0,i}^{\mathrm{SL}}$, to the equilibrium temperature of the mixture as [188]

$$\ln\left(\frac{f_{0,i}^{\mathrm{S}}}{f_{0,i}^{\mathrm{L}}}\right)=-\frac{\Delta_{\mathrm{SL}}h_{0,i}}{R}\left(\frac{1}{T}-\frac{1}{T_{0,i}^{\mathrm{SL}}}\right)+\int_{T_{0,i}^{\mathrm{SL}}}^{T}\frac{\Delta_{\mathrm{SL}}\bar{c}_{p,0,i}(T_0)}{R}\left(\frac{1}{T_0}-\frac{1}{T}\right)dT_0, \tag{3.33}$$

where $\Delta_{\mathrm{SL}}h_{0,i}$ denotes the molar fusion enthalpy of pure i, $\Delta_{\mathrm{SL}}\bar{c}_{p,0,i}(T_0)$ the difference in the molar isobaric heat capacity of pure i across the melting line and T_0 denotes the temperature dependence of the molar isobaric heat capacity. The value of the integral in equation (3.33) is often very small compared to the term containing the fusion enthalpy [188], thus, it was neglected in calculations performed in this work. The ratio of pure component fugacities becomes then

$$\ln\left(\frac{f_{0,i}^{\mathrm{S}}}{f_{0,i}^{\mathrm{L}}}\right)=-\frac{\Delta_{\mathrm{SL}}h_{0,i}}{RT}\left(1-\frac{T}{T_{0,i}^{\mathrm{SL}}}\right). \tag{3.34}$$

Replacing equation (3.34) in (3.30) and expressing the activity as a function of the chemical potentials via equation (3.28) follows

$$\mu_i^{\mathrm{L}}(P,T,x_i)-\mu_{i,0}^{\mathrm{L}}(P,T)=-\Delta_{\mathrm{SL}}h_{0,i}\left(1-\frac{T}{T_{0,i}^{\mathrm{SL}}}\right). \tag{3.35}$$

Equation (3.35) can be solved for the temperature at a given pressure and composition, provided that expressions for the chemical potentials and both the fusion enthalpy and temperature are known.

3.4 Moisture sorption

The equilibrium water sorption in polymers and APIs can be calculated from the equilibrium conditions listed in equation (3.25) by replacing the solid phase with the vapor phase, V. Furthermore, the material equilibrium condition as a function of the chemical potential is more practical in this case, as the SL EOS allows for direct computation of the density of both the liquid and vapor phases. Moreover, only air and water vapor are present in the vapor phase, since polymers and APIs do not evaporate. Additionally, the solubility of air (mostly composed of oxygen and nitrogen) in the liquid phase is negligible at atmospheric pressure. Therefore, the material equilibrium condition reduces to

$$\mu_{\mathrm{H_2O}}^{\mathrm{L}}(P,T,x_{\mathrm{H_2O}}^{\mathrm{L}})=\mu_{\mathrm{H_2O}}^{\mathrm{V}}(P,T,x_{\mathrm{H_2O}}^{\mathrm{V}}). \tag{3.36}$$

Equation (3.36) can be further simplified by assuming that Dalton's law holds in the vapor phase. This assumption is reasonable, insofar the VLEs containing water considered in this work were calculated at temperatures from 25 °C to 50 °C. The vapor pressure of water within this temperature range is much lower than the atmospheric pressure, therefore, even a relative humidity equal to 1 delivers a small partial pressure of water compared to air. Consequently, weak interactions between the water molecules are to be expected in the vapor phase. From equation (3.36) follows then

$$\mu^{\mathrm{L}}_{\mathrm{H_2O}}(P, T, x^{\mathrm{L}}_{\mathrm{H_2O}}) = \mu^{\mathrm{V}}_{0,\mathrm{H_2O}}(P_{\mathrm{H_2O}}, T, x^{\mathrm{V}}_{\mathrm{H_2O}}). \tag{3.37}$$

The partial pressure of water, $P_{\mathrm{H_2O}} = x^{\mathrm{V}}_{\mathrm{H_2O}} P$, needs to be used in the expression to calculate $\mu^{\mathrm{V}}_{0,\mathrm{H_2O}}$ and can be estimated from the definition of the relative humidity, φ,

$$\varphi = \frac{P_{\mathrm{H_2O}}}{P^{\mathrm{LV}}_{0,\mathrm{H_2O}}(T)}, \tag{3.38}$$

whereas $P^{\mathrm{LV}}_{0,\mathrm{H_2O}}(T)$ denotes the vapor pressure of water at the temperature of the system. Equation (3.37) can be then iterated for $x^{\mathrm{L}}_{\mathrm{H_2O}}$ as a function of the relative humidity after specifying the total pressure and temperature. It is important to stress out that the total pressure of the system was held constant at 1 bar to calculate the isothermal water sorption as a function of φ presented in section 4.3. In equation (3.37), $\mu^{\mathrm{L}}_{\mathrm{H_2O}}$ was calculated from equation (3.14) after preiterating the reduced density of the liquid phase from equation (3.6) using the SL parameters of the liquid mixture and $\mu^{\mathrm{V}}_{0,\mathrm{H_2O}}$ was calculated from equation (3.4) using the reduced entropy given in equation (3.13) with $C = 1$ after preiterating the reduced density of the vapor phase from equation (3.6) at the corresponding partial pressure and temperature using the SL parameters of water.

Furthermore, the influence of moisture on the SLE of the ASDs was also investigated. Since the calculation of the ternary SLE is influenced by the amount of moisture absorbed in the ASD, both the ternaries SLE and VLE need to be solved simultaneously as a solid-liquid-vapor equilibrium (SLVE). To elucidate the phases and components involved, the ternary system is schematically shown in Figure 3.3.

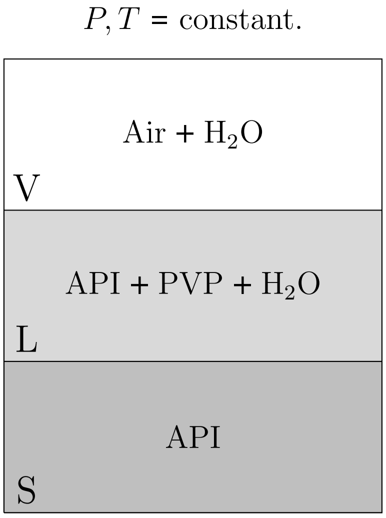

Figure 3.3: Schematic representation of the phase equilibria of a humid amorphous solid dispersion adapted from Prudic et al. [142]. The letters L, V and S denote the liquid, vapor and solid phases, respectively.

Since there is no component present in all three phases as shown in Figure 3.3, the material equilibrium needs to be split up into two parts regarding the already mentioned assumptions as

$$\begin{aligned}\mu^{\mathrm{L}}_{\mathrm{API}}(P,T,x^{\mathrm{L}}_{\mathrm{API}},x^{\mathrm{L}}_{\mathrm{H_2O}}) &= \mu^{\mathrm{S}}_{0,\mathrm{API}}(P,T)\\ \mu^{\mathrm{L}}_{\mathrm{H_2O}}(P,T,x^{\mathrm{L}}_{\mathrm{API}},x^{\mathrm{L}}_{\mathrm{H_2O}}) &= \mu^{\mathrm{V}}_{0,\mathrm{H_2O}}(P_{\mathrm{H_2O}},T),\end{aligned} \tag{3.39}$$

whereas both expressions need to be simultaneously satisfied. The material equilibrium of the API listed in equation (3.39) can be solved using equation (3.35) by calculating the chemical potential, $\mu_i^{\mathrm{L}}(P,T,x_i)$, using equation (3.17). Analogically, the material equilibrium of water must be solved using the chemical potential in the ternary mixture given in equation (3.17). It must be pointed out that the chemical potentials of both water and the API in the ternary liquid mixture are functions of the compositions of two components, in other words, the composition of the dry ASD must be specified. In the calculations performed in this work, the composition of the water-free ASD, the RH and the total pressure were specified, whereas the equilibrium temperature and water composition in the liquid ternary mixture were calculated. Moreover, the chemical potential of pure water in the vapor phase must be calculated at the partial pressure estimated from the specified relative humidity and the vapor pressure at the equilibrium temperature according to equation (3.38), whereas the required vapor pressure was calculated using the SL EOS as well.

3.5 Parameter fitting approach

Sanchez and Lacombe [23] fitted the pure component parameters to vapor pressure and saturated liquid density data 15 °C to 20 °C away from the critical point. Since vapor pressure data of polymers is unavailable, Sanchez and Lacombe [23] fitted the molecular parameters of polymers by a conventional nonlinear least-squares method applied to liquid density data above the glass temperature. This very same approach was used in this work to determine the SL parameters of PVP. Considering that vapor pressure data of APIs is also unavailable, the SL parameters of IBU and IND were fitted to PVT data above the glass temperature as well. Fitting the SL parameter set to PVT data using a least-squares method was straightforward in all cases and delivered an unambiguous parameter set as discussed in section 4.1, even when the starting values were varied.

On the other hand, the parameter sets of GRI and NAP were fitted to experimental SLE data in organic solvents as described in section 4.1, since no pure PVT data was found in the literature. The SLE equation (3.35) was solved using the SL EOS by calculating $\mu^{\mathrm{L}}_{\mathrm{API}}$ using equation (3.14) after preiterating the reduced density of the liquid phase from equation (3.6) using the SL parameters of the mixture. Moreover, $\mu^{\mathrm{L}}_{0,\mathrm{API}}$ was calculated from equation (3.4) by inserting the reduced entropy computed from (3.5) after preiterating the reduced density of the liquid phase from equation (3.6) using the SL parameters of the pure API. In the fitting approach, the temperature and pressure in equation (3.35) were specified and the molar fraction at equilibrium was iterated. Additionally, the fusion enthalpy and temperature were taken from the literature as explained in detail in section 4.1.

The objective function, $f(\mathrm{w}_{j,exp},\mathrm{w}_{j,calc})$, to simultaneously fit the SL parameters alongside the k_{ij} was built as follows

$$f(\mathrm{w}_{j,exp}, \mathrm{w}_{j,calc}) = \sum_{i}^{N} \left(1 - \frac{\mathrm{w}_{j,exp,i}}{\mathrm{w}_{j,calc,i}}\right)^2 , \tag{3.40}$$

where N is the number of experimental points available for each binary mixture, w_j is the mass fraction of component j and subscripts $_{exp}$ and $_{calc}$ denote experimental and calculated points, respectively.

The goal is to find the best SL parameter set (ρ_i^*, T_i^* and P_i^*) and k_{ij} which minimizes equation (3.40). First of all, the sensitivity of the SLE curve $T(x_i)$ to changes in all three SL parameters was tested. The position of the solubility curve alongside the x-axis is dominated by the value of T_i^*, whereas the curvature towards higher temperatures is dominated by ρ_i^* and the curvature towards lower temperatures by P_i^*. It is also known that the characteristic density ρ_i^* needs to be around the crystalline density [23]. For these reasons, the following algorithm was implemented:

1. Initial values for all three SL parameters were defined. ρ_i^* was set to the crystalline density, T_i^* was set to 400 K and P_i^* to 200 MPa. The last two initial values were arbitrarily chosen to be physically feasible. The binary interaction parameter k_{ij} contained in equation (3.12) was set to 1 for all mixtures.

2. T_i^*, P_i^* and ρ_i^* were successively iterated using the Newton-Raphson method (NR) to find the minimum value of the target function holding the other two SL parameters and the k_{ij} constant, until no variation in all parameters was achieved. The NR method used was a self-written version of the original algorithm including an attenuation factor.

3. The pre-iterated parameter set was then used to build the initial simplex required to run a Nelder-Mead minimization method [189]. Since there are three variables, i.e. T_i^*, P_i^* and ρ_i^*, an initial simplex with four parameter sets is required. It was built varying the SL parameters successively by 5 % down and up. The best four parameter sets from the six calculated were then selected as initial simplex.

4. A Nelder-Mead algorithm [189] was used to further optimize the parameter set. Once a minimum was reached, steps 2 to 4 were repeated until no change in all variables was achieved.

5. The k_{ij} was calculated as temperature-independent for each experimental point available.

6. A linear regression among all calculated k_{ij}s for a single binary mixture was performed and a temperature-dependent k_{ij} according to equation (3.12) was calculated.

7. Steps 2 to 6 were repeated until no variation in all parameters was achieved.

4 Results and discussion

The results obtained in this work and the comparison to experimental data, where possible, are presented in this chapter. The discussion regarding pure components is presented in section 4.1. Firstly, the estimation of SL parameters is discussed in section 4.1.1, where binary SLE data was used to fit the parameters of GRI and NAP. Then, the glass transition of pure components such as a brief discussion of their relaxation is presented in section 4.1.2. Furthermore, the influence of pressure on the glass temperature of pure components is briefly discussed in section 4.1.2.1. The phase diagrams including the SLE and glass temperature of dry ASDs are discussed in section 4.2. Three dry ASDs are discussed in detail, namely, IBU-PVP in section 4.2.1, IND-PVP in section 4.2.2 and NAP-PVP in section 4.2.3. Additionally, the water sorption in PVP and IND are presented in sections 4.3.1 and 4.3.2, respectively, whereas the water sorption in IND-PVP such as the phase diagrams including the glass temperature of the ternary system IND-PVP-water are presented and discussed in section 4.3.3. Finally, the SLE of NAP in water such as the water sorption of NAP are presented in section 4.3.4, whereas the results concerning the ternary system NAP-PVP-water are presented in section 4.3.5.

4.1 Pure components

4.1.1 Sanchez-Lacombe parameters

The SL parameters of PVP, IBU and IND were fitted to pure PVT experimental data from Shin et al. [146], Adrjanowicz et al. [147] and Adrjanowicz et al. [190], respectively. On the other hand and due to the lack of experimental data of pure components, the SL parameters of GRI and NAP were fitted to binary SLE data from Zhao et al. [150] and Mora and Martínez [152], Yan et al. [191], respectively. The SL parameters are listed in Table 4.1 and were fitted using the approach described in section 3.5.

Table 4.1: SL parameters of pure components fitted in this work.

Component	ρ_i^* [$\mathrm{kg\,m^{-3}}$]	T_i^* [K]	P_i^* [MPa]	$\bar{M}_i$ [$\mathrm{g\,mol^{-1}}$]	Exp. data used in fitting
PVP	1428.09	949.28	584.66	60×10^3	[146]
GRI	1573	664.46	596.68	352.77	[150]
IBU	1100.64	570.30	459	206.28	[147]
IND	1481.64	592.62	1198.19	357.79	[190]
NAP	1430	554.49	776.88	230.26	[116, 152, 191]

The comparison between the experimental [146] and calculated specific density of PVP is shown in Figure 4.1. The experimental data [146] was measured using the confining fluid method described in section 2.3.1.1. The molecular weight of the PVP used was 55 kg mol^{-1} and it was used as received without further purification [146]. Furthermore, Shin et al. [146] did not make any comments or measurements on the glass transition within the measured pressure from 10 MPa to 200 MPa and temperature from 445 K to 485 K. The calculations shown in Figure 4.1 were carried out neglecting any glass transition or presence of any other phase than a liquid. Equation (3.6) was solved using a liquid-like starting value for the reduced density at given T and P [146] and no equilibrium constraint was imposed to the system, whereas all isothermal experimental points were equally weighted during fitting. An excellent agreement between calculated and experimental data [146] was achieved and the SL parameters obtained are expected to deliver good results even at lower pressures $P < 10$ MPa. Since one of the goals of this work is to describe the phase diagram of ASDs at atmospheric pressure, the SL parameter set of PVP listed in Table 4.1 needs to be validated outside the pressure range where it was fitted. The validation is carried out indirectly by calculating the SLEs of PVP-API systems in section 4.2.

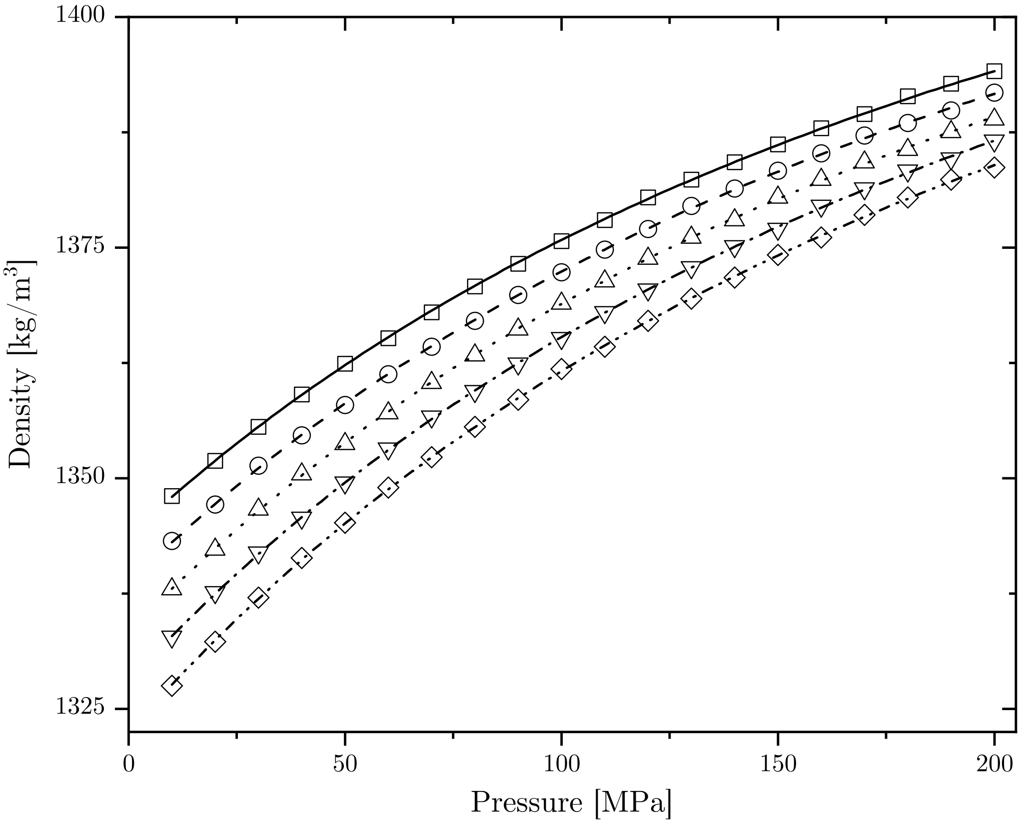

Figure 4.1: Experimental (□ 445 K, ○ 455 K, △ 465 K, ▽ 475 K, ◇ 485 K) [146] and calculated (—— SL at 445 K, – – SL at 455 K, ··· SL at 465 K, – · – SL at 475 K, – ·· SL at 485 K) specific density of PVP. The calculations with SL were carried out using the parameters listed in Table 4.1.

The characteristic temperature, T^*, fixes the position of the isotherms shown in Figure 4.1 alongside the y-axis, without having great influence on the curvature. Lower values of T^* shift the isotherms towards lower densities and vice versa. The characteristic pressure, P^*, influences the curvature towards higher pressures. Higher values of P^*

flatten the slope of the isotherms, whereas lower values of P^* increase the slope. The slope of the isotherms at pressures lower than 10 MPa hardly react to changes in the characteristic pressure. Furthermore, the characteristic density, ρ^*, has, as expected, the greatest influence on and is directly proportional to the calculated specific density alongside an isotherm. On the other hand, the influence of the molecular weight on the calculated density of PVP is marginal, since it only fixes the value of the segment number via $r = \bar{M}P^*/(RT^*\rho^*)$ [23], which is already in the order of 1000. This is only true, if the value is high enough $\bar{M}_{\mathrm{PVP}} > 1.5\,\mathrm{kg\,mol^{-1}}$. The choice of $\bar{M}_{\mathrm{PVP}}$ listed in Table 4.1 is justified in section 4.1.2.

The comparison between the experimental [147] and calculated specific density of IBU is shown in Figure 4.2.

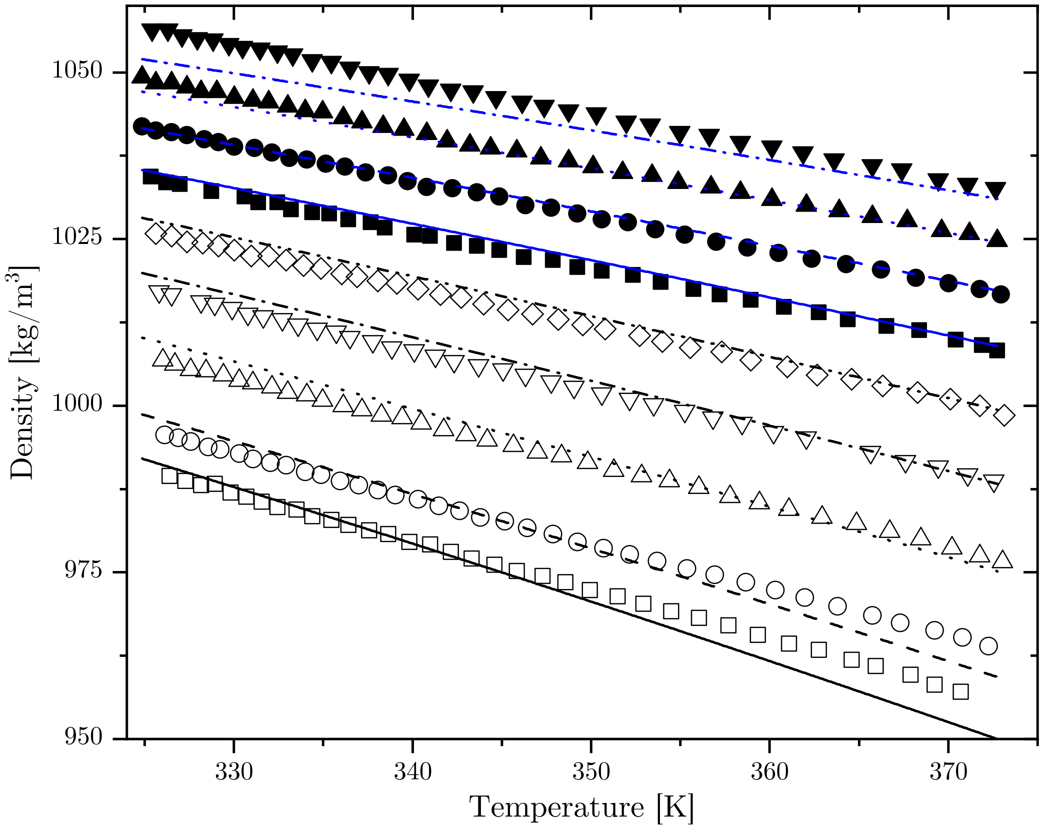

Figure 4.2: Experimental (□ 10 MPa, ○ 20 MPa, △ 40 MPa, ▽ 60 MPa, ◇ 80 MPa, ■ 100 MPa, ● 120 MPa, ▲ 140 MPa, ▼ 160 MPa) [147] and calculated (— SL at 10 MPa, – – SL at 20 MPa, ··· SL at 40 MPa, – · – SL at 60 MPa, – ·· SL at 80 MPa, — SL at 100 MPa, – – SL at 120 MPa, ··· SL at 140 MPa and – · – SL at 160 MPa) specific density of IBU. The calculations with SL were carried out using the parameters listed in Table 4.1.

Since IBU exhibits enantiomeric behavior, it is worth mentioning that Adrjanowicz et al. [147] used the racemic mixture between (S)-ibuprofen and (R)-ibuprofen for measurements. The method used in PVT measurements was also the confining fluid method using mercury as confining fluid [147]. Before each isobaric test run, the sample was cooled down from 105 °C to room temperature before being reheated up to the melt where the sample was pressurized to the next value [147]. In the same study, the glass temperature of IBU as a function of pressure was also derived from dielectric loss experimental data up to almost 350 MPa [147]. Hence, the SL parameters fitted to

PVT experimental data including pressures up to 160 MPa [147] should deliver good results for the glass temperature at high pressures. These results are discussed in section 4.1.2.

The agreement between experimental [147] and calculated data shown in Figure 4.2 is satisfactory, even though the slopes of the isobars are slightly incorrect for all pressures. For instance, the calculated density at 160 MPa is smaller than the experimental value towards lower temperatures, whereas the agreement improves towards higher temperatures. On the other hand, the calculated density at 10 MPa is in good agreement with the experiment at lower temperatures, whereas the discrepancy increases towards higher temperatures. For all pressures in between, the discrepancy is always lower than that at both the lowest and highest pressures being the lowest from 80 MPa to 100 MPa. These results are to be expected, since all isobars were weighted equally during fitting, which leads to a compromise in describing the middle pressures well at the expense of a higher discrepancy towards the extremes in both directions. The starting value of ρ^{*}_{IBU} used to fit the SL parameter set was equal to the crystalline specific density 1098.9 $\text{kg}\,\text{m}^{-3}$ at 25 °C and atmospheric pressure reported by Adrjanowicz et al. [147].

An increase in the characteristic temperature of IBU shifts the isobars towards higher specific densities and also flattens their slope towards higher temperatures. Furthermore, an increase in the characteristic pressure shifts the isobars towards lower specific densities, however, the slope of the isobars is marginally affected. Finally, as was the case for PVP, the characteristic density has the greatest influence on the isobars shown in Figure 4.2 shifting their value by over 100 $\text{kg}\,\text{m}^{-3}$ by a change of 10 % in ρ^{*}_{IBU}. The slopes are also not appreciably influenced by changes in ρ^{*}.

The experimental [190] and calculated specific density of IND is shown in Figure 4.3.

Adrjanowicz et al. [190] performed dielectric measurements at high pressures combined with PVT measurements of IND. The PVT measurements were performed isobarically over a wide temperature ($\approx 20 - 185$°C) and pressure ($0.1 - 200$MPa) range, in which IND exhibits both a glass transition and a solid-liquid phase transition [190]. The experimental set up used in measuring the PVT data of IND shown in Figure 4.3 was not described [190]. Both transitions divide the phase diagram (specific volume over temperature) in three regions, namely the glassy state at temperatures $T < T_G$, a supercooled liquid state at $T_G < T < T^{SL}_{0,\text{IND}}$ and a liquid region at $T > T^{SL}_{0,\text{IND}}$. The parameter set needs to be fitted to experimental data corresponding to a stable phase, as the plain SL EOS is not expected to deliver good results neither in the glassy nor in the supercooled state, since no physical background regarding both phenomena was included in its derivation. Therefore, only the data [190] above the fusion temperature were used to fit the SL parameter set of IND, namely the specific volume at temperatures above 160 °C at all studied pressures. Since the isobars were always measured at the same temperature values, the specific density can be plotted isothermally as a function of pressure as in Figure 4.3.

The experimental [190] and calculated specific density of IND shown in Figure 4.3 are in excellent agreement. A change in each of the characteristic parameters leads to the same behavior as previously discussed for PVP. The high value of the characteristic pressure P^{*}_{IND} listed in Table 4.1 denotes the strength of the intermolecular interactions of IND compared to PVP and the other studied APIs, as stated by Sanchez and

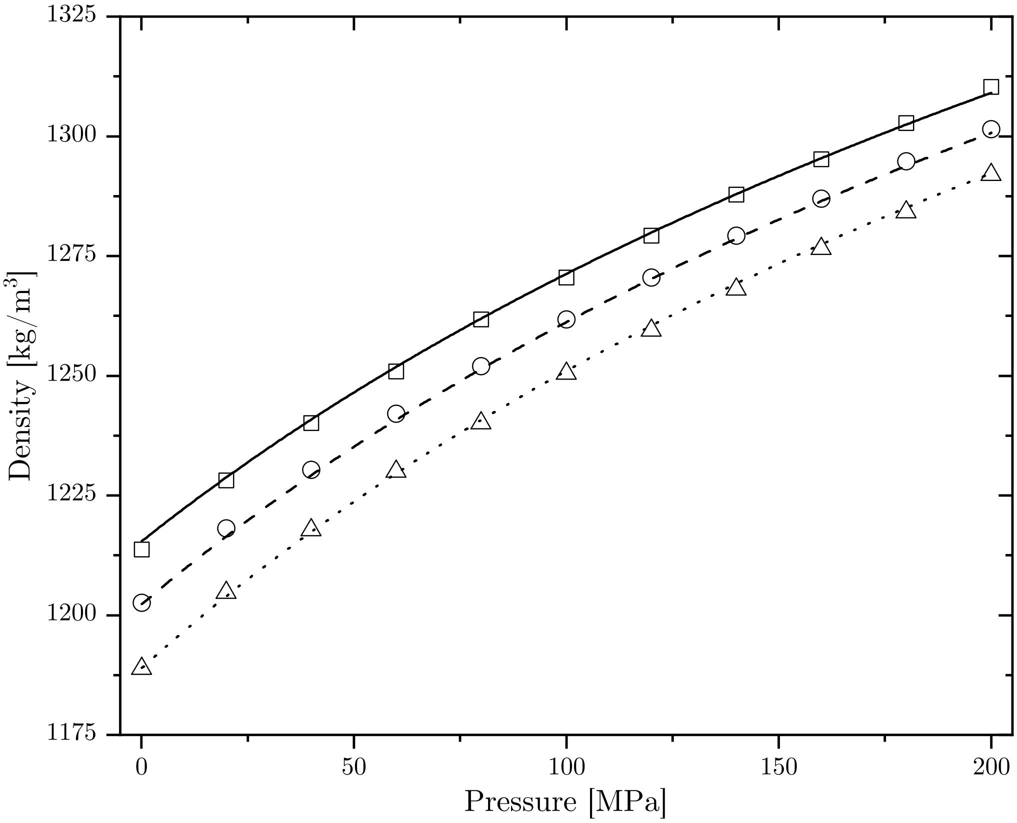

Figure 4.3: Experimental (□ 438.15 K, ○ 448.15 K, △ 458.15 K) [190] and calculated (— SL at 438.15 K, – – SL at 448.15 K, ··· SL at 458.15 K) specific density of IND. The calculations with SL were carried out using the parameters listed in Table 4.1.

Lacombe [24]. An initial value of ρ^*_{IND} equal to $1375\,\mathrm{kg\,m^{-3}}$ was used to fit the SL parameter set regarding the reported values of the IND crystalline density [4, 192].

The validation of the SL parameter set of IBU and IND and the calculation of the SL parameter sets of GRI and NAP required SLE binary calculations, for which the fusion properties of the pure APIs must be known. The fusion properties used in the SLE calculations of APIs throughout this work are listed in Table 4.2.

Table 4.2: Experimental fusion enthalpy and temperature of GRI, IBU, IND and NAP.

Component	$\Delta_{\mathrm{SL}} h_{0,i}$ [kJ mol^{-1}]	$T^{\mathrm{SL}}_{0,i}$ [K]	Reference
GRI	36.36	491.61	[150]
IBU	25.5	347.15	[149]
IND	38.1	433.35	[3]
NAP	30.3	428.7	[116]

The fusion properties of GRI were measured via DSC by the same authors [150] who reported the SLE data used in fitting of the SL parameter set. These experimental data [150] is in agreement with the data reported by Baird et al. [193].

The fusion properties of IBU were also measured via DSC and reported by one of the authors [149] who measured the SLE data. The reported data [149] is also in agreement with the data reported by Baird et al. [193].

On the other hand, the fusion properties of IND were measured via DSC by Pobudkowska et al. [157] and Martínez et al. [154], who also reported SLE data. Pobudkowska et al. [157] reported the fusion enthalpy and temperature as 75.4 kJ mol^{-1} and 433.6 K, whereas Martínez et al. [154] reported values of 55.10 kJ mol^{-1} and 433 K, respectively. Furthermore, Ruidiaz et al. [153] also reported SLE data of IND, however, they used the fusion properties reported by Forster et al. [194], namely 39.46 kJ mol^{-1} and 432.55 K, which were also measured via DSC. As can be seen from the fusion properties of IND reported [44, 154, 157, 193, 194], the fusion temperature appears to be clear, whereas the value of the fusion enthalpy is still controversial. On the other hand, the fusion properties reported by Mathers et al. [3] are in agreement with those of Forster et al. [194], Baird et al. [193], Martínez et al. [154] and Knopp et al. [44]. Furthermore, Mathers et al. [3] reported experimental SLE data of IND-PVP. Therefore, to ensure consistency and avoid confusion, all SLEs calculations including IND performed in this work were carried out using the fusion properties of IND reported by Mathers et al. [3] listed in Table 4.2.

Finally and since the fusion properties of NAP were not measured in the studies [152, 191] reporting SLE data, the fusion properties from Maxwell and Chickos [116] measured via DSC were used in the calculations of SLEs containing NAP. These fusion properties [116] are in agreement with the data also measured via DSC reported by Paus et al. [155], namely 31.5 kJ mol^{-1} and 429.47 K.

The SL parameter set of IBU needs to be validated at atmospheric pressure and lower temperatures, where the phase diagrams of ASDs are to be evaluated. Therefore, the SLEs of IBU in selected organic solvents were calculated using the parameter set of IBU listed in Table 4.1 and the SL parameters of organic solvents taken from the literature listed in Table 4.3. The binary interaction parameters k_{ij} of each pair IBU-organic solvent are listed in Table 4.4 alongside the experimental data to which they were individually fitted.

The experimental [149, 195] and calculated SLEs of IBU in selected organic solvents are shown in Figure 4.4. From the reported CAS number of IBU, it is apparent that Gracin and Rasmuson [149] also used the racemic mixture of both enantiomers for measurements. The equilibrium solubility of IBU in toluene, ethyl-acetate, chloroform, 2-propanol, acetone, ethanol and methanol was measured gravimetrically as described in section 2.3.2.1.

The SL parameter set of methyl-iso-butyl-ketone listed in Table 4.3 was fitted to vapor pressure [196] and saturated liquid density [197, 198] experimental data from 280 K to 380 K. Both the vapor pressure and saturated liquid density were equally weighted during fitting. The average relative deviations (ARDs) of both calculated properties compared to the experimental data were under 1.7 %.

On the other hand, Wang et al. [195] purified the purchased IBU used in measurements by recrystallization from an ethanol solution two times. It was not stated whether the obtained crystals were the racemic mixture of both enantiomers. The solubilities of IBU in 1-pentanol, ethyl-acetate, 1-butanol, 2-propanol, acetone and ethanol were measured at atmospheric pressure using a somewhat different approach than Gracin and Rasmuson [149]. The equilibrium solubility was measured using a laser beam directed towards the inner chamber of the vessel containing the solutions, when the intensity of the laser beam reached a maximum [195]. Additional IBU was added to the solution until the laser intensity did not return a maximum [195]. A detailed explanation of the experimental method can be found elsewhere [199].

The SL parameter set of iso-butanol listed in Table 4.3 was fitted to vapor pressure [200] and saturated liquid density [201] experimental data from 325 K to 395 K. Both the vapor pressure and saturated liquid density were equally weighted during fitting. The ARD of both calculated properties compared to the experimental data was under 2.4 %. The SLEs of IBU in 3-methyl-1-butanol [195] is not shown, since no experimental data on the saturated liquid density was readily found in the literature to fit the SL parameters of the solvent.

Table 4.3: SL parameters of organic solvents and water taken from the literature and fitted in this work. The SL parameters of the components marked with an asterisk were fitted to the experimental data listed under the references column.

Component	ρ_i^* [kg m^{-3}]	T_i^* [K]	P_i^* [MPa]	Reference	$\bar{M}_i$ [g mol^{-1}]
1, 4-dioxane	1163	519	536	[202]	88.11
1-butanol	863	494	320	[203]	74.12
1-octanol	872	552	301	[203]	130.23
1-pentanol	865	513	313	[203]	88.15
1-propanol	972	420	886.59	[23]	60.1
2-propanol	975	399	853.16	[23]	60.1
acetone	917	484	532.97	[23]	58.08
acetonitrile	842	565.28	734.38	[204]	41.05
chloroform	1688	511.77	456.07	[23]	119.38
cyclohexane	902	496.68	382.73	[23]	84.16
ethanol	963	413	1068.98	[23]	46.07
ethyl-acetate	1052	468	458	[23]	88.11
methanol	922	468	1201.72	[23]	32.04
methyl-acetate	1076	466	496.49	[23]	74.08
n-butyl-acetate	1003	498	394.15	[23]	116.16
toluene	966	543	402.26	[23]	92.14
water	1105	623	2687.14	[23]	18.02
iso-butanol*	1039.34	418.04	815.76	[200, 201]	74.12
methyl-iso-butyl-ketone*	986.65	420.02	577.92	[196–198]	100.16

Table 4.4: Fitted binary interaction parameters of mixtures API + organic solvent according to equation (3.12).

Mixture	$k_{ij,0}$	$k_{ij,T} \cdot 10^4$ [K^{-1}]	SLE exp. data
IND-1-octanol	1.0587	5.583	[157]
IND-ethanol	0.9962	0.058	[154, 157]
IND-ethyl-acetate	1.1722	−1.624	[154]
IND-1, 4-dioxane	1.1097	−0.733	[153]
IBU-toluene	0.9917	0	[149]
IBU-methyl-iso-butyl-ketone	1.01	0	[149]
IBU-ethyl-acetate	0.997	0	[149, 195]
IBU-iso-butanol	1.0355	0	[195]
IBU-1-pentanol	1.0133	0	[195]
IBU-1-butanol	1.1033	−3.245	[195]
IBU-chloroform	1.008	0	[149]
IBU-2-propanol	1.0454	0	[149, 195]
IBU-acetone	1.1221	−4.52	[149, 195]
IBU-ethanol	1.1813	−3.668	[149, 195]
IBU-methanol	1.2889	−7.391	[149]
GRI-iso-butanol	1.027	−1	[150]
GRI-1-butanol	1.0898	−2.25	[150]
GRI-1-propanol	1.0422	−1.275	[150]
GRI-ethanol	1.0677	−1.51	[150]
GRI-n-butyl-acetate	1.1222	−3.458	[150]
GRI-methanol	1.0911	−2.119	[150]
GRI-ethyl-acetate	1.0985	−2.906	[150]
GRI-methyl-acetate	1.0845	−2.525	[150]
GRI-acetonitrile	1.0732	−2.664	[150]
NAP-cyclohexane	0.9191	1.525	[152]
NAP-acetone	0.9915	−0.302	[191]
NAP-1-octanol	1.1251	−5.74	[152]
NAP-2-propanol	1.005	−0.38	[191]
NAP-chloroform	1.0715	−1.388	[152]
NAP-ethanol	1.0173	−0.558	[191]
NAP-ethyl-acetate	1.0873	−1.679	[191]
NAP-methanol	1.0604	−2.037	[191]

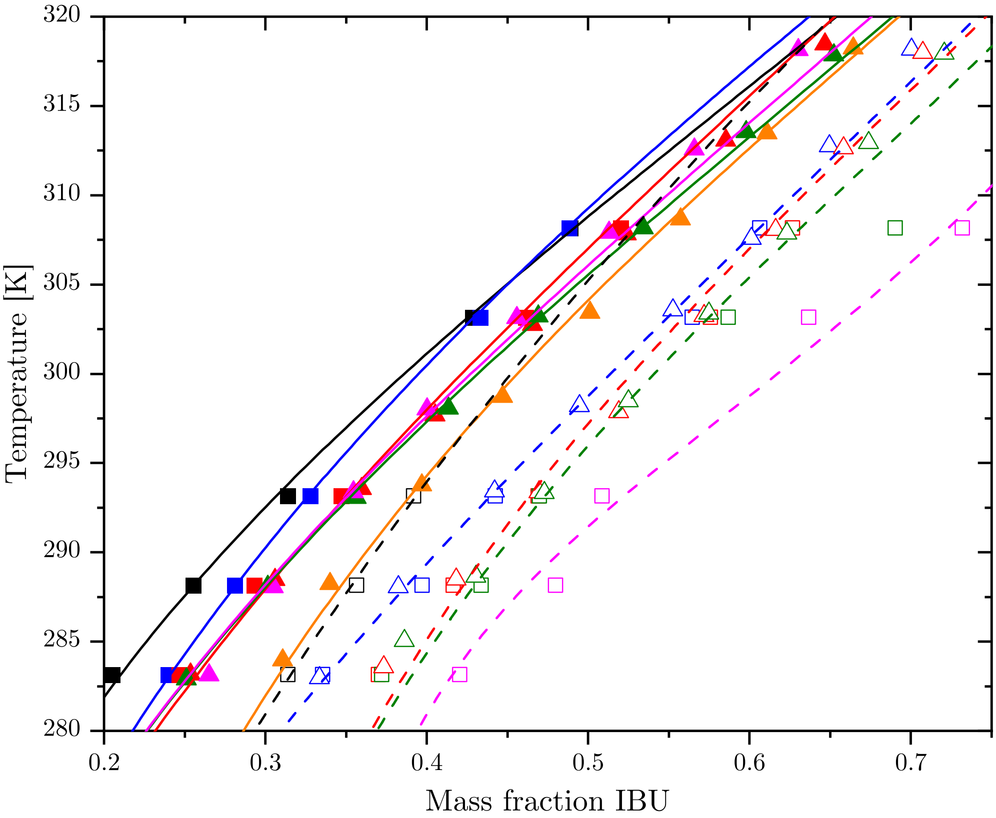

Figure 4.4: Experimental (■ toluene [149], ■ methyl-iso-butyl-ketone [149], ■ ethyl-acetate [149], ▲ ethyl-acetate [195], ▲ iso-butanol [195], ▲ 1-pentanol [195], ▲ 1-butanol [195], □ chloroform [149], □ 2-propanol [149], △ 2-propanol [195], □ acetone [149], △ acetone [195], □ ethanol [149], △ ethanol [195], □ methanol [149]) and calculated (— SL toluene, — SL methyl-iso-butyl-ketone, — SL ethyl-acetate, — SL iso-butanol, — SL 1-pentanol, — SL 1-butanol, – – SL chloroform, – – SL 2-propanol, – – SL acetone, – – SL ethanol, – – SL methanol) binary SLEs of IBU in organic solvents at 1 bar. The calculations with SL were carried out using the pure-component parameters listed in Tables 4.1 and 4.3, the k_{ij}s listed in Table 4.4 and the fusion properties listed in Table 4.2.

The experimental data [149, 195] are in good agreement with each other for ethyl-acetate and 2-propanol, whereas the data for ethanol shows a discrepancy of about 5 K at a mass fraction of IBU of approximately 0.7. Nevertheless, the experimental data of ethanol [149, 195] are in good agreement for lower mass fractions of IBU. The calculated SLEs in toluene, ethyl-acetate, 1-pentanol, chloroform and 2-propanol could accurately be described using a temperature-independent binary interaction parameter. Furthermore, the temperature dependence of the other SLEs is rather weak showing an always negative slope with a maximal absolute value lower than $7.5 \times 10^{-4}\,\mathrm{K}^{-1}$ for IBU-methanol. Two specific cases must be examined with more detail, namely the systems containing ethanol and methanol. The experimental data from Wang et al. [195] in ethanol is better described, due to the fact that all experimental points were weighted equally to fit the k_{ij} and three points from Wang et al. [195] are in the vicinity of the discrepancy, whereas only one point from Gracin and Rasmuson [149] is present. Furthermore, the calculated SLE of the system containing methanol exhibits a concave curvature from 285 K to 290 K and a convex curvature towards higher temperatures. This behavior is not expected to be physically feasible and its origin is purely mathematical. The experimental point between 285 − 290K [195] is an outlier which causes the objective function given to the minimization algorithm to be rather large, thus, the binary interaction parameter is further varied until the odd curvature is reached. For an accurate description of this SLE, which is outside the scope of this work, further experimental data to confirm or deny the accuracy of the outlier is required. Furthermore, both the SLEs of IBU in methyl-iso-butyl-ketone and iso-butanol are in excellent agreement with the experimental data [149, 195] by using a temperature independent k_{ij} under 4 % deviation from the geometric mixing rule. Finally, it can be seen that the parameter set of IBU fitted to PVT data [147] at higher pressures can be used to calculate SLEs at atmospheric pressure with high accuracy.

As for IBU and since the parameter set of IND was fitted to PVT data [190] at high pressures, the parameter set was validated by calculating the SLEs of IND in organic solvents at 1 bar. The SL parameters of the organic solvents involved are listed in Table 4.3 and the binary interaction parameters are listed in Table 4.4 alongside the SLE experimental data to which they were individually fitted.

The experimental [153, 154, 157] and calculated SLEs of IND in selected organic solvents are shown in Figure 4.5.

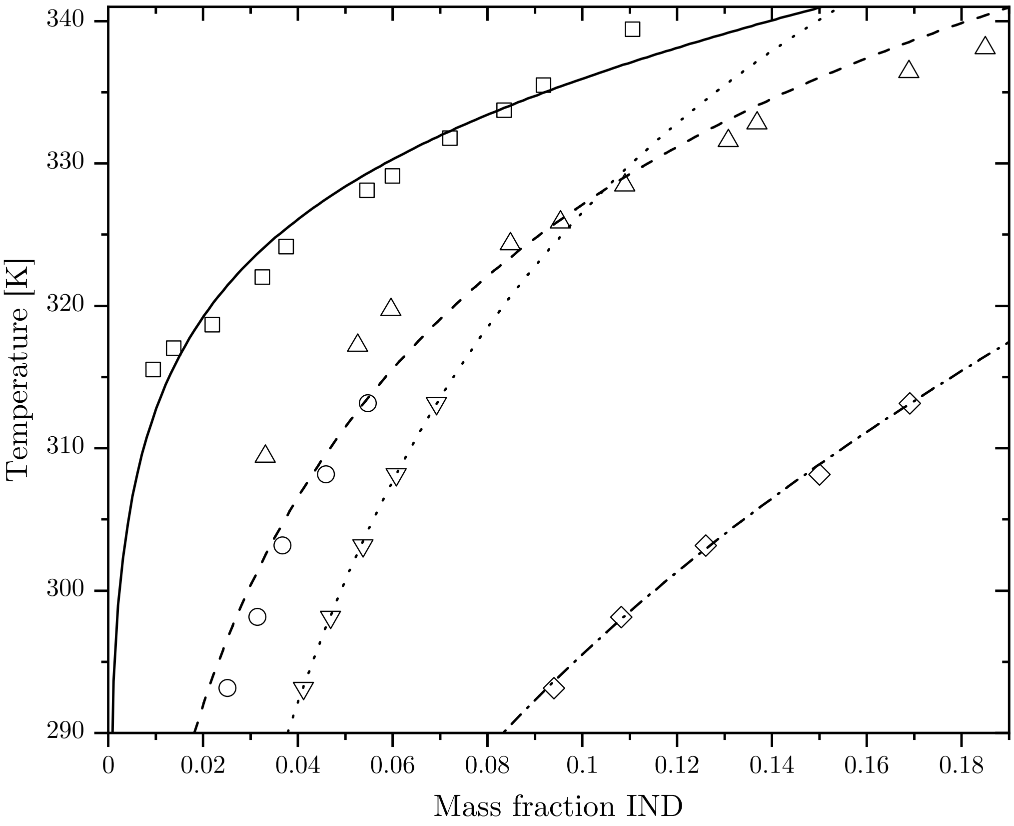

Figure 4.5: Experimental (□ 1-octanol [157], △ ethanol [157], ○ ethanol [154], ▽ ethyl-acetate [154], ◇ 1, 4-dioxane [153]) and calculated (— SL 1-octanol, – – SL ethanol, ··· SL ethyl-acetate, – · – SL 1, 4-dioxane) binary SLEs of IND in organic solvents at 1 bar. The calculations with SL were carried out using the pure-component parameters listed in Tables 4.1 and 4.3, the k_{ij}s listed in Table 4.4 and the fusion properties listed in Table 4.2.

Pobudkowska et al. [157] performed the solubility measurements via using UV spectophotometry by preparing mixtures of IND in water, 1-octanol and ethanol. Only the experimental data of IND in 1-octanol and ethanol reported by Pobudkowska et al.

[157] was used in the validation, since the SLE of IND-water is discussed in section 4.3.3.

Ruidiaz et al. [153] performed the solubility experiments of IND in 1, 4-dioxane-water mixtures, whereas Martínez et al. [154] used ethanol-water and ethanol-ethyl-acetate mixtures as solvents. Both sources [153, 154] used the UV spectrophotometry method described in section 2.3.2.2.

The experimental SLE data of IND in ethanol from Pobudkowska et al. [157] and Martínez et al. [154] have a discrepancy between 310 and $\approx 315\,\mathrm{K}$. Nevertheless, the general trend towards lower $T < 310\,\mathrm{K}$ and higher $T > 320\,\mathrm{K}$ temperatures could be well described, even though the fusion properties of Mathers et al. [3] were used. The binary interaction parameter of this mixture has a weak positive temperature dependence exhibiting values under 1 % deviation from the geometric mean mixing rule. Furthermore, the experimental SLE data of IND in 1-octanol [157] exhibits an almost linear trend between 315 and 340 K, whereas the calculation with SL shows a marked concave behavior. This leads to underestimating the equilibrium temperature at lower and higher IND mass fractions and to slightly overestimating it at intermediate IND mass fractions. The calculated SLEs of IND in ethyl-acetate and 1, 4-dioxane are in excellent agreement with the experimental data [153, 154] showing k_{ij}s with weak negative temperature dependence and deviations from the geometric mean mixing rule of about 10 %.

The SL parameter set of GRI was fitted to experimental SLE data in pure organic solvents [150], since no experimental data of the pure API was found in the literature. The results are shown in Figure 4.6.

Zhao et al. [150] used the stable polymorph of GRI without further purification to measure the SLEs in twelve organic solvents from which nine were used in this work, namely 1-butanol, iso-butanol, 1-propanol, ethanol, n-butyl-acetate, methanol, ethyl-acetate, methyl-acetate and acetonitrile using the gravimetric method described in section 2.3.2.1. The SLEs of GRI in propyl-acetate, iso-propyl-acetate and iso-butyl-acetate [150] are not shown, since no readily available experimental data on the saturated liquid density was found in the literature to fit the SL parameters of the organic solvents.

An excellent agreement could be achieved using temperature dependent binary interaction parameters with negative slopes in all cases. The highest absolute slope was exhibited by the mixture containing n-butyl-acetate and the lowest by the mixture containing ethanol. Only the SLE of GRI in 1-butanol shows a slight discrepancy compared to the experimental data [150], possibly due to the low solubility and the existence of two points outside the general trend. The parameter set of GRI is therefore suitable to calculate phase equilibria at atmospheric pressure and is used to calculate the glass temperature in section 4.1.2. Furthermore, the starting value of ρ^*_{GRI} used in fitting the SL parameter set was $1450\,\mathrm{kg\,m^{-3}}$ regarding the values of the GRI crystalline density reported in the literature [192, 205].

The SL parameter set of NAP listed in Table 4.1 was fitted to experimental SLE data in pure organic solvents [152, 191], since no data of the pure API was found in the literature. The comparison between experimental [152, 191] and calculated SLEs is shown in Figure 4.7.

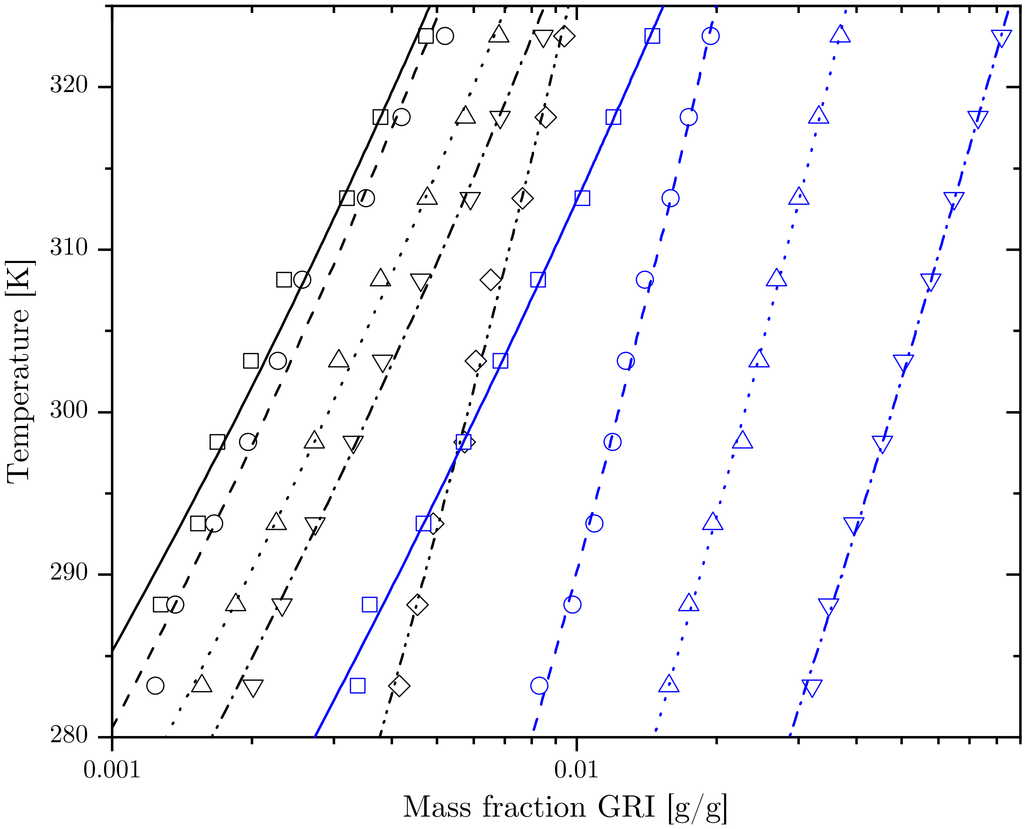

Figure 4.6: Experimental (□ iso-butanol, ○ 1-butanol, △ 1-propanol, ▽ ethanol, ◇ n-butyl-acetate, □ methanol, ○ ethyl-acetate, △ methyl-acetate, ▽ acetonitrile) [150] and calculated (—— SL iso-butanol, – – SL 1-butanol, · · · SL 1-propanol, – · – SL ethanol, – · · SL n-butyl-acetate, —— SL methanol, – – SL ethyl-acetate, · · · SL methyl-acetate, – · – SL acetonitrile) binary SLEs of GRI in organic solvents at 1 bar. The calculations with SL were carried out using the pure-component parameters listed in Tables 4.1 and 4.3, the k_{ij}s listed in Table 4.4 and the fusion properties listed in Table 4.2.

Mora and Martínez [152] performed the solubility measurements of NAP in several solvents via UV spectophotometry as described in section 2.3.2.2, from which 1-octanol, chloroform and cyclohexane were used in this work. The SLE of NAP in iso-propyl myristate [152] is not shown, since no readily available experimental data on the saturated liquid density was found in the literature to fit the SL parameters of the solvent.

On the other hand, Yan et al. [191] used a laser monitoring observation technique similar to the previously described method used by Wang et al. [195]. The experimental SLEs of NAP in acetone, methanol, ethanol, ethyl-acetate and 2-propanol [191] were used in this work. All three SL parameters were successively fitted alongside the binary interaction parameters to all the experimental data [152, 191] at once as described in section 3.5.

The experimental [152, 191] and calculated SLEs shown in Figure 4.7 are in excellent agreement with each other. The temperature dependence of the binary interaction parameters of mixtures containing acetone, 2-propanol, and ethanol were the weakest and always negative. Furthermore, the greatest temperature dependence of k_{ij} was exhibited by mixtures containing ethyl-acetate followed by cyclohexane. Mixtures containing cyclohexane and acetone have a negative deviation from the geometric mean rule, whereas all other mixtures containing NAP show a positive deviation. Moreover, the initial value of ρ^*_{NAP} used to fit the SL parameter set was equal to the specific crystalline density of NAP 1265 kg m^{-3} reported by Löbmann et al. [4].

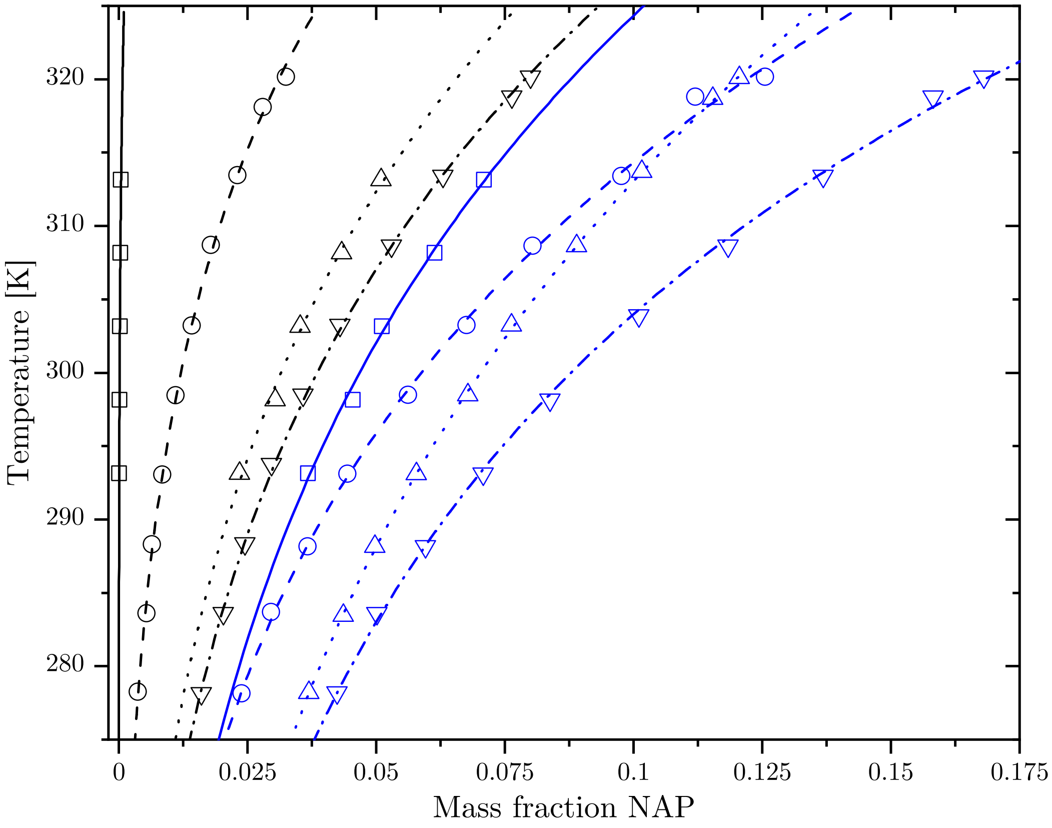

Figure 4.7: Experimental (□ cyclohexane [152], ○ acetone [191], △ 1-octanol [152], ▽ 2-propanol [191], □ chloroform [152], ○ ethanol [191], △ ethyl-acetate [191], ▽ methanol [191]) and calculated (—— SL cyclohexane, – – SL acetone, ··· SL 1-octanol, – · – SL 2-propanol, —— SL chloroform, – – SL ethanol, ··· SL ethyl-acetate, – · – SL methanol) binary SLEs of NAP in organic solvents at 1 bar. The calculations with SL were carried out using the pure-component parameters listed in Tables 4.1 and 4.3, the k_{ij}s listed in Table 4.4 and the fusion properties listed in Table 4.2.

4.1.2 Glass transition

The SL parameter sets listed in Table 4.1 were used to calculate the glass temperature of pure components via the GET as described in section 3.2. The calculated values of the characteristic temperatures such as the experimental data [3–5, 58, 106] to which the glass temperature of all pure components was fitted are listed in Table 4.5.

Since the measurement of the glass temperature via DSC depends on the heating/cooling rate used, the experimental glass temperatures reported in Table 4.5 were selected among reported values satisfying following criteria to ensure consistency: The experimental method used was mDSC or DSC and the heating rate, modulation amplitude and period were explicitly stated. In the case of PVP, only references with explicitly stated molecular weights were considered.

Table 4.5: Characteristic temperatures calculated via GET and experimental glass temperatures of pure components.

Component	k_p in equation (2.11) [-]	T_I^{calc} [K]	T_A^{calc} [K]	T_G^{calc} [K]	T_G^{exp} [K]
GRI	15.65	473.24	681.27	363.01	363 [5]
IBU	6.68	404.32	573.65	228.04	228 [106]
IND	14.51	425.48	628.50	316.54	316.55 [3]
NAP	12.56	395.49	571.99	278.19	278.19 [4]
PVP	10.61	685.45	1031.04	451.84	451.84 [58]

The experimental glass temperature of GRI [5] reported in Table 4.5 was measured via DSC using a heating rate of 10 K min^{-1} and was determined as the onset temperature of the glass transition event upon heating. This value is in excellent agreement and within the experimental uncertainty of other measurements performed via DSC at the same heating rate [170, 206–209]. A measurement performed via DSC at higher heating rates was also reported by Tombari et al. [210], however, it was not considered for the sake of consistency. Zhou et al. [206] also measured the glass temperature of GRI via DSC at different heating rates and obtained a similar value as Huang et al. [5], although the heating rate at which the reported T_G was measured was not explicitly stated. On the other hand, Willart et al. [211] measured the glass temperature of GRI via DSC at a heating rate of 5 K min^{-1} which led to a value of 358.15 K. Even though a lower heating rate leads to a value nearer to the actual glass temperature, no other experimental data measured at 5 K min^{-1} were found in the literature for comparison. Therefore, the value of T_G reported by Huang et al. [5] listed in Table 4.5 was selected to fit the k_p of GRI.

The glass temperature of racemic IBU reported by Dudognon et al. [106] was measured via DSC using a heating rate of 10 K min^{-1} and estimated as the midpoint of the glass transition event upon heating. This value is in agreement with the one reported by Johari et al. [212] measured using the same heating rate and estimated as the onset temperature of the glass transition event. The difference of 5 K between the measurements of Dudognon et al. [106] and Johari et al. [212] can be attributed to the different estimation of T_G from the thermographs. Furthermore, Brás et al. [213] also measured T_G via DSC using a heating rate of 5 K min^{-1} and calculated the same value of 228 K. Luebbert et al. [15] also measured the glass temperature of IBU. However, no details on the DSC measurement were given. Thus, the value reported by Dudognon et al. [106] listed in Table 4.5 was selected to fit the k_p of IBU.

Reported values regarding the T_G of IND measured via DSC at 10 K min^{-1} [3, 4, 115, 130, 137, 214–218] show a maximal difference of 6.6 K, an average of 316.98 K and a standard deviation of 2.09 K. The nearest value to the average was reported by Mathers et al. [3] and determined as the midpoint of the glass transition event upon heating. The values reported by Prudic et al. [60] and Doreth et al. [131] at heating rates of 2 K min^{-1} and 3 K min^{-1}, respectively, were not considered, as the measured glass temperature is higher than the average value of the measurements performed at 10 K min^{-1} [3, 4, 115, 130, 137, 214–218], even though the heating rate used for measurement is lower. Thus, the value reported by Mathers et al. [3] listed in Table 4.5 was selected to fit the k_p of IND.

The reported T_G of NAP was measured via DSC at 10 K min^{-1} [4] and at 2 K min^{-1} [58, 60]. The values reported by Löbmann et al. [4] and Paudel et al. [58] are in excellent agreement with and within experimental uncertainty from each other. The T_G reported by Löbmann et al. [4] listed in Table 4.5 was used to fit the k_p of NAP to ensure consistency among all the APIs regarding the heating rate.

The selection of a suitable glass temperature of PVP to fit the GET parameter k_p requires special attention, since the T_G of polymers is a function of the molecular weight. Therefore, a suitable molecular weight high enough to avoid the glass temperature to still change upon further increment of $\bar{M}_{\mathrm{PVP}}$ also has to be considered. For this purpose, the experimental [3, 43, 45, 57, 58, 60, 123–135] and calculated glass temperature of PVP as a function of the molecular weight is presented in Figure 4.8.

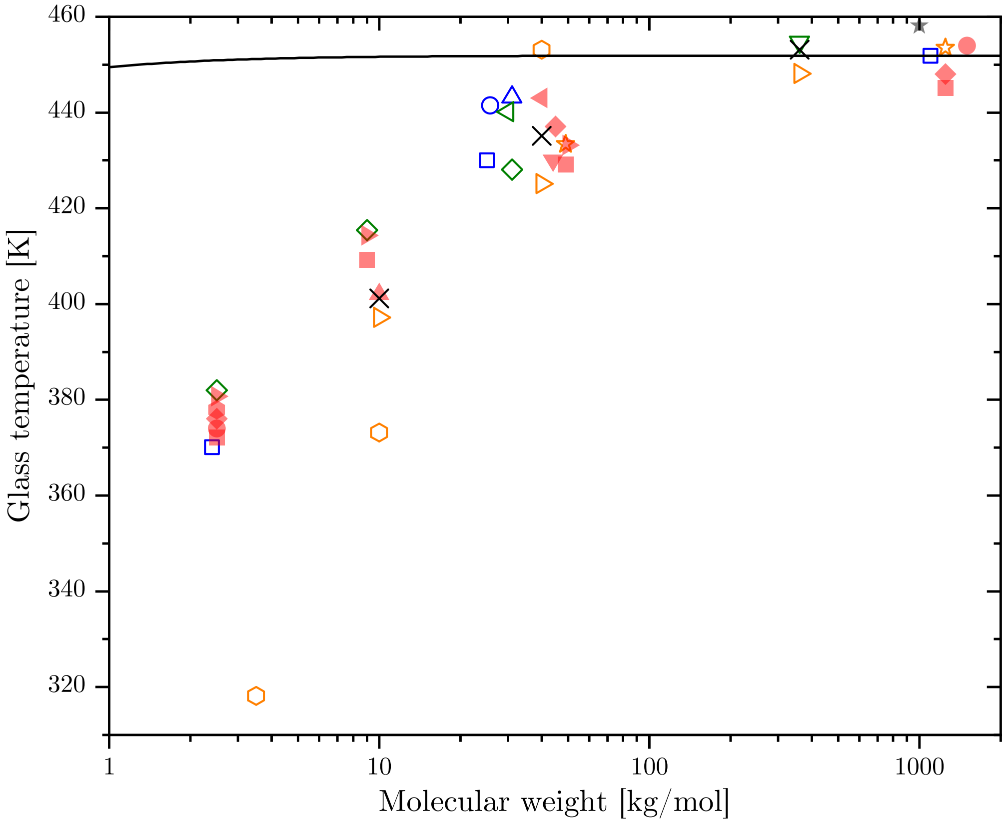

Figure 4.8: Experimental (□ [58], ○ [60], △ [134], ▽ [43], ◇ [131], ◁ [45], ▷ [132], ⬡ [124], ☆ [135], ■ [126], ● [127], ▲ [128], ▼ [57], ◆ [129], ◀ [133], ▶ [130], ⬢ [3], ★ [125], × [123]) and calculated (— SL) glass temperature of PVP over the molecular weight at 1 bar. The colors of the symbols represent the heating rates used in the DSC measurements, where 2 K min^{-1}, 3 K min^{-1}, 5 K min^{-1}, 10 K min^{-1} and 20 K min^{-1}. The SL parameters and k_p in equation (2.11) used in the calculations are listed in Table 4.1 and 4.5, respectively.

Figure 4.8 can be divided into four clusters, namely $\bar{M}_{\mathrm{PVP}} \approx 2.5$, ≈ 10, $\approx 11 - 100$ and > 100kg mol^{-1}. The data reported by Bell [124] is in disagreement with the rest of the experimental data at $\bar{M}_{\mathrm{PVP}} \approx 2.5$ and $\bar{M}_{\mathrm{PVP}} \approx 10$kg mol^{-1}, however, the T_G reported at higher molecular weights is within reasonable deviation from the other reported values. Moreover, all clusters, excluding the data from Bell [124], show a maximal deviation of around 20 K among them at comparable molecular weights. Since the goal is to choose a suitable experimental value of $T_{G,\mathrm{PVP}}$, it is appropriate to focus on the area where the molecular weight has a small influence on the glass temperature, i.e. $>$ 100 kg mol^{-1}. Even though these data were measured at different heating rates, the glass temperature obtained was very similar considering the arithmetical mean of $\approx$ 451.85 K and standard deviation of $\approx$ 3.8 K among values above 100 kg mol^{-1} shown in Figure 4.8. The value reported by Paudel et al. [58] at 1100 kg mol^{-1} listed in Table 4.5 is the nearest to the mean value and was therefore chosen to fit the k_p of PVP.

The values of k_p listed in Table 4.5 were used to calculate the reduced entropy density of PVP and the APIs GRI, IBU, IND and NAP. The results are shown in Figure 4.9.

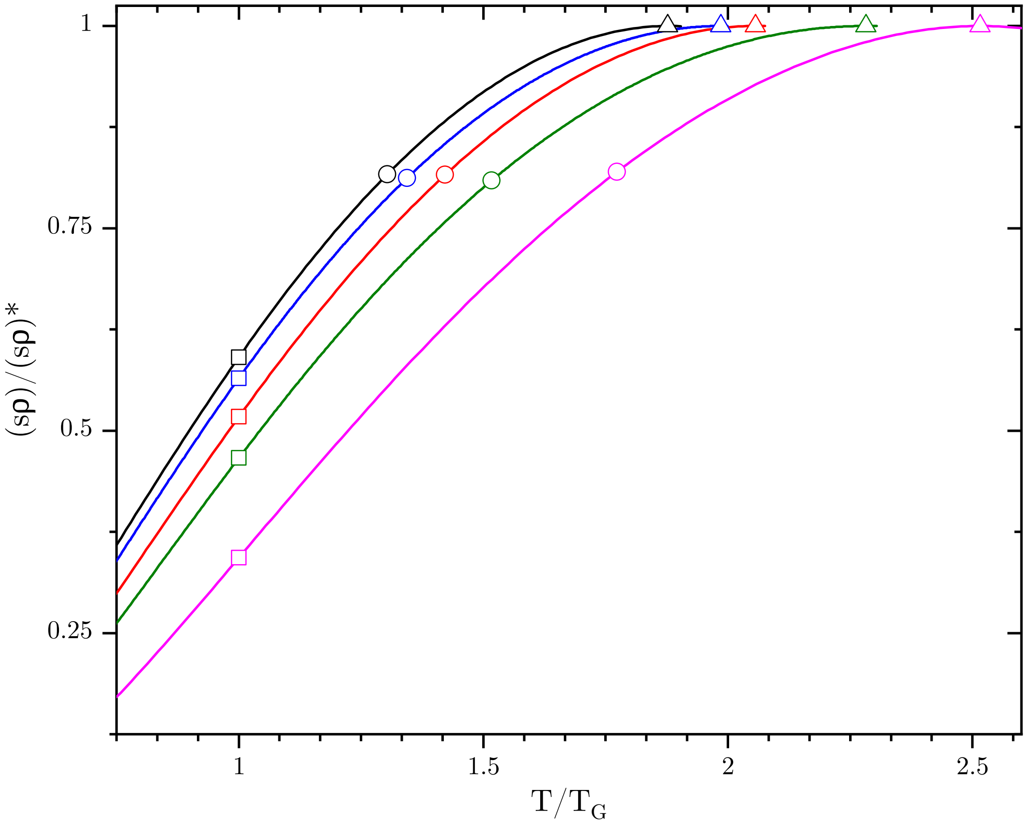

Figure 4.9: Calculated (— GET GRI, — GET IND, — GET NAP, — GET PVP, — GET IBU) reduced entropy density and characteristic temperatures (squares T_G, circles T_I, triangles T_A) at 1 bar. The y-axis was normalized by the respective highest value of the reduced entropy density, $(s\rho)^*$, and the x-axis by the calculated T_G of each pure component listed in Table 4.5. The calculations with GET were performed using the SL parameters listed in Table 4.1 and the k_p listed in Table 4.5.

As shown in Figure 4.9, IBU exhibits the highest difference between T_A and T_G. The calculated Arrhenius temperature was $\approx 2.5 T_{G,\mathrm{IBU}}^{calc}$ and almost 230 K higher than the fusion temperature [149]. On the other hand, GRI exhibits the lowest difference between T_A and T_G, as its calculated Arrhenius temperature is $\approx$ 1.9 times higher than its calculated glass temperature. Moreover, the T_A of GRI is almost 190 K higher than its fusion temperature [150]. Dudowicz et al. [9] have argued that T_A should be close to the fusion temperature provided that the fluid can crystallize. This is the case for

GRI, IND and NAP, as the melting temperatures listed in Table 4.2 are between the T_I^{calc} and T_A^{calc} listed in Table 4.5. The melting temperature of IBU [149] is almost 60 K lower than the calculated crossover temperature.

Dudowicz et al. [9] reported an almost linear increase in all characteristic temperatures with increasing molecular weight and a "saturation" to constant values at $\bar{M} \to \infty$. This same trend was obtained for PVP in the calculations performed in this work. Therefore, the calculated characteristic temperatures of PVP listed in Table 4.5 at the molecular weight reported in Table 4.1 are the limiting values according to Figure 4.8. An experimental confirmation of the Arrhenius temperature of polymers is also rather problematic, since the polymer would decompose at high temperatures hindering any experimental measurements [9].

The kinetics of the glass transition can be analyzed using the so-called Angell plot [219] shown in Figure 4.10 for PVP and all APIs. The components were categorized in strong and fragile glass formers, depending on the form of the function obtained in the Angell plot [219]. An Arrhenius behavior of τ_α with temperature would yield a straight line in Figure 4.10, whereas a non-Arrhenius behavior, often described by the VFTH for non-polymeric (e.g. [167, 168, 170, 171, 212, 220]) and the WLF equations for polymeric components (e.g. [132]), would result in an exponential behavior. The VFTH calculations using the reported constants listed in Table 4.6 are also shown in Figure 4.10 for comparison.

Table 4.6: VFTH equation (2.1) parameters of GRI, IBU, IND and NAP at 1 bar.

Component	τ_0 [s]	B_T [K]	T_0 [K]	Reference
GRI	1×10^{-14}	1995.84	308	[170]
IBU	1.2×10^{-14}	1426.81	187	[167]
IND	4×10^{-20}	3978	234	[168]
NAP	1.1×10^{-12}	1190.68	231.2	[171]

The relaxation times predicted by the GET for on one hand, GRI and IND, and on the other hand, NAP and PVP, are very similar. Furthermore, IBU exhibits the highest deviation from Arrhenius behavior. The relaxation time calculated via GET is not quite in agreement with the VFTH calculations using the parameters listed in Table 4.6 as shown in Figure 4.10. For instance, the relaxation time of IND at T_I^{calc} was overestimated in more than 5 orders of magnitude compared to the VFTH equation. Since the VFTH parameters were fitted to experimental dielectric relaxation data [168], the values calculated from the GET do not represent the experimental dielectric relaxation very well. The smallest deviation from the VFTH equation was shown by NAP, for which a deviation of less than 1 order of magnitude was achieved at temperatures close to T_A^{calc}. It is important to point out that the VFTH equation is suitable to describe the relaxation time at no more than 100 K below the glass temperature, as explained in detail elsewhere, e.g. [9, 53, 221]. As for PVP, the relaxation time calculated via GET is different by over 8 orders of magnitude at T_I^{calc} compared to the WLF equation with parameters $c_1 = 2.91$ and $c_2 = 208.2\,\mathrm{K}$ reported by Liu et al. [132] for a molar mass of $360\,\mathrm{kg\,mol^{-1}}$.

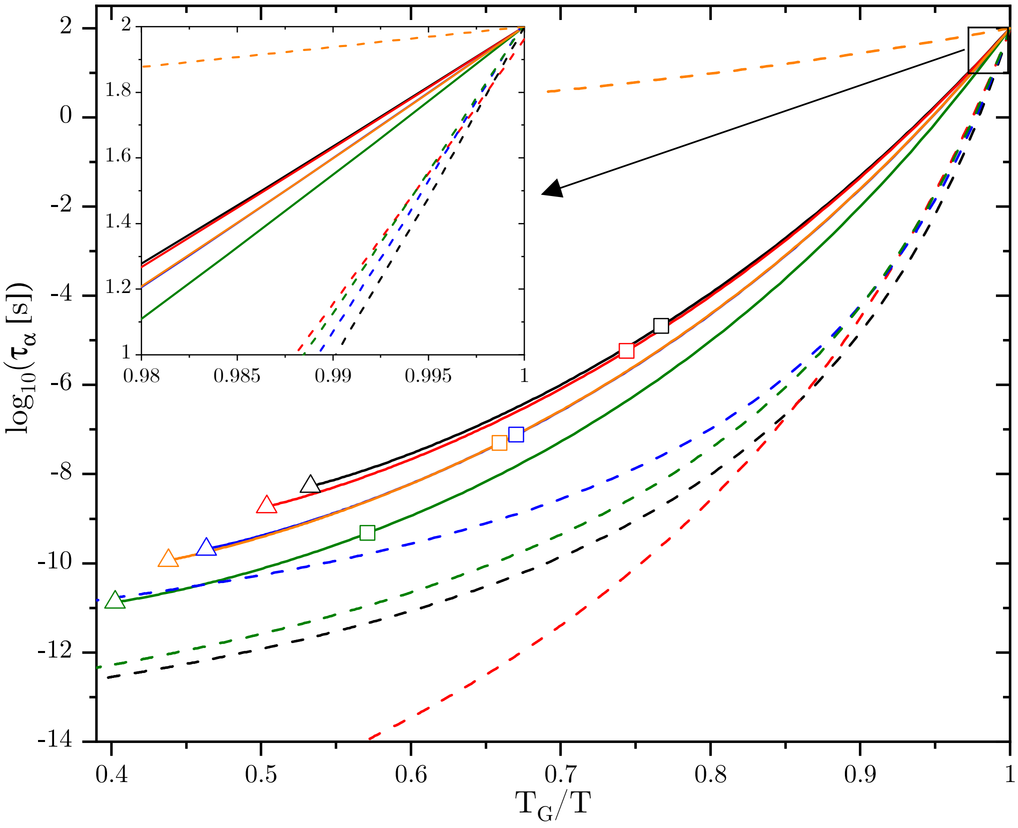

Figure 4.10: Angell [219] plot of APIs and PVP at 1 bar. Solid lines are GET calculations (— GRI, — IND, — NAP, — IBU, — PVP) with SL parameters listed in Table 4.1 and k_p listed in Table 4.5. Dashed lines were calculated using the VFTH equation (2.1) (– – GRI, – – IND, – – NAP, – – IBU) with parameters listed in Table 4.6 and the WLF equation (2.5) (– – PVP) with the parameters $c_1 = 2.91$ and $c_2 = 208.2\,\mathrm{K}$ reported by Liu et al. [132]. Squares denote the corresponding crossover temperature T_I and triangles the Arrhenius temperature T_A.

An estimate of the crossover temperature, at which the α and β relaxations appear to merge [73] as schematically shown in Figure 4.11, can be analytically computed for the APIs by equating the VFTH equation (2.1) and the Arrhenius equation

$$\tau_\beta = \tau_0 \exp\left(\frac{E_a}{RT}\right), \tag{4.1}$$

whereas the preexponential factor, τ_0, and the molar activation energy, E_a, are specific for the β relaxation and different from the values of the α relaxation. Equation (4.1) is used to calculate the β relaxation time, τ_β, described by the dashed line in Figure 4.11. The estimates obtained and reported here should be taken with care as a first approximation, since the values were calculated from fits of empirical equations to dielectric relaxation experimental data [167, 168, 170, 171] and may not be quite exact. The parameters of the VFTH (2.1) and Arrhenius equations (4.1) were taken from the same source, when possible, for consistency. A brief summary of the obtained T_I for IBU, IND, GRI and PVP is presented in the following paragraphs. Unfortunately, no experimental data on the β dielectric relaxation of NAP was found in the literature.

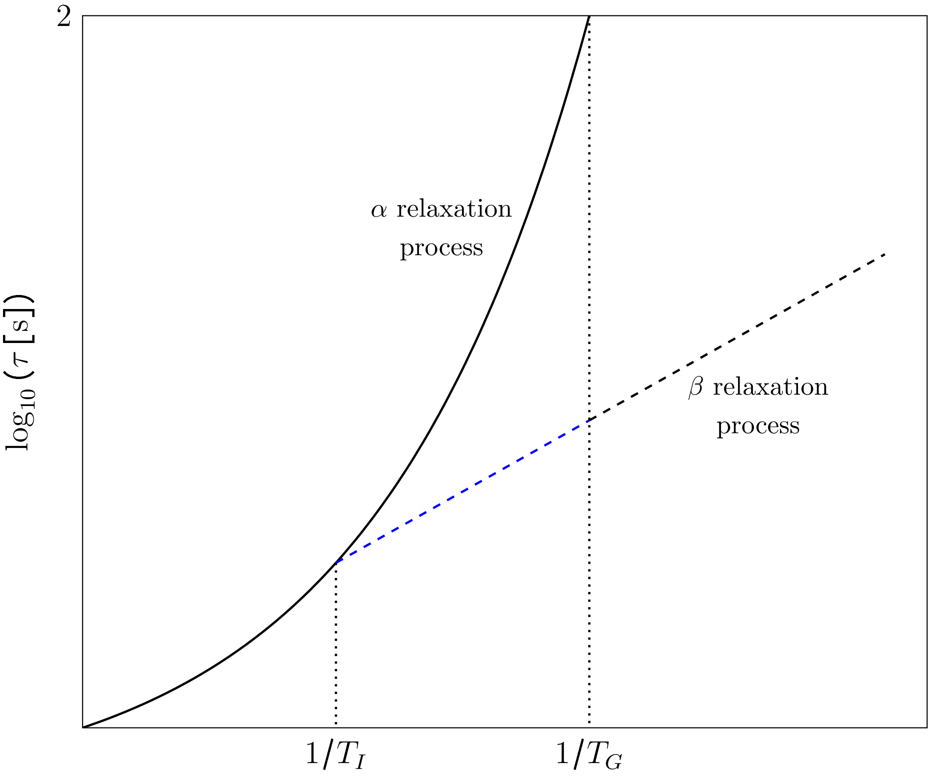

Figure 4.11: Qualitative representation of the estimation of the crossover temperature, T_I, from the α and β relaxation times. T_G is arbitrarily defined as the temperature at which the relaxation time of the α process equals 100 s.

The dielectric relaxation processes of IBU comparing experimental data from different sources [167, 169, 212] were reported by Bauer et al. [220]. Brás et al. [167] reported $E_a = 52\,\mathrm{kJ\,mol^{-1}}$ and $\tau_0 = 3 \times 10^{-16}\,\mathrm{s}$ for the β relaxation of IBU. Together with the VFTH parameters listed in Table 4.6, a value of $T_{I,\mathrm{IBU}} = 255.63\,\mathrm{K}$ was calculated. This leads to a difference of almost 150 K from the value calculated via GET listed in Table 4.5. Furthermore, Johari et al. [212] reported VFTH parameters of the α relaxation ($B_T = 1170\,\mathrm{K}$, $\tau_0 = 1 \times 10^{-13}\,\mathrm{s}$ and $T_0 = 192\,\mathrm{K}$) which in combination with the parameters of the β relaxation [167] lead to a very similar crossover temperature as the obtained using the VFTH parameters reported by Brás et al. [167].

Concerning IND, Carpentier et al. [222] reported VFTH parameters of the α relaxation ($B_T = 4264.25\,\mathrm{K}$, $\tau_0 = 2.6 \times 10^{-20}\,\mathrm{s}$ and $T_0 = 230.5\,\mathrm{K}$) and Arrhenius parameters of the β relaxation ($E_a = 56\,\mathrm{kJ\,mol^{-1}}$ and $\tau_0 = 9.5 \times 10^{-17}\,\mathrm{s}$) which lead to a $T_{I,\mathrm{IND}} = 401.09\,\mathrm{K}$, only 24 K lower than the calculated via GET listed in Table 4.5. Following the same procedure, the VFTH parameters reported by Wojnarowska et al. [168] listed in Table 4.6 were used together with the β relaxation parameters [222] to obtain a similar value of $T_{I,\mathrm{IND}} = 393.95\,\mathrm{K}$, which indirectly indicates that the measurements of the α relaxation [168, 222] are in agreement with each other, even though the reported VFTH parameters differ.

As for GRI, Kothari et al. [170] reported parameters for both the α ($B_T = 1996\,\mathrm{K}$, $\tau_0 = 1\times10^{-14}\,\mathrm{s}$ and $T_0 = 308\,\mathrm{K}$) and β relaxation ($E_a = 58.2\,\mathrm{kJ\,mol^{-1}}$ and $\tau_0 = 1\times10^{-10}\,\mathrm{s}$[1]). The obtained temperature is $T_{I,\mathrm{GRI}} = 380.27\,\mathrm{K}$, which is almost 93 K lower than the calculated value with the GET listed in Table 4.5.

The procedure described above for the APIs was also applied for PVP. The α relaxation was described using the WLF equation [132] and the β relaxation was reported by Cerveny et al. [223] using the Arrhenius equation with $E_a = 129.28\,\mathrm{kJ\,mol^{-1}}$ and $\tau_0 = 5.6\times10^{-17}\,\mathrm{s}$. The crossover temperature calculated by equating the WLF and Arrhenius equation produced a value lower than the corresponding T_G. The condition $T_I < T_G$ implies that the β relaxation time shown in Figure 4.11 would intercept the α relaxation time at a value higher than $\tau_\alpha = 100\,\mathrm{s}$, which is physically unfeasible. No other sources investigating the molecular dynamics of pure PVP both above and below the glass temperature were found in the literature for comparison. Cerveny et al. [223] argued that a measurement of the α relaxation via dielectric spectroscopy was not possible, as the high conductivity masked any process that was not very intense. On the other hand, Liu et al. [132] did not make any comments regarding the β relaxation of PVP, although their loss modulus was clearly measured at temperatures low enough to observe faster relaxation processes as shown in Figure 4B in their publication [132]. At this point, it is important to point out that both relaxation phenomena were measured using different techniques. For instance, Cerveny et al. [223] measured the dielectric loss spectra using BDS, whereas Liu et al. [132] measured the loss modulus using dynamic-mechanical analysis (DMA). Since both techniques should deliver similar results as the shear and dielectric relaxation times may be described by the WLF equation [30], it is not clear as to why the calculated crossover temperature is physically unfeasible.

It is now clear that the GET overestimates the relaxation time of GRI, IBU, IND and NAP. Furthermore, the crossover temperature is also always overestimated, given it is defined as the intersection between the α and β relaxations. The possible reasons behind this behavior may be analyzed departing from equation (3.20) and inserting the definition of the activation energy at high temperatures proposed by Dudowicz et al. [9]

$$\tau = \tau_0 \exp\left[\frac{k_p T_I \tilde{s}(T_A)\tilde{\rho}(T_A)}{T\tilde{s}\tilde{\rho}}\right]. \tag{4.2}$$

Following the procedure described in section 3.2, the first step to solve equation 4.2 consists on estimating the characteristic temperatures T_A from equation (3.18) and T_I from equation (3.19). Then, k_p is fitted to the experimental glass temperature meaning that T_I and $(\tilde{s}\tilde{\rho})^*$ already have an effect on the fitted value of k_p. Since the crossover temperature mathematically describes an inflection point in the function $T(\tilde{s}\tilde{\rho})$ and is always overestimated, the location of the inflection point must be offset towards higher temperatures. Therefore, the fitted k_p value corrects the activation energy scaled by $\tilde{s}(T_A)\tilde{\rho}(T_A)/(\tilde{s}\tilde{\rho})$ which in turn is overestimated alongside T_I by the SL EOS. This behavior can be explained using Figure 4.9. There are only two possibilities of reducing the estimated T_I and the maximum in the entropy density, namely, either shifting the whole profile towards lower temperatures sacrificing the predicted glass

---

[1] This value was not explicitly reported and was calculated from Figure 2a) in the original publication [170].

temperature, or increasing the slope of the curves between T_G and T_A making the glass transition event narrower while predicting the correct glass temperature. As the SL parameters of IBU and IND were fitted to PVT data, the liquid density should be correctly described. Assuming this is the case, the reduced entropy, and therefore the number of configurations available to the system, must be overestimated by SL and thus, the glass transition event becomes broader than it actually is. Furthermore, a decrease in the crossover temperature and the maximal entropy density would lead to a lower value of k_p. Consequently, the relaxation time in the Angell plot would show a steeper slope according to equation (4.2) and come closer to the VFTH fits. The results obtained for the reduced entropy using equation (3.13) are inherent to its derivation and cannot be influenced without introducing further parameters into the model. The description of the relaxation time could be improved by fitting the SL parameters directly to the experimental relaxation time, however, the thermodynamic behavior is not expected to be described very well thereafter. As the goal of the present work consists on correctly describing the phase behavior including thermodynamic phase equilibria, no further attempt at correcting the description of the relaxation time was made.

The previous analysis triggers the question as to why the relaxation time of PVP is not in agreement with the WLF fit using the parameters reported by Liu et al. [132] as shown in Figure 4.10. For instance, the fragility index of PVP predicted by the WLF equation is substantially lower than that of the APIs, whereas Mansuri et al. [224, 225] reported values of 75.8 and 105.6 for PVP-K12 and K-17, respectively. These values are near the ones calculated from the VFTH equation using equation (2.3) and the parameters listed in Table 4.6, namely $m_{\mathrm{GRI}} = 107$, $m_{\mathrm{IBU}} = 92$, $m_{\mathrm{IND}} = 83$, $m_{\mathrm{NAP}} = 101$. The GET predictions calculated via equation (3.22) are $m_{\mathrm{GRI}}^{calc} = 37$, $m_{\mathrm{IBU}}^{calc} = 46$, $m_{\mathrm{IND}}^{calc} = 37$, $m_{\mathrm{NAP}}^{calc} = 41$ and $m_{\mathrm{PVP}}^{calc} = 41.3$. Therefore, the relaxation time of PVP described using the parameters of Liu et al. [132] has an even higher deviation than the GET calculations compared to the values of Mansuri et al. [225]. Finally, a graphical estimation of m_{PVP}^{WLF} from the inset in Figure 4.10 would yield a value of approximately 5 which is lower than the minimal fragility index of an ideal glass former, i.e. 16.5 [226]. Thus, further experimental data is required to draw conclusions regarding the relaxation time of PVP over the temperature and the quality of the GET predictions.

4.1.2.1 Influence of pressure

The calculated reduced entropy, density and entropy density of IBU as a function of temperature was calculated at different pressures to investigate its influence on the glass transition as shown in Figure 4.12. The calculated glass temperature of IBU at all pressures investigated is located at an almost constant value of the entropy density as shown in Figure 4.12, however, T_G itself increases linearly with pressure. Furthermore, the crossover temperature also linearly increases, whereas the value of the entropy density at T_I decreases by increasing the pressure. On the other hand, the maximum of the entropy density flattens at higher pressures, however, the Arrhenius temperature is located at the same value of the entropy density at all pressures which agrees with LCT calculations performed by Dudowicz et al. [9]. T_A itself shows the same behavior as T_G and T_I linearly increasing with pressure. The reduced entropy and density exhibit an opposite pressure dependence as shown in Figure 4.12.

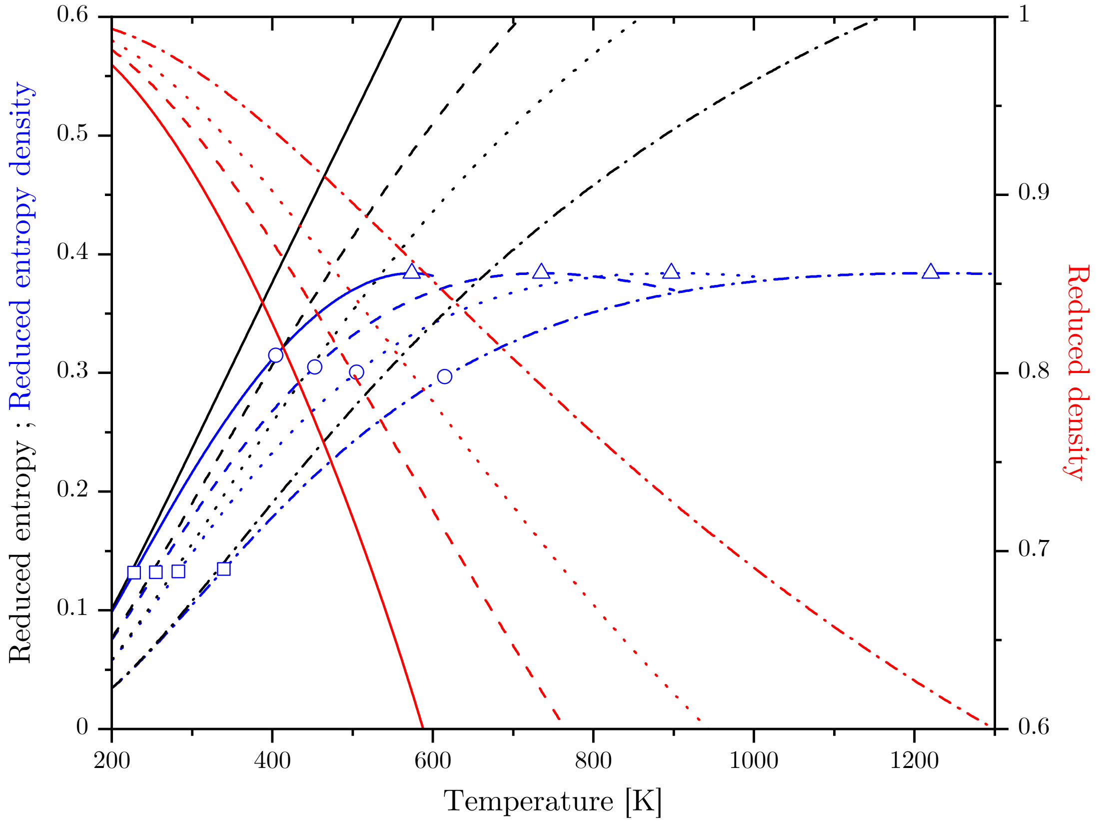

Figure 4.12: Calculated reduced entropy (—, – –, ···, – · –), density (—, – –, ···, – · –) and entropy density (—, – –, ···, – · –) of IBU over the temperature at 0.1, 50, 100 and 200 MPa, respectively. Squares, circles and triangles denote the glass, crossover and Arrhenius temperatures at the corresponding pressure, respectively. All calculations were performed using the GET with the SL parameters listed in Table 4.1 and the k_p in equation (2.11) listed in Table 4.5.

For instance, the entropy decreases upon increasing the pressure at constant temperature, whereas the density increases with pressure at constant temperature. Both predicted effects can also be explained by drawing an isotherm somewhere between $T_{G,B}$ and $T_{0,i}^{\mathrm{SL}}$ in Figure 2.1. The volume of the metastable liquid decreases by increasing the pressure alongside an isotherm which explains the density increase, as the total mass is constant. Furthermore, the system has lower available configurations at smaller volumes which explains the entropy decrease. Finally, the entropy density obeys the same behavior as the entropy suggesting that the depletion of available configurations to the system has a greater effect on the entropy density than the compressibility. Therefore, the entropy density must shift towards higher temperatures upon increasing the pressure as the prediction shown in Figure 4.12 also suggests.

Moreover, the influence of pressure on the relaxation time of IBU was predicted using the GET in combination with the SL EOS and compared to dielectric relaxation experimental data [147, 169] as shown in Figure 4.13. Adrjanowicz et al. [169] measured the dielectric relaxation of racemic IBU at 293 K and 378 K over the pressure using a self-made experimental set-up as described in detail by Roland et al. [227]. After identification of the α and β relaxation processes from the dielectric loss spectra, the α relaxation time was plotted isothermally over the pressure [169].

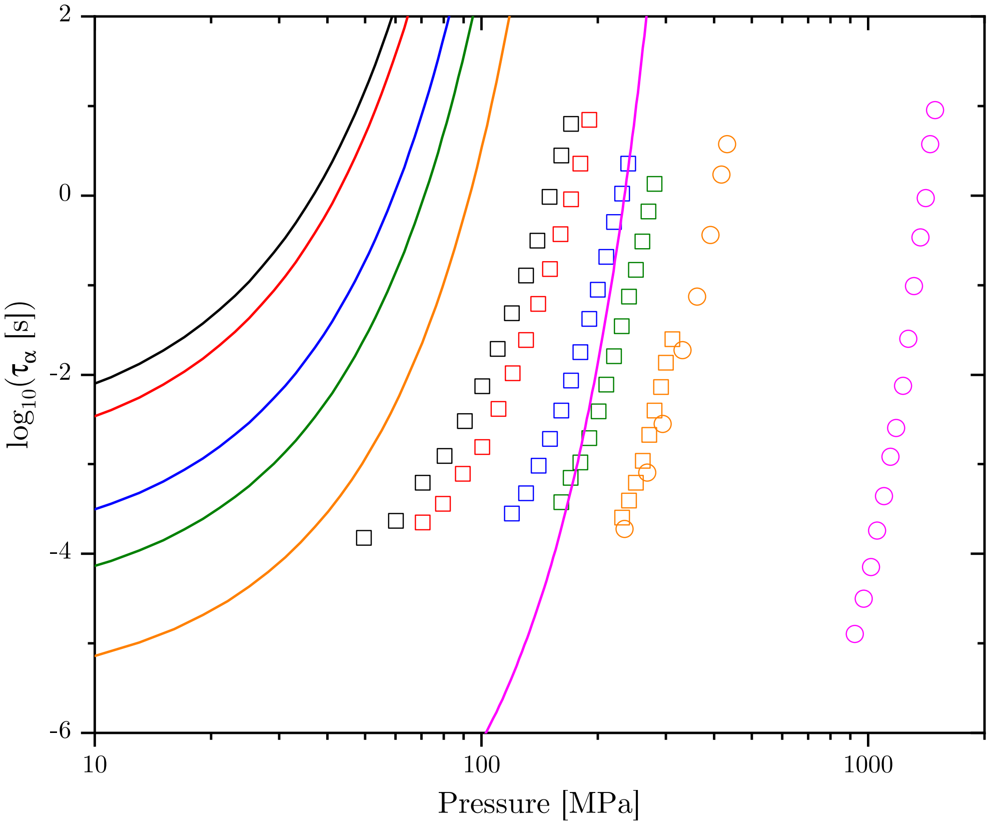

Figure 4.13: Isothermal experimental ((□ 260 K, □ 263.15 K, □ 273.15 K, □ 280.15 K, □ 293.15 K) [147] (○ 293 K, ○ 378 K) [169]) and predicted (— GET at 260 K, — GET at 263.15 K, — GET at 273.15 K, — GET at 280.15 K, — GET at 293.15 K, — GET at 378 K) segmental relaxation time of IBU over the pressure. The GET calculations were performed using the SL parameters listed in Table 4.1 and the k_p listed in Table 4.5.

Furthermore, the VFTH equation was fitted to the experimental relaxation time at 0.1 MPa, 412 MPa, 920 MPa and 1400 MPa and the glass temperature at the four different pressures was then calculated from the fitted parameters [169].

On the other hand, Adrjanowicz et al. [147] also used the experimental technique described by Roland et al. [227] to measure the dielectric relaxation of IBU over the pressure at constant temperature. The α relaxation time calculated from the dielectric loss spectra was then plotted isothermally at 360.15 K, 263.15 K, 273.15 K, 280.15 K and 293.15 K over the pressure [147]. The experimental data reported in both publications [147, 169] at 293 K is in excellent agreement with each other.

The predicted relaxation time shown in Figure 4.13 was calculated using equation (4.2) with the k_p fitted to the glass temperature of IBU at atmospheric pressure listed in Table 4.5. Although the GET prediction correctly predicts the shift of the relaxation time profile towards higher pressures upon increasing the temperature, it also overestimates the experimental relaxation time [147, 169] by several orders of magnitude. Dudowicz et al. [9] assumed a constant activation energy (equation (2.11)) based on the publication of Tabor [228], where the viscous flow of hydrocarbons was investigated. The assumption of a constant activation energy is only applicable to long-chained polymers as pointed out by Tabor [228]. Thus, the relative high overestimation of the relaxation time shown in Figure 4.13 is to be expected. However, not only the parameter k_p plays an important role in the prediction, but also the entropy density itself. The value of the entropy density is directly associated to the fitted SL parameter set, as it cannot be influenced without introducing additional variables into the model. By further examining Figure 4.2, it becomes clear that the fitted SL parameter set of IBU cannot describe the specific density at high pressures and low temperatures very well. Furthermore, the SL parameter set of IBU is expected to deliver results in reasonable agreement with experiments at pressures up to 160 MPa, however, the reported experimental relaxation time [147, 169] was investigated at considerably higher pressures. Therefore, the prediction falls outside the pressure range within which the SL parameters of IBU listed in Table 4.1 were fitted.

For the sake of completeness, the predicted glass temperature as a function of the pressure was calculated following the procedure described in section 3.2 and compared to the glass temperature calculated from dielectric relaxation experiments [169] as shown in Figure 4.14.

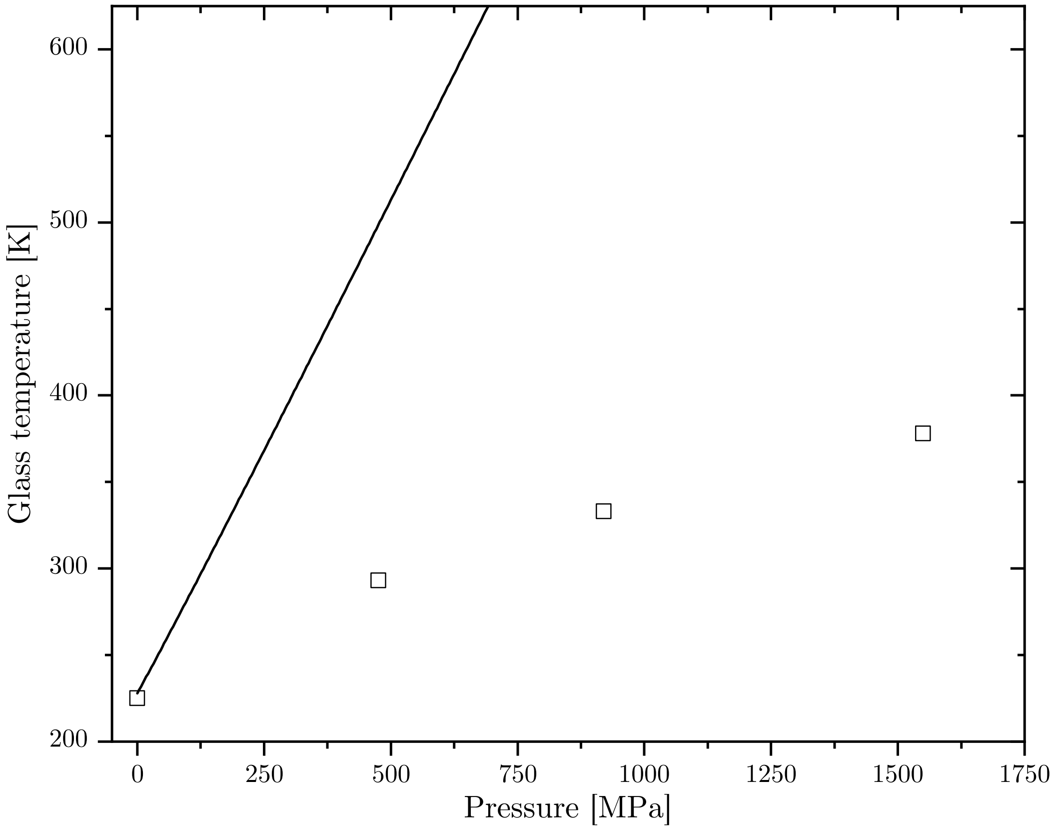

Figure 4.14: Experimental (□ [169]) and predicted (— GET) glass temperature of IBU over the pressure. The GET calculations were performed using the SL parameters listed in Table 4.1 and the k_p listed in Table 4.5.

The calculation of the glass temperature shown in Figure 4.14 fails at pressures over ≈ 750 MPa, since the SL EOS (equation (3.6)) does not possess any density roots above the pressure at which the close-packed density, ρ^*, is reached. Furthermore, the experimental glass temperature [169] is always overestimated and the overestimation increases with pressure. Both the experimental [169] and the calculated glass temperature exhibit a linear dependence on pressure, however, the predicted T_G as a function of pressure has a much higher slope than the experimental data [169].

As previously discussed, the slope of T_G over the pressure shown in Figure 4.14 may be influenced only by varying the k_p parameter, since the entropy density and crossover temperature contained in equation 4.2 are inherent to the model after fixing the SL parameter set. Of course, the low temperature relaxation time limit, τ_0, may also affect the glass temperature calculation. The answer to the question, whether τ_0 may be assumed pressure independent is outside the scope of this work. Nevertheless, it must be pointed out that a variation of τ_0 from 1×10^{-13} s to 1×10^{-11} s already causes a difference of ≈ 20 K in the predicted glass temperature using the GET.

The next goal consists in investigating whether a pressure independent k_p may be used when the SL parameter set was fitted to PVT data within the pressure range in which the experimental data is available. Since the experimental [190] and calculated PVT data of IND shown in Figure 4.3 are in excellent agreement with each other up until 200 MPa, comparing the predicted values of the relaxation time of IND to the experiment within this pressure range (0.1 − 200 MPa) [168] will elucidate the predicting capabilities of the GET.

The predicted and experimental relaxation time of IND deduced from dielectric relaxation experiments [168] over the pressure at constant temperature is shown in Figure 4.15.

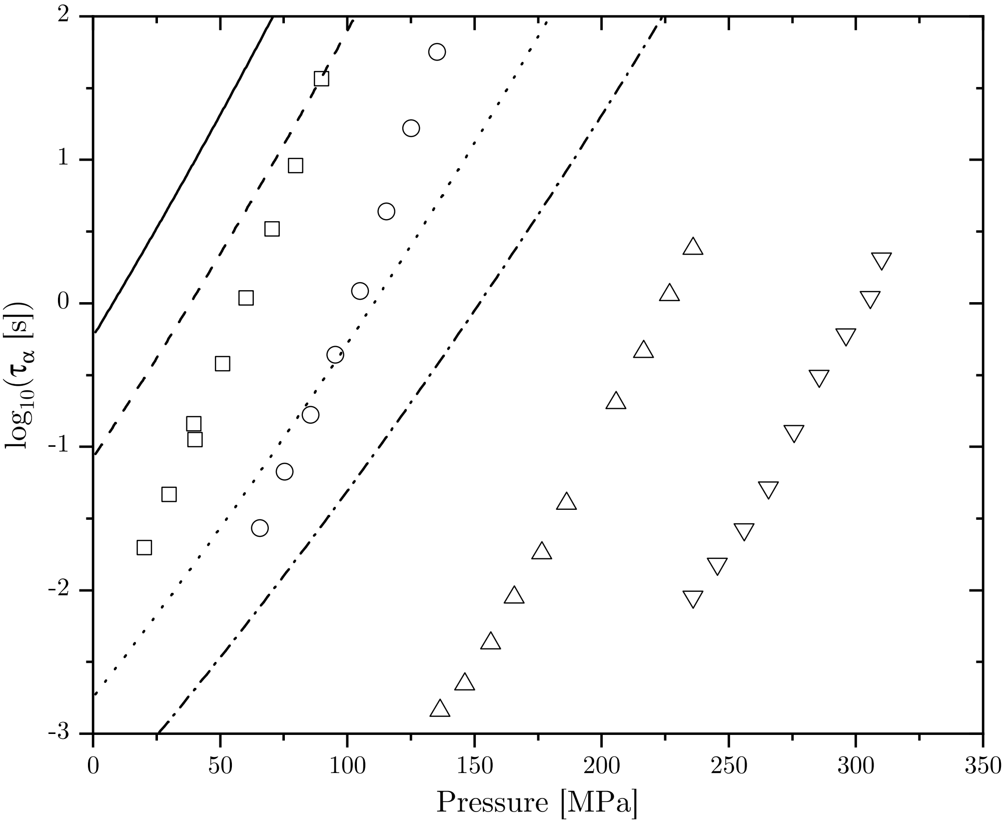

Figure 4.15: Isothermal experimental (□ 338.15 K, ○ 348.15 K, △ 372.15 K, ▽ 386.15 K) [168] and calculated (—— GET at 338.15 K, – – GET at 348.15 K, ··· GET at 372.15 K, – · – GET at 386.15 K) relaxation time of IND over the pressure. The GET calculations were performed using the SL parameters listed in Table 4.1 and the k_p listed in Table 4.5.

The prediction of τ_α for IND is in much better agreement than for IBU. At this point it must be pointed out that the x-axis of Figure 4.13 was plotted in logarithmic scale, whereas it is linear in Figure 4.15. Even though the relaxation times are still overestimated, the prediction using a pressure independent k_p is very good. Furthermore, it is also worth mentioning that the entropy, density and entropy density of IND exhibited the same tendency as shown for IBU in Figure 4.12 and are therefore not shown. Moreover, the experimental [168] and predicted glass temperature of IND over the pressure is shown in Figure 4.16.

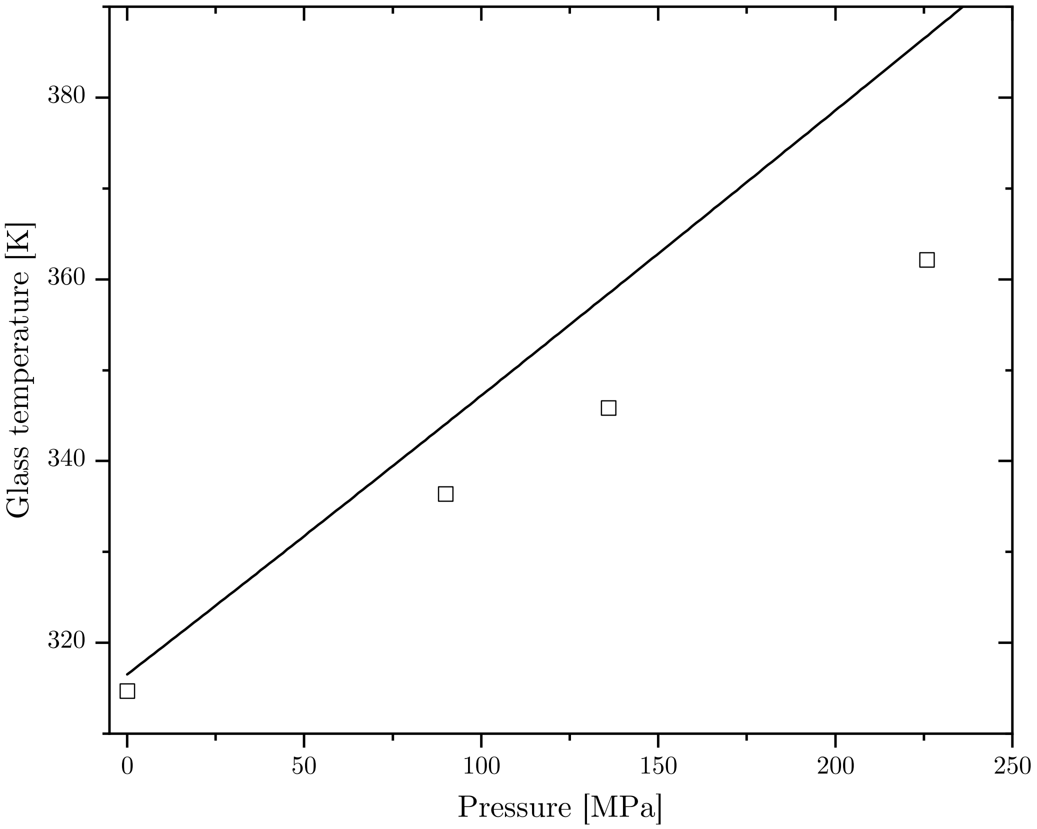

Figure 4.16: Experimental (□ [168]) and predicted (— GET) glass temperature of IND over the pressure. The GET calculations were performed using the SL parameters listed in Table 4.1 and the k_p listed in Table 4.5.

The predicted glass temperature is in surprisingly good agreement with the experimental values [168] as presented in Figure 4.16. At this point it is worth stressing out that the calculated T_G shown in Figure 4.16 is a prediction using the k_p fitted to the glass temperature of IND at atmospheric pressure listed in Table 4.5 and no further adjustable parameters were used. Thus, it can be concluded that the pressure range in which the SL parameter set is fitted plays a more important role than the pressure dependence of k_p. Consequently, the GET may be used to quantitatively predict the pressure dependence of $T_{G,\text{IND}}$ provided that the SL parameter set was fitted to PVT data within the same pressure range at which the prediction is to be attempted. However, whether this last statement is also applicable to other APIs needs to be further tested.

4.2 Amorphous solid dispersions

The results concerning the ASDs composed of PVP and IBU, IND and NAP, respectively, are presented in this section. Unfortunately, no binary experimental data of the ASD GRI-PVP was found in the literature to fit the k_{ij}. Vasanthavada et al. [229] found out that there is no appreciable solubility of crystalline GRI in PVP due to the non-existence of hydrogen bonding in the ASD formed with PVP confirmed via Fourier transform infrared spectroscopy (FTIR). Fitting the binary interaction parameter to the experimental glass temperature of the ASD would overshadow the prediction capability of the model and was therefore not attempted.

Furthermore, the activation energy, ΔE, contained in equation (3.20) and required to calculate the glass temperature of ASDs, was calculated using equations (3.23) and (3.24). However, the results obtained were very similar. Therefore, only the results regarding the T_G of ASDs obtained by using equation (3.23) are presented in this and following sections.

First, the binary interaction parameter of the binary mixtures PVP-API was fitted to experimental SLE data at atmospheric pressure. In all cases, the binary mixtures could be well described using a temperature-independent binary interaction parameter ($k_{ij,T}$ = 0 in equation (3.12)) as shown in Table 4.7. The k_{ij} of the ASD IND-PVP was fitted twice to different experimental data [3, 44, 60, 136] denoted as set A and B, since the SLE results obtained experimentally were different, even though no apparent difference in the components or methods was present. Furthermore, the specific glassy densities of PVP, IBU, IND and NAP used to calculate the glass temperature via the GT equation (2.6) are also presented in Table 4.7. A detailed description of the selection of experimental data, the calculations and the obtained results is presented in the following paragraphs.

Table 4.7: Binary interaction parameters in equation (3.12) of ASDs fitted to experimental SLE data and specific glassy densities used in the GT equation (2.6).

ASD	$k_{ij,0}$	Exp. SLE data	Component	$\rho_{0,i}^{gl.}$ [kg m^{-3}]
IBU-PVP	1.0955	[16]	PVP	1180 [58]
IND-PVP (set A)	1.1518	[3, 60, 136]	IBU	1050 [230, 231]
IND-PVP (set B)	1.2055	[44]	IND	1333 [232]
NAP-PVP	1.0908	[60]	NAP	1250 [58]

4.2.1 Ibuprofen + poly vinyl pyrrolidone

The experimental [16] and calculated SLE of IBU-PVP is shown in Figure 4.17. The fusion temperature and enthalpy reported by Luebbert and Sadowski [16] were measured by Luebbert et al. [15] and Gracin and Rasmuson [149], respectively. However and to ensure consistency, both the fusion temperature and enthalpy used in fitting the binary interaction parameter of IBU-PVP were taken from Gracin and Rasmuson [149] and are listed in Table 4.2.

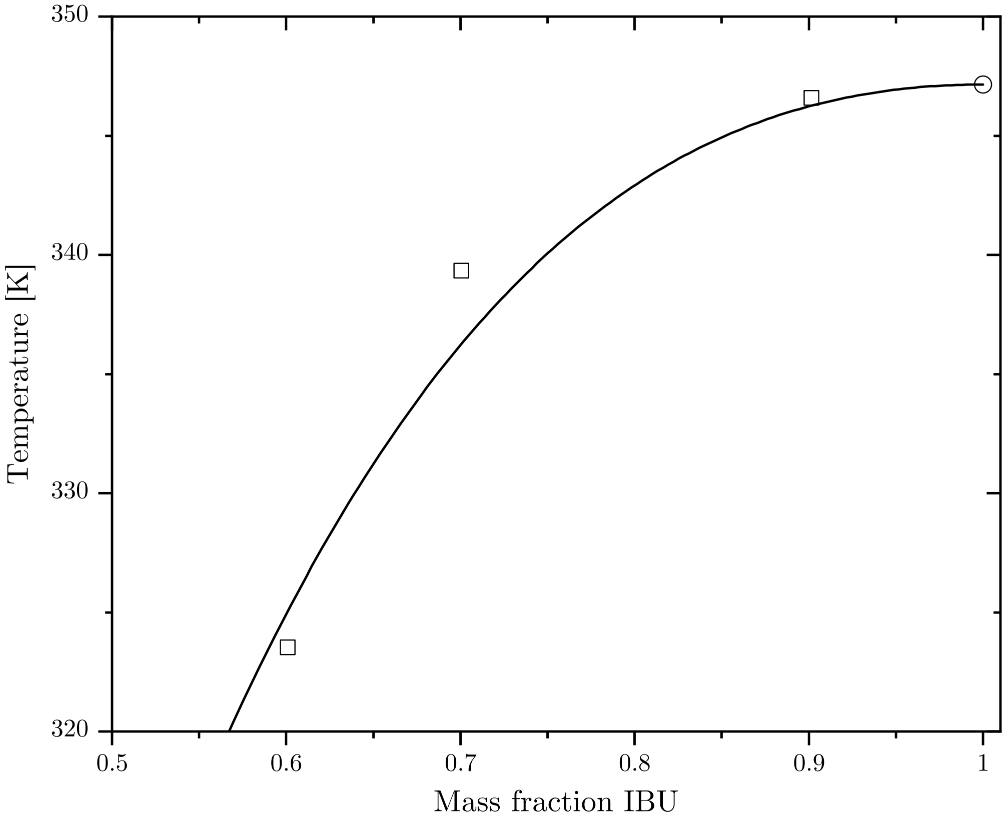

Figure 4.17: Experimental (□ [16], ○ [149]) and calculated (— SL) SLE of IBU-PVP at 1 bar. The calculations were carried out using the SL parameters listed in Table 4.1, the k_{ij} listed in Table 4.7 and the fusion properties listed in Table 4.2.

Luebbert and Sadowski [16] used racemic IBU and a PVP with molecular weight of 25.7 kg mol^{-1} to obtain the SLE experimental data shown in Figures 4.17. The fusion temperature was measured via mDSC by linearly extrapolating the measured onset temperature of the fusion event at heating rates of 1 K min^{-1}, 2 K min^{-1} and 5 K min^{-1} to a zero heating rate [16].

The calculated SLE shown in Figure 4.17 describes the experimental data [16] well, even though only three data points were reported. The solubility of IBU is slightly underestimated at mass fractions of IBU around 0.7, however, the slope towards higher mass fractions is in very good agreement with the experiment [16]. The binary interaction parameter obtained describes a rather small deviation from the geometric mean. The fitted k_{ij} can now be used to predict the glass temperature of the dry ASD.

The phase diagram describing the glass temperature such as the SLE of IBU-PVP is shown in Figure 4.18. The density of glassy PVP listed in Table 4.7 was measured via He picnometry for a PVP with molecular weight of 1100 kDa by Paudel et al. [58]. The experimental glassy density of PVP [58] is within experimental uncertainty of the values reported by Knopp et al. [44] and Zhang and Zografi [127], which were both also measured using He picnometry for PVPs of similar molecular weight ≈ 1100 kg mol^{-1}. On the other hand, the glassy density of IBU used in the GT calculations was assumed by Marsac et al. [231] ($1050\,\mathrm{kg\,m^{-3}}$) as 5 % less than the crystalline density reported by Sun [230].

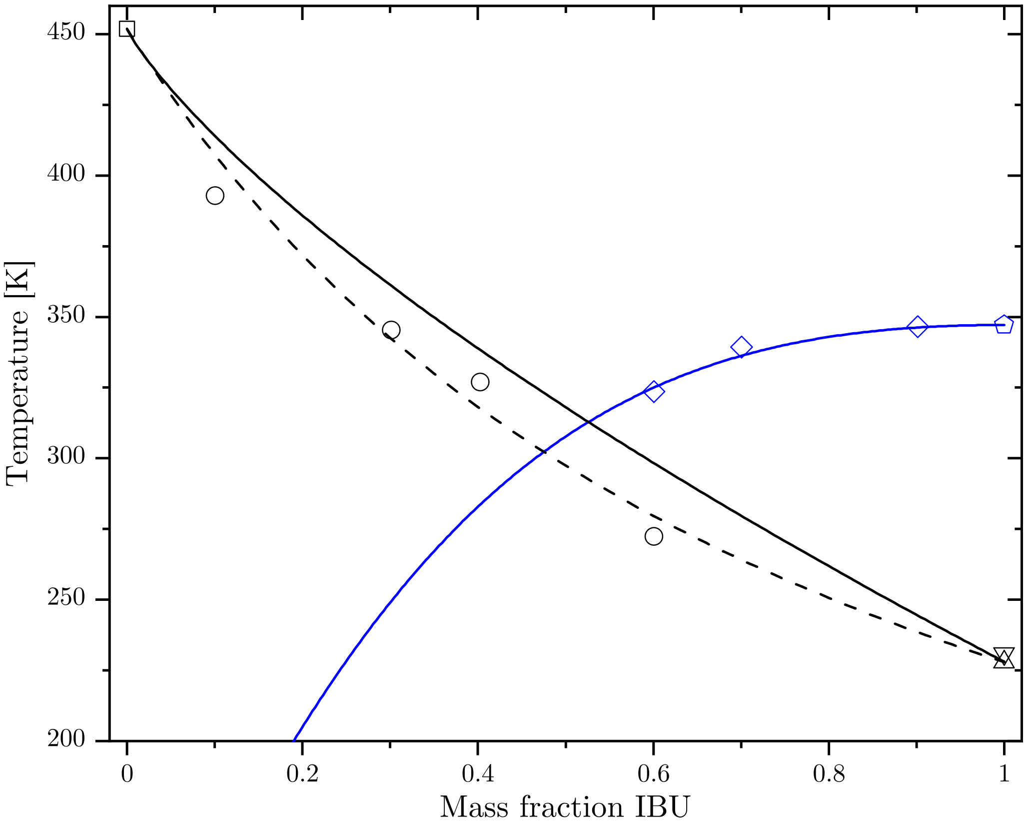

Figure 4.18: Experimental glass temperature (□ [58], ○ [16], △ [106], ▽ [15]), experimental SLE (◇ [16], ⬠ [149]), calculated glass temperature (— GET, – – GT) and calculated SLE (— SL) of IBU-PVP at 1 bar. The calculations with GET and SL were carried out using the SL parameters listed in Table 4.1, the k_{ij} listed in Table 4.7, the k_p listed in Table 4.5 and the fusion properties listed in Table 4.2. The GT calculations were performed using the experimental glass temperatures of the pure components listed in Table 4.5 and the glassy densities listed in Table 4.7.

The experimental glass temperature of the ASD [16] shown in Figure 4.18 was measured via mDSC upon heating from the reversing heat flow, however, no further details on the heating rate, period or amplitude were stated. Moreover, Luebbert and Sadowski [16] stated that the measured glass temperature did not depend on the heating rate used. No further experimental data on the glass temperature of the ASD were found in the literature for comparison.

The GT calculation, which require much less computational effort, is better than the GET prediction. However, it is worth mentioning that the calculation performed via GET is a prediction without any additional fitted parameters to the experimental glass temperature of the ASD [16]. Thus, a single EOS capable of correctly describing the thermodynamics of the mixture, such as the SL EOS, may be used in combination with the GET to predict the glass temperature of the ASD IBU-PVP in good agreement with the experiment [16].

Following the theoretical description of the phase diagrams of ASDs presented in chapter 1, the ASD IBU-PVP may contain up to ≈ 40 % weight of IBU at room temperature to form a mixture located under the glass temperature line and metastable against recrystallization as shown in Figure 4.18. However, the ASD containing 40 % weight IBU at 300 K has to relax to its equilibrium liquid state at some point in time. Whether this relaxation time is higher than the shelf life (approximately 2 years) cannot be examined with the theory developed here without incurring in further crude assumptions, therefore, the stability analysis of the ASDs was not theoretically investigated in this work. Luebbert and Sadowski [16] investigated the stability of the ASD against recrystallization. From their Figure 7(b) [16] can be concluded that the formulation containing 60 % weight of IBU is stable against recrystallization for up to approximately 2 years if stored at dry conditions and room temperature, which is in agreement with the GET prediction presented in Figure 4.18.

4.2.2 Indomethacin + poly vinyl pyrrolidone

The experimental [3, 44, 60, 136] and calculated SLE of IND-PVP is shown in Figure 4.19.

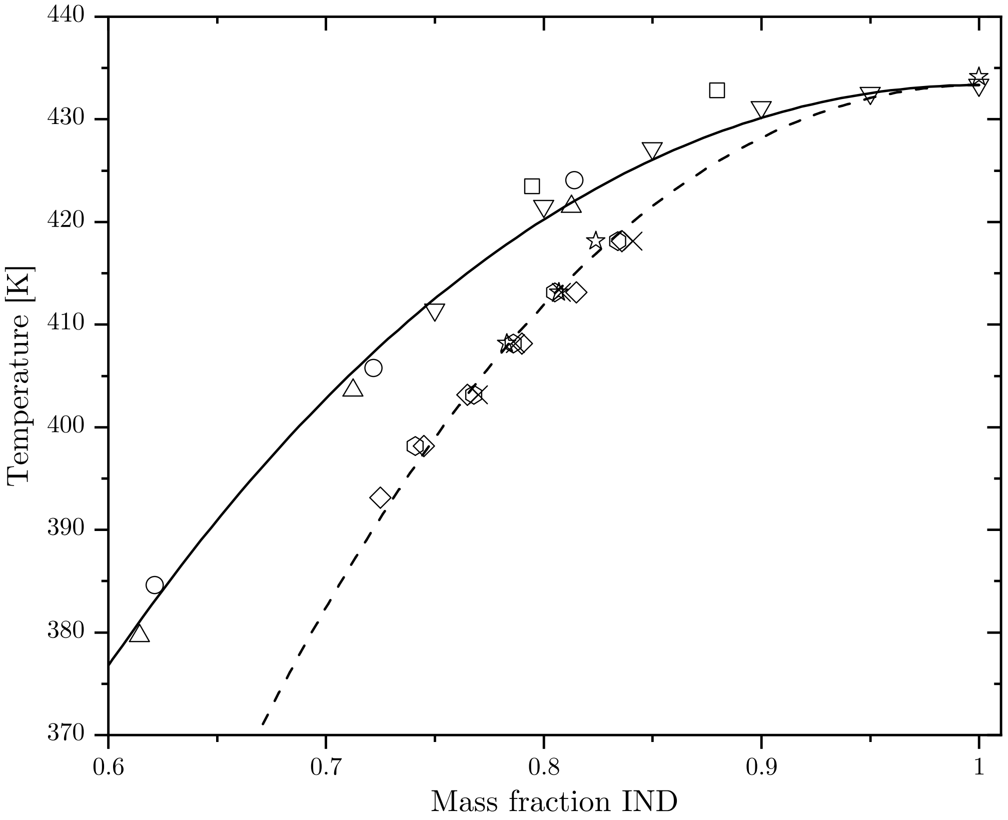

Figure 4.19: Experimental (□ $\bar{M}_{\mathrm{PVP}} = 25.7\,\mathrm{kg\,mol^{-1}}$ [60], ○ $\bar{M}_{\mathrm{PVP}} = 28 - 34\,\mathrm{kg\,mol^{-1}}$ [136], △ $\bar{M}_{\mathrm{PVP}} = 2.5\,\mathrm{kg\,mol^{-1}}$ [136], ▽ $\bar{M}_{\mathrm{PVP}} = 2.5\,\mathrm{kg\,mol^{-1}}$ [3] (◇ $\bar{M}_{\mathrm{PVP}} = 23\,\mathrm{kg\,mol^{-1}}$, ⬡ $\bar{M}_{\mathrm{PVP}} = 7 - 11\,\mathrm{kg\,mol^{-1}}$, × $\bar{M}_{\mathrm{PVP}} = 44 - 54\,\mathrm{kg\,mol^{-1}}$, ☆ $\bar{M}_{\mathrm{PVP}} = 1000 - 1500\,\mathrm{kg\,mol^{-1}}$) [44]) and calculated (—— SL set A , – – SL set B) SLE of IND-PVP at 1 bar. The calculations were carried out using the SL parameters listed in Table 4.1, the k_{ij} listed in Table 4.7 and the fusion properties listed in Table 4.2.

The experimental SLE data [3, 44, 60, 136] shown in Figure 4.19 is partially contradictory. On one hand there is the data from Sun et al. [136], Mathers et al. [3] and

Prudic et al. [60] which are in excellent agreement with each other and were all measured via DSC. The data from Sun et al. [136] was measured for the γ-polymorph of IND ($T_{0,i}^{SL}$ = 160 °C [136] and $\Delta_{\mathrm{SL}}h_{0,i}$ = 39.7 kJ mol^{-1} [231][2]). The data from Mathers et al. [3] and Prudic et al. [60] were also measured for the γ-polymorph of IND. Even though the polymorph measured was not explicitly stated by Prudic et al. [60], the fusion temperature 160.1 °C and fusion enthalpy 39.3 kJ mol^{-1} were both taken from Paus et al. [155], who performed the measurements using the γ-polymorph. The slight deviation among the data reported by Mathers et al. [3], Sun et al. [136] and Prudic et al. [60] can be ascribed to an inaccurate digitalization of the data from Figure 8b in Prudic et al. [60]. On the other hand, there is the data from Knopp et al. [44] measured for the γ-polymorph (confirmed via XRPD) of IND ($T_{0,i}^{\mathrm{SL}}$ = 161.0 ± 0.1 °C and $\Delta_{\mathrm{SL}}h_{0,i} \approx 40.57$ kJ mol^{-1}) [44] also via DSC. Since there is *a priori* no obvious explanation for the difference among the data [3, 44, 60, 136], the k_{ij} of the ASD IND-PVP was fitted twice using different SLE experimental data according to Table 4.7.

Regardless of the differences in the SLE experimental data [3, 44, 60, 136], the influence of the molar mass of PVP on the SLE is superfluous. For instance, Knopp et al. [44] used PVPs with molar masses differing 3 orders of magnitude and obtained very similar results for the SLE as shown in Figure 4.19. The same conclusion is obtained by comparing the data of Sun et al. [136] and Mathers et al. [3] who used PVPs with 1 order magnitude difference in the molar masses and both came to very similar results for the SLE as well as shown in Figure 4.19. Furthermore, Sun et al. [136] also measured the SLE IND-PVP using polymers with one order of magnitude difference in the molecular weights and reported no appreciable differences in the results obtained as shown in Figure 4.19.

Both binary interaction parameters of IND-PVP listed in Table 4.7 can now be used to predict the glass temperature of the ASD via the GET. The phase diagram including the prediction of the glass temperature as well as the SLE is shown in Figure 4.20. The experimental glassy density of IND used in the GT calculations listed in Table 4.7 was reported by Tong and Zografi [232] and is in agreement with other reported values [54, 234].

The experimental glass temperature reported by Sun et al. [136] shown in Figure 4.20 was measured via DSC as the onset temperature upon cooling at 10 K min^{-1}. The binary mixtures IND-PVP were prepared via cryomilling and were then annealed from 4 h to 10 h at a non-specified temperature prior to the DSC analysis [136]. Moreover, Prudic et al. [60] prepared the ASDs IND-PVP via spray drying using ethanol as solvent and nitrogen as drying agent. The glass temperature of the ASDs was measured via mDSC after a quenching step at a heating rate of 2 K min^{-1} with a modulation period of 60 s and an amplitude of 0.318 K [60]. Furthermore, Gong et al. [57] prepared the IND-PVP mixtures by coprecipitation using supercritical carbon dioxide. The glass temperature of the ASDs was measured via DSC from the first heating run at 10 K min^{-1} [57]. Additionally, Lopez et al. [43] prepared fibers of IND-PVP using the procedure described in their paper [43]. The glass temperature of the fibers containing different weight percentage of IND was measured via mDSC at 3 K min^{-1} and a modulation period of 60 s [43].

---

[2] In the original publication by Sun et al. [136] was stated that the fusion enthalpy was taken from Marsac et al. [233]. However, the correct reference may be Marsac et al. [231].

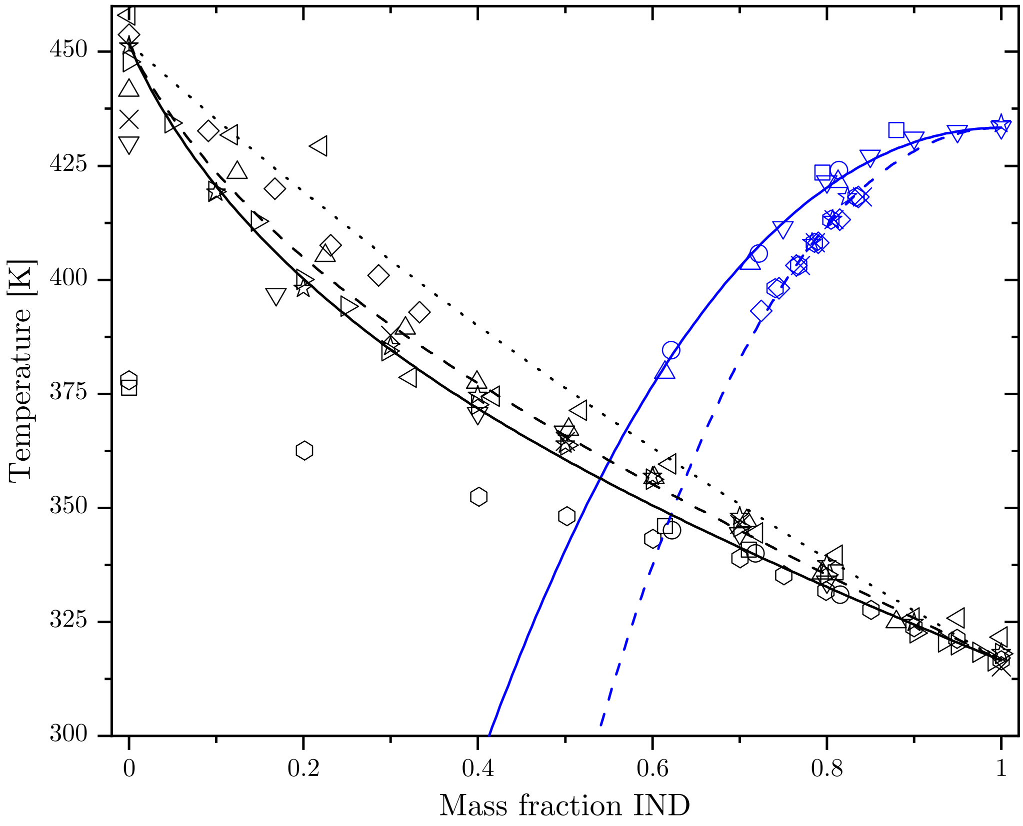

Figure 4.20: Experimental glass temperature ((□ $\bar{M}_{\text{PVP}} = 2-3\,\text{kg}\,\text{mol}^{-1}$, ○ $\bar{M}_{\text{PVP}} = 28-34\,\text{kg}\,\text{mol}^{-1}$) [136], △ $\bar{M}_{\text{PVP}} = 25.7\,\text{kg}\,\text{mol}^{-1}$ [60], ▽ $\bar{M}_{\text{PVP}} = 44\,\text{kg}\,\text{mol}^{-1}$ [57], ◇ $\bar{M}_{\text{PVP}} = 360\,\text{kg}\,\text{mol}^{-1}$ [43], ⬡ $\bar{M}_{\text{PVP}} = 2.5\,\text{kg}\,\text{mol}^{-1}$ [3], ◁ $\bar{M}_{\text{PVP}}$ not stated [54], ▷ $\bar{M}_{\text{PVP}}$ not stated [64], ☆ $\bar{M}_{\text{PVP}}$ not stated [56], × $\bar{M}_{\text{PVP}} = 50\,\text{kg}\,\text{mol}^{-1}$ [137], + [58]), experimental SLE (□ [60], (○, △) [136], ▽ [3], (◇, ⬡, ×, ☆) [44]), calculated glass temperature (— GET set A, – – GET set B, ··· GT) and calculated SLE (— SL set A, – – SL set B) of IND-PVP at 1 bar. The calculations with GET and SL were performed using the SL parameters listed in Table 4.1, the k_{ij} listed in Table 4.7, the k_p listed in Table 4.5 and the fusion properties listed in Table 4.2. The GT calculations were carried out using the experimental glass temperatures listed in Table 4.5 and the glassy densities listed in Table 4.7.

Mathers et al. [3] prepared the ASDs by weighing the desired amount of the pure components and ball milling them together. The glass temperature of the resulting ASD was measured via DSC as the midpoint of the glass transition event upon heating, however, no further details such as the heating rate used were reported [3]. Moreover, Chokshi et al. [137] measured the glass temperature IND-PVP shown in Figure 4.20 via DSC at a heating rate of $10\,\text{K}\,\text{min}^{-1}$, whereas the ASDs were prepared via hot-melt extrusion to be then cooled and milled prior to analysis. Finally, Lu and Zografi [64] and Crowley and Zografi [56] prepared the ASD IND-PVP by rotaevaporation from methanol as described in detail by Yoshioka et al. [54]. The glass temperature was then measured via DSC on all three studies [54, 56, 64] as the onset temperature on the second heating run using a heating rate of $20\,\text{K}\,\text{min}^{-1}$ [54, 56] and $10\,\text{K}\,\text{min}^{-1}$ [64].

The experimental glass temperature of IND-PVP at mass fractions of IND higher than 0.7 [3, 54, 56, 57, 60, 64, 136, 137] shown in Figure 4.20 are in excellent agreement with each other, even though the molecular weight of the PVP used differ in at least one order of magnitude [57, 136, 137]. The agreement worsens towards lower mass fractions of

IND and reaches a maximum at around 0.19, where the difference in the reported glass temperature [3, 43] amounts to over 100 K. Evidently, the PVP of low molar mass used by Mathers et al. [3] leads to a lower glass temperature of the ASD. On the other hand, the glass temperature of pure PVP reported by Sun et al. [136] and Mathers et al. [3] is substantially lower than the other values [43, 54, 56–58, 60, 64, 137] following the trend previously discussed and shown in Figure 4.8. Furthermore, the binary interaction parameter of the ASD IND-PVP has a higher influence on the calculated SLE than on the predicted glass temperature. For instance and according to Figure 4.20, the difference in the predicted glass temperature between sets A and B at $w_{\mathrm{IND}} \approx 0.6$ is lower than 10 K, whereas the difference in the calculated SLE temperature at the same mass fraction is higher than 25 K. Moreover, the GT calculation is in good agreement with the experimental glass temperature reported by Yoshioka et al. [54] and Lopez et al. [43], whereas the predictions achieved via the GET using set A and B are in better agreement with the other sources [56, 57, 60, 64, 136, 137].

According to the calculated phase diagram presented in Figure 4.20, the glass temperature of the ASD formed by IND and PVP is higher than the room temperature ≈ 300 K for all concentrations. According to the SLE calculations, the ASD should be stable against recrystallization at room temperature for mass fractions of IND lower than 0.4 (set A) or lower than ≈ 0.52 (set B). Chokshi et al. [137] performed a stability analysis against relaxation and recrystallization of the ASD at 40 °C and 75 % RH, however, the time period studied was only 3 months. They found out that even though the ASDs containing 70, 50 and 30 % weight of IND slightly relaxed, no recrystallization took place as confirmed via XRPD [137]. The maximal T_G depression of ≈ 5 K was evidenced by the ASD containing 30 % weight of IND [137]. These results [137] are in agreement with the GET predictions presented in Figure 4.20, as the predicted glass temperature of the ASD is higher than 40 °C for mass fractions of IND lower than 0.7. Furthermore, the maximal T_G depression reported by Chokshi et al. [137] is mostly due to the moisture absorbed by the ASD, as PVP is highly hygroscopic [93]. On the other hand, Matsumoto and Zografi [126] found out that the molecular dispersion of IND and PVP with 5 and 30 % weight PVP did not recrystallize whatsoever after dry storage at 30 °C over a period of 20 weeks. Finally, Yoshioka et al. [54] suggested that the crystallization inhibition of PVP over IND is not only caused by the time scale of the glass transition, but also by other factors regarding the chemical and steric interactions. This means that the stability of ASDs depends on the difference between the storage temperature and the glass transition of the formulation, and on the intermolecular interactions between the API and the polymer.

4.2.3 Naproxen + poly vinyl pyrrolidone

The experimental [59, 60] and calculated SLE of NAP-PVP is shown in Figure 4.21. Paudel et al. [59] measured the SLE experimental data of NAP-PVP shown in Figure 4.21 via mDSC at 2 K min^{-1} and an amplitude of 1 K every 40 s. Furthermore, Prudic et al. [60] also measured the SLE experimental data shown in Figure 4.21 via mDSC at 2 K min^{-1}, 5 K min^{-1} and 10 K min^{-1} with three different amplitudes and a constant 60 s period after applying a heating and successive quench cooling ramp to remove excess water in the ASDs. The equilibrium temperatures were measured by Prudic et al. [60] as the offset point of the dissolution peak on the thermographs, whereas the SLE points reported [60] and shown in Figure 4.21 are the extrapolation of the measured offset temperatures to zero heating rate [60].

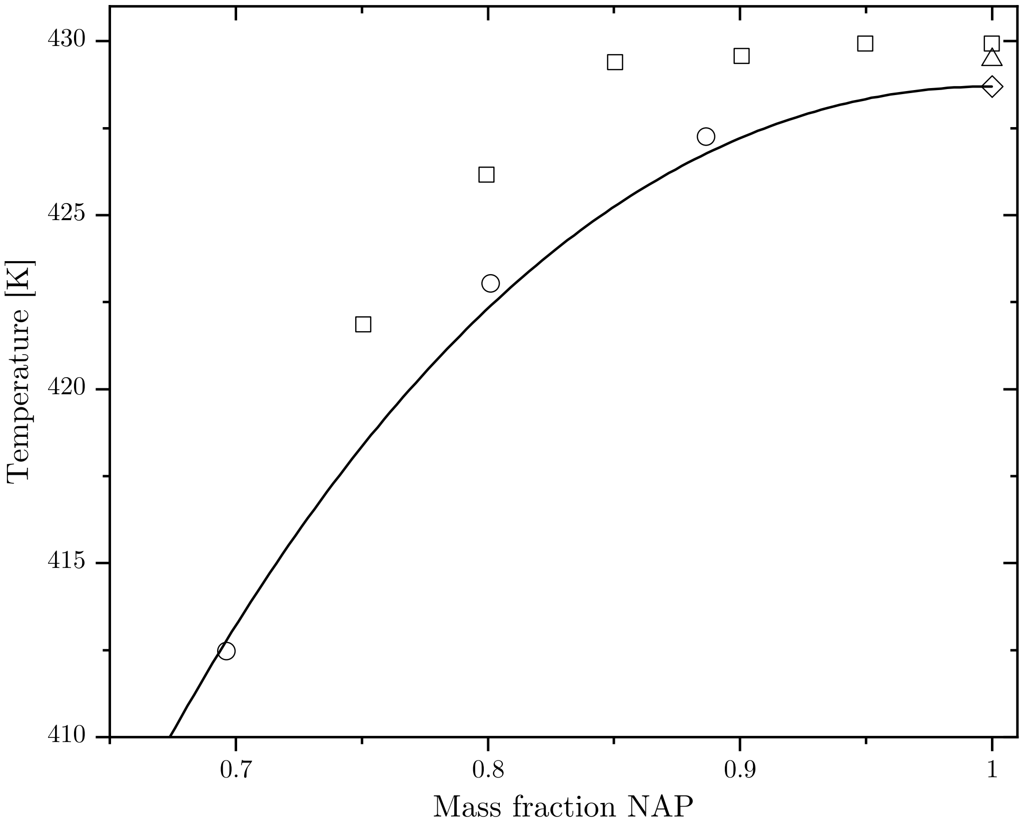

Figure 4.21: Experimental (□ [59], ○ [60], △ [155], ◇ [116]) and calculated (— SL) SLE of NAP-PVP at 1 bar. The calculations with SL were carried out using the SL parameters listed in Table 4.1, the k_{ij} listed in Table 4.7 and the fusion properties listed in Table 4.2. The experimental data from Paudel et al. [59] is shown only for comparison and was not used to fit the k_{ij}.

The experimental fusion temperatures of NAP [59, 116, 155] are in excellent agreement with each other and within experimental uncertainty. On the other hand, the experimental SLE data from Paudel et al. [59] exhibits a relative flat slope at mass fractions of NAP higher than 0.8. This behavior cannot be well described by the SL EOS with physically feasible values of the binary interaction parameter. Therefore, only the SLE data from Prudic et al. [60] was used to fit the k_{ij} of the ASD. At this point it is important to point out that the scale in Figure 4.21 comprises only 20 K and the measured SLE data [59, 60] are in excellent agreement with each other for the whole composition range studied.

The fitted binary interaction parameter was used to calculate the phase diagram of NAP-PVP shown in Figure 4.22. The glassy density of NAP used in the GT calculations is listed in Table 4.7.

The experimental glass temperatures of the ASD reported by Nair et al. [55] were measured via DSC at a heating rate of 10 K min^{-1}. The ASDs were prepared using the solvent casting method [55] with methanol and amorphous NAP was obtained after quenching the molten drug using dry ice [55]. Similarly, Paudel et al. [59] prepared the ASDs also using the solvent casting method with methanol as described in detail in their publication. The glass temperature of the films was measured via mDSC at a heating rate of 2 K min^{-1} with an amplitude of 1 K and a period of 40 s [59]. Finally, Prudic et al. [60] obtained the ASDs by spray drying from ethanol using nitrogen as drying agent. The glass temperatures of the ASD were measured via mDSC at a heating rate of 2 K min^{-1}, a period of 60 s and an amplitude of 0.318 K [60].

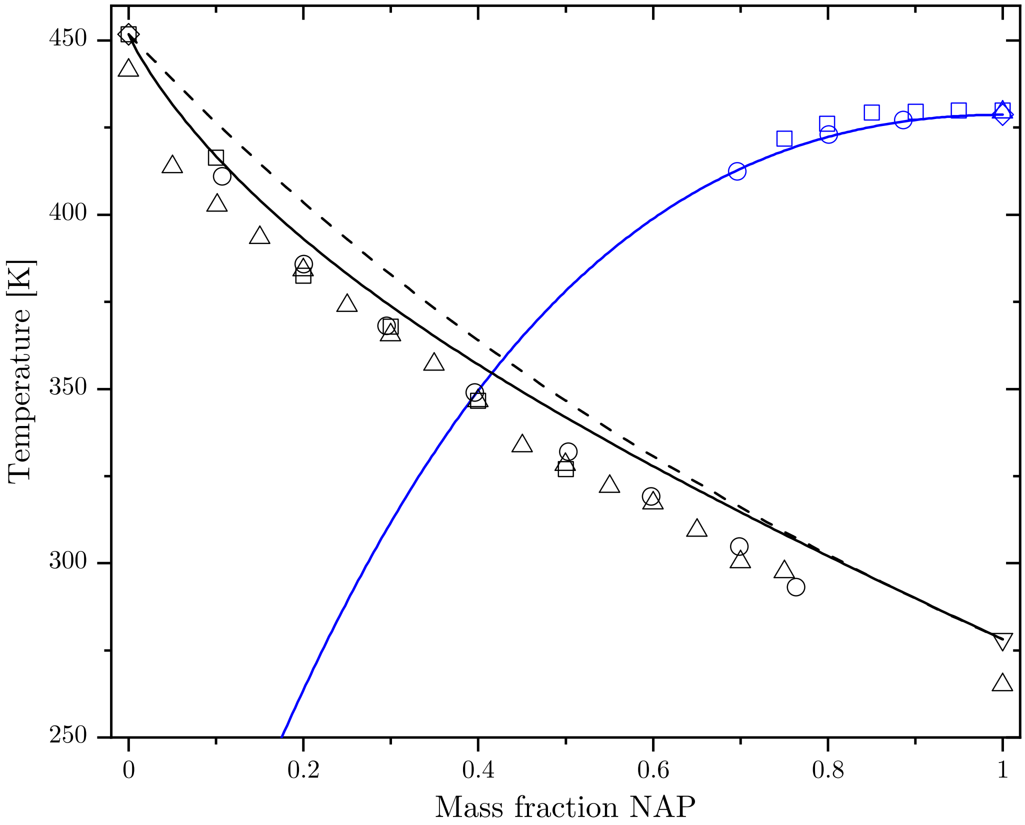

Figure 4.22: Experimental glass temperature (□ $\bar{M}_{\mathrm{PVP}}$ = 1300 kg mol^{-1} [55], ○ $\bar{M}_{\mathrm{PVP}}$ = 25 kg mol^{-1} [59], △ $\bar{M}_{\mathrm{PVP}}$ = 25.7 kg mol^{-1} [60], ▽ [4], ◇ [58]), experimental SLE (□ [59], ○ [60], △ [155], ◇ [116]), calculated glass temperature (— GET, – – GT) and calculated SLE (— SL) of NAP-PVP at 1 bar. The calculations with GET and SL were performed using the SL parameters listed in Table 4.1, the k_{ij} listed in Table 4.7, the k_p listed in Table 4.5 and the fusion properties listed in Table 4.2. The GT calculations were carried out using the experimental glass temperatures listed in Table 4.5 and the glassy densities listed in Table 4.7.

The experimental glass temperatures of NAP-PVP [55, 59, 60] shown in Figure 4.22 are in very good agreement with each other. There is only a slight deviation towards mass fractions on NAP lower than 0.1, however, the deviation can be ascribed to the different molecular weights of the PVPs used to prepare the ASDs. The glass temperature of pure PVP reported by Nair et al. [55] and digitalized from their Figure 2(d) is in excellent agreement with the value reported by Paudel et al. [58] and therefore with the trend previously discussed regarding Figure 4.8.

The predicted glass temperature via GET presented in Figure 4.22 is in good agreement with the experimental values [55, 59, 60]. The T_G prediction worsens towards higher mass fractions of NAP, however, the difference between the GET prediction and the experiment [55, 58, 60] does not exceed 15 K. Furthermore, the GET prediction is slightly better than the GT calculation at mass fractions of NAP lower than 0.6, additionally, both the GT calculation and the GET prediction are almost equal at higher mass fractions of NAP. Regarding the whole phase diagram shown in Figure 4.22, the glass temperature of the ASD does not reach the room temperature up until mass fractions of NAP higher than 0.7. However, the ASD is stable against recrystallization only up to mass fractions of NAP lower than ≈ 0.3, if the trend of the calculated SLE line should hold.

Consequently, an ASD of NAP-PVP with a mass fraction of 0.3 NAP should be stable against recrystallization and relaxation over the shelf life, if stored at dry conditions. Of course, a stability test over time is required before definitely assuring that the ASD will not relax to its equilibrium liquid state in a given period of time, since a thermodynamic analysis alone is not sufficient to resolve this inquiry unambiguously. Lehmkemper et al. [63] performed a stability analysis of the dry ASD at 25 °C and found out that NAP remained completely amorphous for at least 18 months in the formulation containing 40 % weight of NAP. For comparison, the formulation containing 50 % weight of NAP partially recrystallized after 12 months storage [63]. Furthermore, the SLE extrapolation at 300 K shown in Figure 4.22 is in agreement with the SLE extrapolation using the PC-SAFT EOS reported by Lehmkemper et al. [63]. In a similar study performed by the same group [62] was concluded that the ASD containing less than 60 % weight of NAP remained stable against recrystallization after storage at 25 °C for up to six months. On the other hand, ASDs containing 40 % weight NAP remained stable after storage at the same conditions for up to 18 months [62].

4.3 Influence of moisture

In order to test the influence of moisture on the glass temperature of ASDs, the binary interaction parameter of water-polymer and water-API mixtures needs to be fitted to experimental data. First, the selection of relevant experimental data on the water sorption in PVP [174] to fit the k_{ij} as well as the experimental [92, 93, 158, 160–162] and predicted glass temperature of PVP as a function of the absorbed moisture are discussed in section 4.3.1. Then, the experimental [140, 159, 179, 180] and calculated water sorption in IND such as its experimental [159] and predicted glass temperature as a function of the absorbed moisture are discussed in section 4.3.2. Finally, the experimental [56] and predicted water sorption in the IND-PVP such as the experimental [56] and predicted glass temperature of IND-PVP over the absorbed water are discussed in section 4.3.3. Furthermore, the prediction of the glass temperature of the ASD as a function of the relative humidity, storage temperature and ASD composition is also discussed in section 4.3.3. No further adjustable parameters were included in the model to improve the calculation of ternary systems, thus, all calculations presented in section 4.3.3 are also predictions. The binary interaction parameters of water mixtures containing PVP, IND and NAP, respectively, such as the specific glassy density and glass temperature of water are listed in Table 4.8. The selection of the experimental data used to fit the k_{ij} is described in detail in the following sections.

Table 4.8: Binary interaction parameters in equation (3.12) of water mixtures containing poly vinyl pyrrolidone, indomethacin and naproxen, respectively, and specific glassy density and glass temperature of water used in the GT equation (2.6).

Mixture	$k_{ij,0}$ [-]	$k_{ij,T} \cdot 10^3$ [K^{-1}]	Exp. data
PVP-water	1.3825	−0.352	[174]
IND-water	0.5818	1.24	[140, 159, 179, 180]
NAP-water	1.2398	−0.4275	[151]

Component	$\rho_{0,i}^{gl.}$ [$\mathrm{kg\,m^{-3}}$]	T_G [K]	k_p in equation (2.11)
water	997.05 [235]	136 [236]	0.66

4.3.1 Poly vinyl pyrrolidone + water

The binary interaction parameter of the mixture PVP-water was fitted to vapor sorption experimental data at 298.15, 308.15, 315.15 and 328.15 K reported by Sadeghi and Taghi Zafarani-Moattar [174]. A temperature-independent k_{ij} was fitted to each isotherm [174] and then a linear regression of the fitted values was performed which led to the k_{ij} in equation (3.12) listed in Table 4.8. The comparison between the experimental [97, 160, 161, 174, 237, 238] and calculated water sorption of PVP is shown in Figure 4.23. The water sorption experimental data reported by Sadeghi and Taghi Zafarani-Moattar [174] was selected to fit the k_{ij}, as it was measured at mass fractions of absorbed water above the T_G of PVP-water mixtures as can be deduced from Figure 4.24.

Sadeghi and Taghi Zafarani-Moattar [174] measured the water sorption in PVP of 10 $\mathrm{kg\,mol^{-1}}$ average molar mass isothermally at 298.15, 308.15, 318.15 and 328.15 K using the isopiestic method described in section 2.3.4.1. Furthermore, the experimental water sorption in glassy PVP [97, 160, 161, 237, 238] depicted in Figure 4.23 is shown only for comparison and was not used in fitting the binary interaction parameter, as it cannot be described by the SL EOS alone as discussed in section 2.2. On the other hand, the temperature dependence of the experimental water sorption isotherms above T_G [174] can be very well described by the SL EOS, even though the temperature-dependence is relatively low as seen in Figure 4.23. It must be pointed out that Sadeghi and Taghi Zafarani-Moattar [174] did not measure themselves the T_G of the pure PVP and its solutions with water. Nevertheless, the glass temperature of a PVP with molar mass equal to 10 $\mathrm{kg\,mol^{-1}}$, as used by Sadeghi and Taghi Zafarani-Moattar [174], is lower than 420 K according to Figure 4.8. Therefore, the absorbed humidity required to depress the T_G of PVP to values under the room temperature are even inferior than shown in Figure 4.24. One can thus assume with some degree of certainty that the PVP used in their experiments [174] was always above its T_G.

The experimental [92, 93, 158, 160–162] and predicted T_G of PVP as a function of the absorbed water is shown in Figure 4.24. The k_p (equation (2.11)) of water was fitted to the experimental T_G, both listed in Table 4.8. The GT calculations were performed using the T_G and the specific density of water listed in Table 4.8.

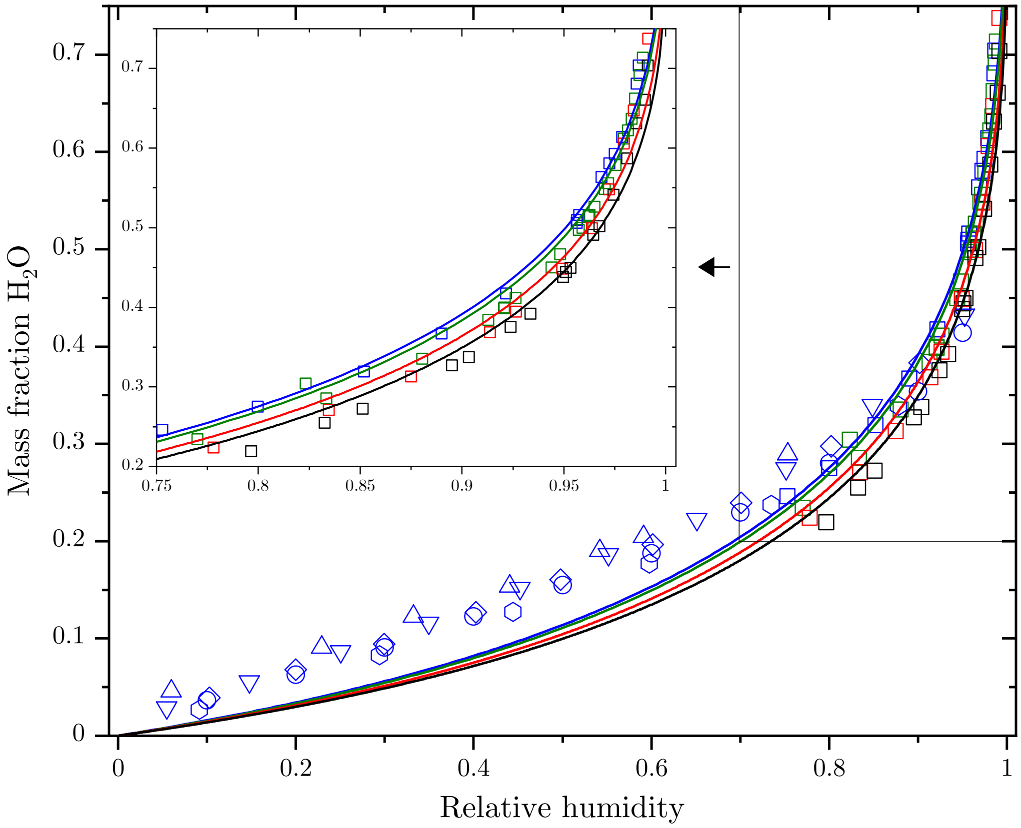

Figure 4.23: Experimental ((□, □, □, □) [174], ○ [160], △ [161], ▽ [237], ◇ [238], ⬡ [97]) and calculated (solid lines: SL) water absorption of PVP over the relative humidity at 1 bar. The colors represent data and calculations obtained isothermally at 298.15 K, 308.15 K, 318.15 K and 328.15 K, respectively. The inset shows only the experimental data [174] to which the temperature-dependent k_{ij} was fitted. All calculations were performed using the SL parameters of PVP and water listed in Tables 4.1 and 4.3, respectively, and the binary interaction parameter listed in Table 4.8.

The experimental water sorption reported by Oksanen and Zografi [93] shown in Figure 4.23 was measured using a PVP with a viscosity average molecular weight of 40 kg mol^{-1} using the desiccator method as described in section 2.3.4.2. The glass temperature of the equilibrated samples shown in Figure 4.24 were then measured in duplicate from the second heating run obtained via DSC using a heating rate of 20 K min^{-1} [93].

Buera et al. [158] investigated the influence of the PVP molecular weight on the water sorption isotherms. For consistency, only the results regarding the PVP with molar mass equal to 40 kg mol^{-1} [158] were considered. The water sorption was measured using the desiccator method as described in section 2.3.4.2. Then, the T_G of the equilibrated PVP samples shown in Figure 4.24 was measured as the onset temperature of the glass transition event from the second heating run obtained at 5 K min^{-1} [158].

Hancock and Zografi [92] also used the desiccator method described in section 2.3.4.2 to evaluate the vapor sorption of PVP and then measured the T_G of the equilibrated samples shown in Figure 4.24 via DSC at a heating rate of 20-40 K min^{-1}. The molecular weight of the PVP used was not explicitly stated by Hancock and Zografi [92], however, the glass temperature of dry PVP equal to 450 K [92] indicates that the molecular weight is higher than 100 kg mol^{-1} according to Figure 4.8.

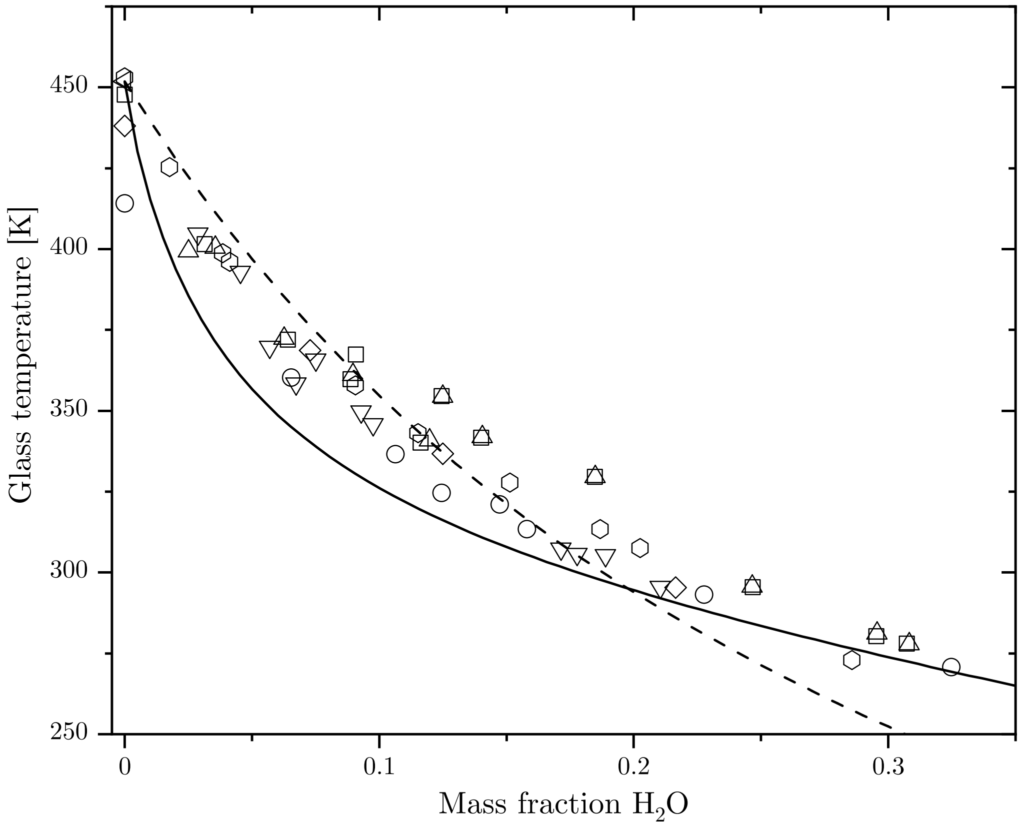

Figure 4.24: Experimental (□ [93], ○ [158], △ [92], ▽ [160], ◇ [162], ⬡ [161], ◁ [58]) and predicted (— GET, – – GT) glass temperature of water-PVP at 1 bar. The calculations were performed using the SL parameters of PVP and water listed in Tables 4.1 and 4.3, respectively, and the k_p listed in Table 4.5. The k_p, specific density and glass temperature of water used in the GET and GT calculations are listed in Table 4.8.

The moisture content of equilibrated PVP-water samples at different relative humidities was obtained by Fitzpatrick et al. [160] by thermogravimetric analysis by heating from 5 °C to 200 °C at 5 °C min^{-1} under a nitrogen purge. The experimental glass temperature of the equilibrated PVP-water samples shown in Figure 4.24 was measured via mDSC using a heating rate of 2 K min^{-1}, a modulation amplitude of 2 °C and a period of 1 min [160]. Neither the molecular weight nor the T_G of dry PVP were explicitly stated [160]. Saklatvala et al. [162] used a similar method as Fitzpatrick et al. [160] to measure the glass temperature shown in Figure 4.24.

Hasegawa et al. [161] measured the water content of equilibrated PVPs previously exposed to different relative humidities at constant temperature via Karl-Fischer titration. The T_G of the equilibrated PVP samples shown in Figure 4.24 was then measured as the midpoint of the glass transition event from the second heating runs obtained via DSC using an unspecified heating rate [161]. The molecular weight of the PVP used was also not explicitly stated [161].

The experimental [92, 93, 158, 160–162] and via GET predicted T_G of PVP shown in Figure 4.24 are in excellent agreement with each other. For instance, the GET calculation correctly predicts a steeper slope of T_G over the absorbed water, and therefore a higher plasticization, at mass fractions of water lower than 0.1 as also evidenced by the experimental data [92, 93, 158, 160–162]. Furthermore, the GET prediction correctly correlates the experimental data [92, 93, 158, 161] showing a flattening slope towards mass fractions of water higher than 0.2, which the GT prediction does not correlate well. Even though the GET prediction slightly overestimates the plasticization at lower mass fractions of water compared to the GT prediction, the agreement with the experimental T_G [92, 93, 158, 161] is better than the GT prediction at higher water mass fractions. It must be reiterated that the GET calculation was not fitted to the experimental data [92, 93, 158, 160–162]. Therefore, it can be concluded that the model presented in this work is suitable for predicting the plasticization of PVP over the whole relative humidity range without incurring in a greater error than the GT equation. On the other hand, the vapor uptake of glassy PVP requires an expansion of the SL EOS as briefly explained in section 2.2, however, the moisture sorption in the rubbery state above T_G can be also calculated with the present model without major deviation from the experimental data [174].

4.3.2 Indomethacin + water

The binary interaction parameter according to equation (3.12) of IND-water was fitted to experimental vapor sorption data [140, 159, 179, 180] as shown in Figure 4.25 and is listed in Table 4.8. The experimental water sorption in amorphous IND reported by Andronis et al. [159] shown Figure 4.25 was measured using a dynamic gravimetric method as described in section 2.3.4.3. Furthermore, the glass temperature of the equilibrated samples shown in Figure 4.26 was measured by Andronis et al. [159] via DSC at a heating rate of 1 K min^{-1}.

Dawson et al. [179] measured the water uptake of amorphous IND disks using an automated moisture sorption apparatus as described in section 2.3.4.3. The conditions at which equilibrium was assumed were different depending on the relative humidity range as explained in detail by Dawson et al. [179]. The experimental vapor sorption of IND reported by Dawson et al. [179] and shown in Figure 4.26 corresponds to the first cycle of the ordinary glass as shown in their Figure 2.

Rumondor et al. [140] measured the vapor sorption of IND shown in Figure 4.25 also using a dynamic gravimetric method as briefly explained in section 2.3.4.3. The amorphous IND was left to equilibrate at each relative humidity for about 600 min [140].

Borrmann et al. [180] measured the moisture sorption of IND shown in Figure 4.25 using a dynamic vapor sorption method as described in section 2.3.4.3. Equilibrium was assumed to be achieved after 180 min for RH lower than 0.6 and after 120 min for higher values [180].

As for PVP-water, the binary interaction parameter of IND-water should be fitted to experimental vapor sorption data above the glass temperature of IND. However, as the vapor sorption of IND is substantially lower than in PVP according to Figures 4.23 and 4.25, the effect of fitting to all experimental data [140, 159, 179, 180] or only to the points above the T_G should be negligible. This hypothesis was actually tested and the k_{ij} was fitted to only the points above the dashed lines in Figure 4.25 at the corresponding temperatures.

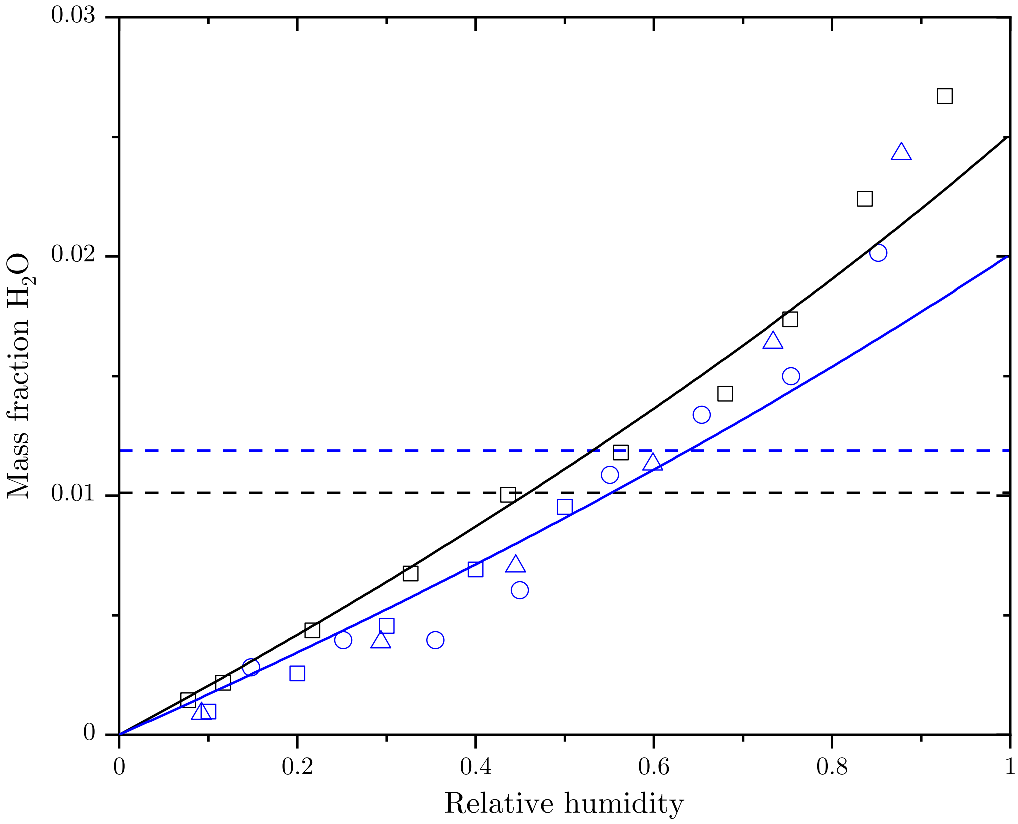

Figure 4.25: Experimental (□ [159] at 303.15 K, (□ [179], ○ [140], △ [180]) at 298.15 K) and calculated (— SL at 303 K, — SL at 298.15 K) water absorption of IND over the relative humidity at 1 bar. The lines (– –, – –) approximately denote the required absorbed water mass fraction to depress the T_G of IND to 303.15 K and 298.15 K, respectively, according to Figure 4.26. All calculations were performed using the SL parameters of IND and water listed in Tables 4.1 and 4.3, respectively, and the binary interaction parameter listed in Table 4.8.

The predicted glass temperature almost did not change compared to the prediction calculated using the k_{ij} fitted to all reported points shown in Figure 4.25. Therefore, the temperature-dependent k_{ij} initially fitted to all experimental data [140, 159, 179, 180] was further used to not arbitrarily exclude points from the measured data sets. The ordinate values of the dashed lines shown in Figure 4.25 were read from the next higher point in the x-axis relative to the isotherms shown in Figure 4.26.

The calculated water sorption in IND shown in Figure 4.25 correlates well the experimental data [140, 159, 179, 180], even though the isotherms do not possess the proper curvature towards high relative humidities. Furthermore, the calculated isotherms exhibit a boundary value of the absorbed water mass fraction different than unity at 100 % RH. This implies that there is a vapor-liquid-liquid equilibrium at higher mass fraction of absorbed water. This behavior was also obtained in calculations of the vapor sorption in IND using the PC-SAFT EOS as reported by Borrmann et al. [180]. Of course, water and IND cannot coexist as liquids at 1 bar and room temperature, given that the fusion temperature of IND is higher than the boiling temperature of water at atmospheric pressure. Moreover, the crystalline solubility (SLE) of IND in water is in the order of 9×10^{-7} weight fraction at room temperature [153, 157, 239] and cannot be well described using the binary interaction parameter of IND-water previously mentioned. However, the water sorption in IND should be substantially more important than the location of the SLE curve. Therefore, the fitted temperature-dependent k_{ij} was further used to predict the glass temperature of IND as a function of the absorbed moisture as shown in Figure 4.26.

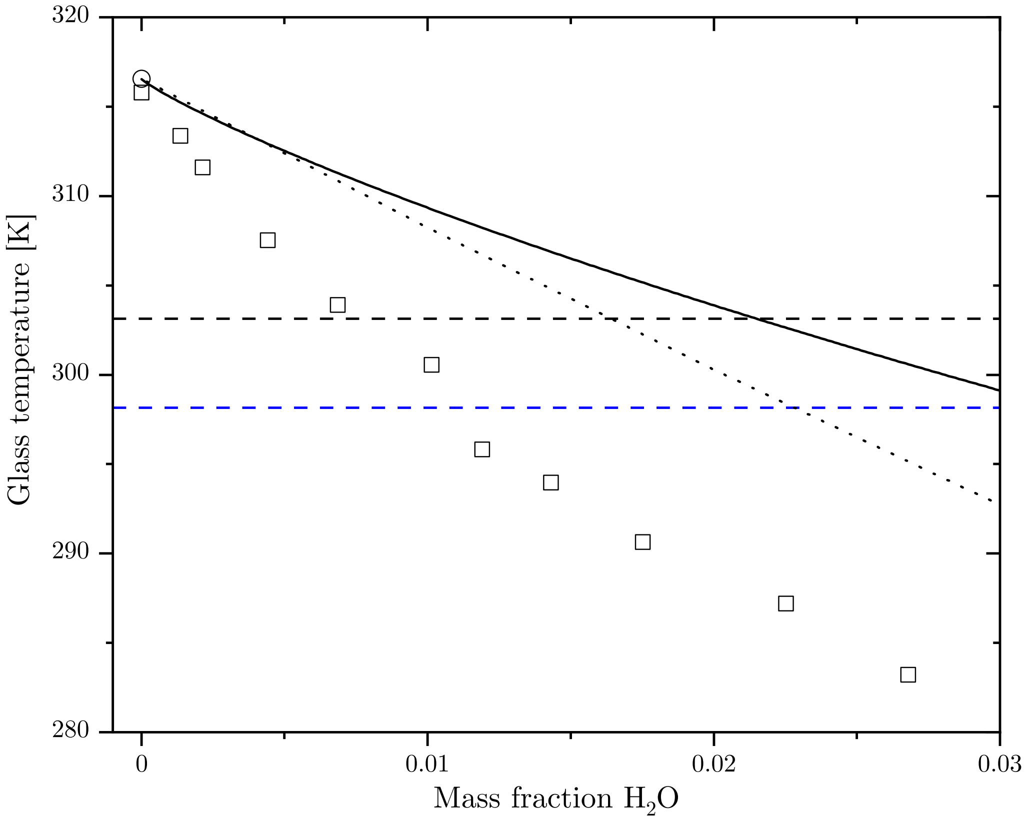

Figure 4.26: Experimental (□ [159], ○ [3]) and predicted (— GET, ··· GT) glass temperature of IND-water at 1 bar. The lines (– –, – –) denote isotherms at 303.15 K and 298.15 K, respectively. The calculations were performed using the SL parameters of IND and water listed in Tables 4.1 and 4.3, respectively, and the k_p listed in Table 4.5. The k_p, specific density and glass temperature of water used in the GET and GT calculations such as the k_{ij} are listed in Table 4.8.

The predicted glass temperature of IND-water shown in Figure 4.26 underestimates the plasticization of IND compared to the experimental T_G [159]. Both the GET prediction and the experimental glass temperature [159] exhibit an almost linear decrease with the absorbed water mass fraction. The GT calculation has a similar slope at lower mass fractions and is in agreement with the GET prediction, however, the GT calculation is closer to the experimental T_G [159] at higher mass fractions. Nonetheless, both the GET prediction and the GT calculation overestimate the experimentally measured T_G [159] in over 10 K at water mass fractions near 0.3. The reason behind the deviation is still unclear, however, association may play a key role regarding the temperature-independent k_{ij} obtained for instance by Borrmann et al. [180] using the PC-SAFT EOS. As the SL EOS used in this work does not account for association between the components, the fitted binary interaction parameter may account both for the deviation from the geometric mean included in the mixing rule and association leading to a poor description of T_G, whereas the PC-SAFT EOS can account separately for both effects and may achieve a better prediction. Of course, this is only an initial hypothesis whose validation needs to be further considered as it is outside the scope of this work.

4.3.3 Indomethacin + poly vinyl pyrrolidone + water

All binary interaction parameters were estimated and the ternary system consisting of IND-PVP-water can now be investigated. For this purpose, the experimental [56, 98, 140, 142] and predicted isothermal water sorption in the ASD IND-PVP at atmospheric pressure is shown in Figure 4.27.

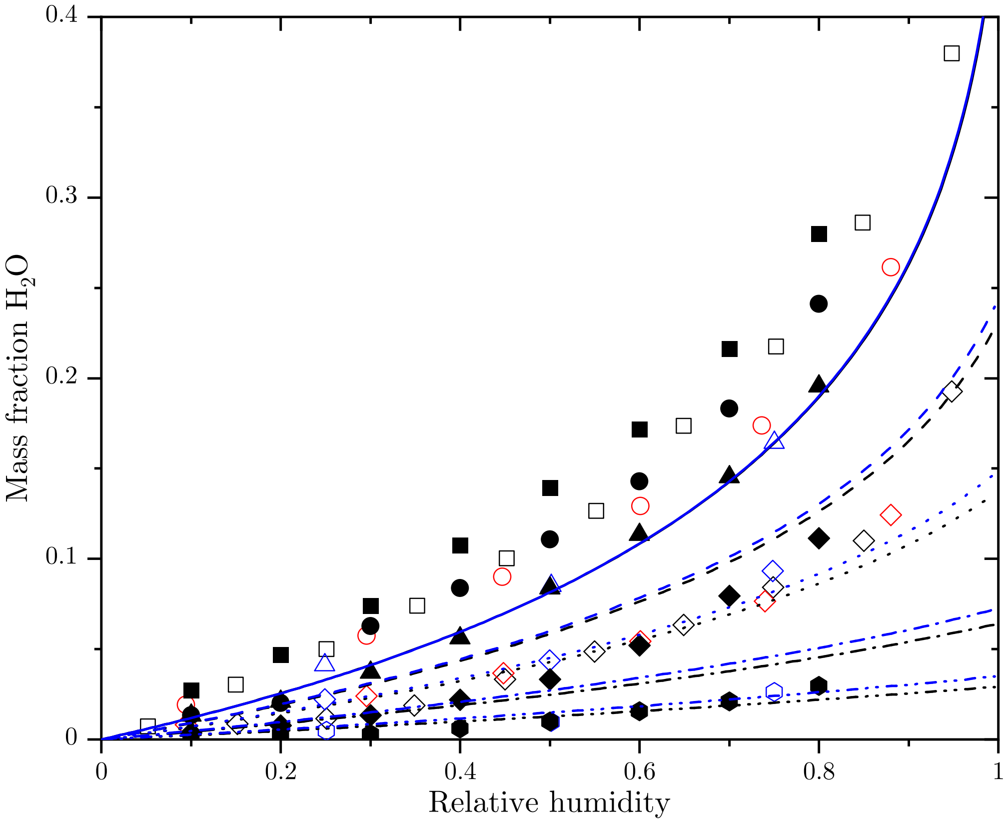

Figure 4.27: Experimental (squares: 10 % IND, circles: 20 % IND, triangles: 30 % IND, diamonds: 50 % IND, hexagons: 80 % IND, filled symbols were measured at 303 K [56] and open symbols at 298.15 K by black [140], blue [142] and red [98]) and predicted (— 10 % IND, – – 20 % IND, ··· 30 % IND, –·– 50 % IND, –·· 80 % IND, whereas black lines denote SL calculations at 303 K and blue lines at 298.15 K) water absorption in IND-PVP over the relative humidity at 1 bar. The percentages denote mass fractions of dry ASDs. All calculations were performed using the SL parameters of IND and PVP listed in Table 4.1, the SL parameters of water listed in Table 4.3 and the binary interaction parameters listed in Tables 4.7 and 4.8.
All experimental data shown in this figure was digitalized from the respective publications due to lack of written values, thus, any conclusions drawn from their comparison should be critically challenged.

Crowley and Zografi [56] measured the vapor uptake of IND-PVP shown in Figure 4.27 gravimetrically using an automated system as described in section 2.3.4.3. The IND-PVP dispersions were prepared by rotaevaporation from methanol with a further vacuum drying step up to 48 h for samples containing high concentrations of PVP [56]. The molecular weight of the PVP used was not explicitly stated [56]. The absence of crystals was confirmed via XRPD in all dispersions prepared [56]. All samples were stored in desiccators containing P_2O_5 at 277 K for the whole duration of the study and no crystallization was evidenced in any prepared dispersion stored at these conditions over a period of six months [56]. Moreover, the glass temperature of the equilibrated samples was measured via DSC at a heating rate of 20 K min^{-1} using nitrogen as purge gas after performing a first run to remove the thermal history of the samples [56]. The experimental data concerning the T_G of the ASD as a function of the absorbed water are shown in Figure 4.28.

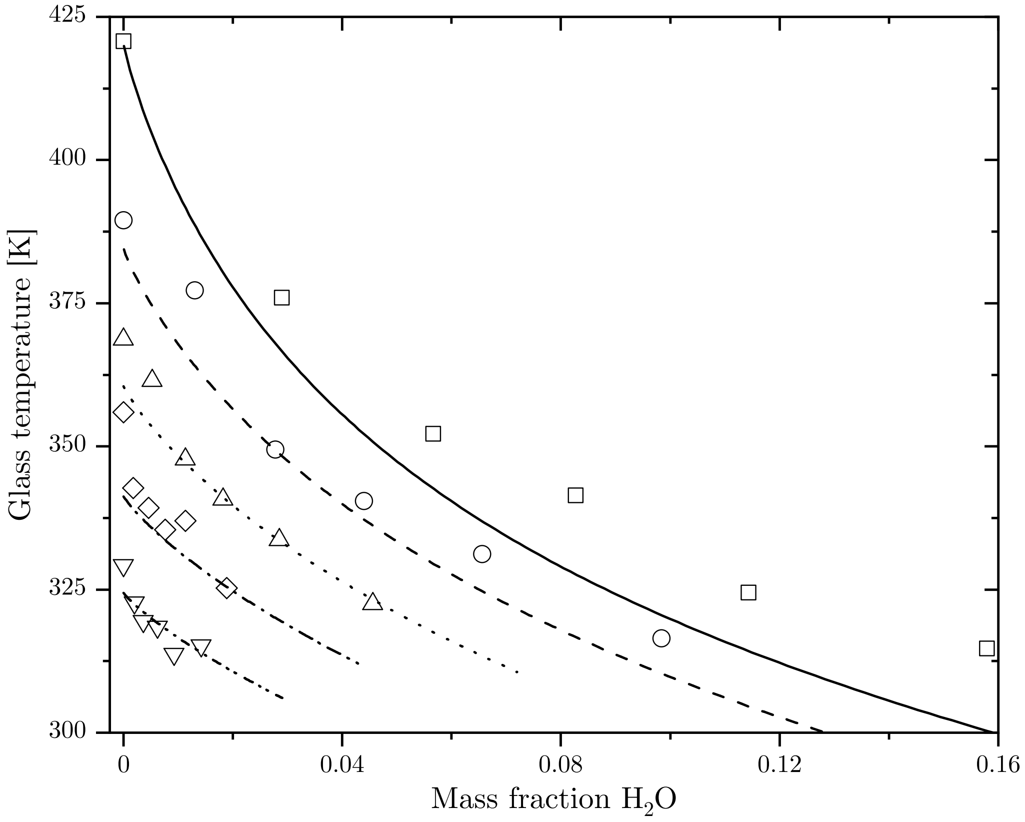

Figure 4.28: Experimental (□ 10 % IND, ○ 30 % IND, △ 50 % IND, ◇ 70 % IND, ▽ 90 % IND) [56] and predicted (—— GET 10 % IND, – – GET 30 % IND, ··· GET 50 % IND, – · – GET 70 % IND, – ·· GET 90 % IND) glass temperature of humid IND-PVP stored at 303 K and 1 bar. The percentages denote mass fractions of dry ASDs. All calculations were performed using the SL parameters of IND and PVP listed in Table 4.1, the SL parameters of water listed in Table 4.3, the k_p of IND and PVP listed in Table 4.5, the k_p of water listed in Table 4.8 and the binary interaction parameters listed in Tables 4.7 and 4.8.

Rumondor et al. [140] prepared the IND-PVP dispersions used to measure the vapor sorption data shown in Figure 4.27 by rotaevaporation from ethanol after drying the polymer for at least one week over P_2O_5, whereas the molecular weight of the PVP used was not explicitly stated. The resulting dispersions were placed under vacuum for at least 12 h and were then heated above the melting temperature of IND to ensure that no crystals remained in the samples [140]. Thereafter, the samples were cooled to room temperature and ground in a mortar [140]. The vapor uptake of the prepared dispersions was measured using a symmetrical gravimetric analyzer as described in section 2.3.4.3 at 298.15 K [140]. The samples were exposed to RH values from 5 % to 95 % in steps of 10 %, whereas equilibrium was assumed to be reached after 1000 min [140].

Prudic et al. [142] prepared the ASDs of IND-PVP used to measure the vapor uptake shown in Figure 4.27 via spray drying using ethanol as solvent, whereas the PVP used had a molecular weight of 25.7 kg mol^{-1}. After the preparation step, the samples were stored in a vacuum oven at 25 °C for at least one day to remove any remaining solvent and moisture [142]. The moisture sorption of the prepared ASDs was measured at 25 °C by a dynamic gravimetric method as described in section 2.3.4.3 [142]. Equilibrium was assumed to be reached after one to two days after exposing the samples to RH values of 25 %, 50 % and 75 % [142].

Borrmann et al. [98] prepared IND-PVP films used to measure the vapor uptake data shown in Figure 4.27 using a spin-coating technique described in detail elsewhere [97], whereas the molecular weight of the PVP used was 25.7 kg mol^{-1}. Prior to water sorption measurements, the films were dried in the measuring cell at a RH of 1×10^{-5} for at least 12 h [98]. Then, the vapor sorption was measured at 298.15 K and RH values between 0 and 0.9 using a dynamic vapor sorption device as described in section 2.3.4.3, whereas the crystallinity degree of the equilibrated films was tested via XRPD and no presence of crystals within the detection limits of the device were found [98].

The experimental vapor sorption data in the ASD containing 50 % IND [56, 98, 140, 142] shown in Figure 4.27 are in excellent agreement with each other bearing in mind that all points were digitalized from their respective sources. Furthermore, the temperature dependence of the experimental water sorption [56, 98, 140, 142] becomes almost negligible at mass fractions of IND in the dry ASD higher than 0.5, although the error made in the digitalization of the experimental data may have played a role on the observed trend. Regardless, the predicted temperature dependence is relatively low for all dry ASD compositions as can be deduced from Figure 4.27 by comparing the same type of lines with different colors. On the other hand, the experimental water sorption data at mass fractions of IND in the dry ASD lower than 50 % [56, 98, 140, 142] exhibit a weak temperature-dependence, whereas the higher the temperature the higher the absorbed vapor at constant RH. Overall, the predicted water sorption in the ASD shown in Figure 4.27 is underestimated for all IND mass fractions, even though the general qualitative trend is correctly predicted. As was the case for the predicted water sorption of pure IND shown in Figure 4.25, the predicted mass fraction of absorbed water in the ASD at 100 % RH shown in Figure 4.27 is different than unity, which indicates that a vapor-liquid-liquid equilibrium will form at higher mass fractions of absorbed water as also predicted using the PC-SAFT EOS [98]. Furthermore, the agreement between the experimental [56, 98, 140, 142] and the predicted water sorption in the ASD shown in Figure 4.27 becomes better with higher mass fractions of IND in the dry ASD. This last described behavior can be explained baring in mind that PVP absorbs almost ten times more water than IND at the same RH as can be seen by comparing Figures 4.23 and 4.25. Therefore, the poor description of the experimental water sorption in glassy PVP [97, 160, 161, 237, 238] achieved with the SL EOS as shown in Figure 4.23 is transferred onto the ternary system. Nevertheless, the water sorption in ASDs containing high concentration of IND can be still be well described as shown by the (− · ·)-lines in Figure 4.27. At this point it is important to stress out that both PVP and IND may have been plasticized below their respective glass temperatures alongside one or several isotherms as can be deduced from the trend of the experimental T_G of the ASD over the absorbed vapor as shown in Figure 4.28. Unfortunately, the experimental T_G of the ASD shown in Figure 4.28 is higher than both isotherms presented in Figure 4.27 which makes an estimation of the glass transition at a fixed value of the water sorption unfeasible without incurring in extrapolations of the experimental T_G of the ASD [56].

The agreement between the experimental [56] and predicted T_G of the ASD shown in Figure 4.28 is remarkably good bearing in mind that no further adjustable parameter was fitted to ternary data. This result implies that the correct description of the water sorption in the glassy state is not imperatively required to correctly predict the glass temperature of the ASD over the absorbed water vapor. Of course, the correct description of the water sorption in the glassy state is necessary to perform calculations on the stability of the ASD and should be corrected by implementing modifications as carried out by for instance Borrmann et al. [97] and Borrmann et al. [98]. Nonetheless, the model presented in this work has proved to be a powerful tool in predicting the phase behavior of the humid ASD IND-PVP.

Additionally, the phase diagram of the humid ASD IND-PVP as a function of the relative humidity is presented in Figure 4.29.

The experimental T_G shown in Figure 4.29 reported by Crowley and Zografi [56] is the same as in Figure 4.28. However, the glass temperature plotted over the dry ASD composition delivers new insights regarding the phase behavior of the ternary system. For instance, the experimental T_G [56] exhibits a maximum over the IND mass fraction in the dry ASD at constant RH. Thus, there must be an optimal drug load to achieve the maximal possible stability (lowest plasticization), given that the storage conditions (RH and temperature) are known. Close examination of the experimental T_G [56] at $\varphi = 0.1$ shown in Figure 4.29 indicates that the ASD with 30 % weight IND has a higher glass temperature than the ASD with 10 % weight drug load. This behavior means that there is a dry ASD composition for which the plasticization at constant RH is lower than in both the pure API and PVP. Such behavior was already reported for instance by Prudic et al. [142] for the ASDs composed of IND and NAP in PVP and poly vinyl pyrrolidone vinyl acetate (PVP-VA) as predicted using the GT equation. Although the predicted T_G via GET underestimates the plasticization of the ASD at RH values higher than 20 %, it is in better agreement with the experimental data [56] than the GT prediction.

An explanation of the maximum in the T_G as a function of the ASD composition at constant RH was given for instance by Prudic et al. [142]. According to Figure 4.27, the water sorption and therefore the plasticization of the ASD decreases by increasing the IND mass fraction in the dry ASD. Thus, the strong plasticized T_G of pure PVP on the left side of the phase diagram shown in Figure 4.29 must increase with the IND composition to then decrease and reach the value of the plasticized pure drug at the right hand side of the phase diagram [142].

Prudic et al. [142] also investigated the stability of humid IND-PVP ASDs via XRPD after four weeks storage at 25 °C. It was found that the humid ASD containing 30 % weight IND on a water-free basis did not recrystallize, however, the ASDs containing 50 % and 80 % weight IND on a water-free basis did so [142] which is in agreement with the predicted SLVE shown in Figure 4.29.

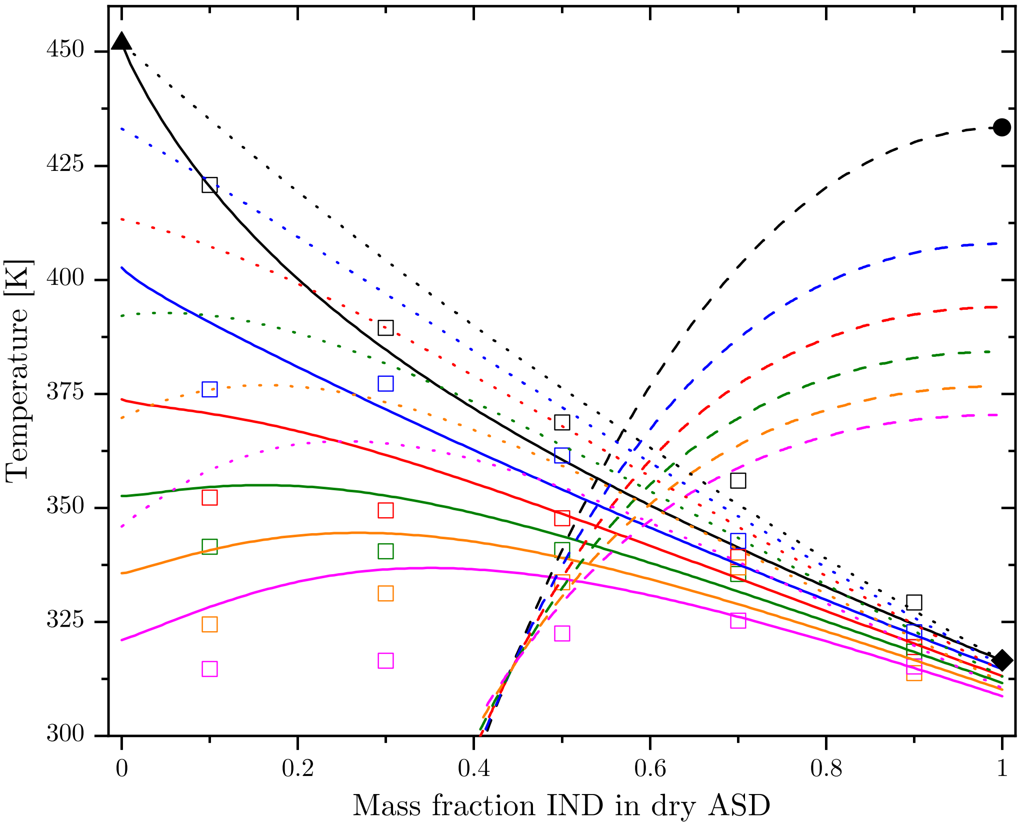

Figure 4.29: Experimental (open squares [56] measured at 303 K, ▲ [58], (●, ◆) [3]) and calculated (solid lines: T_G via GET, dotted lines: T_G via GT, dashed lines: SLVE via SL) phase diagram of humid IND-PVP at 1 bar. The colors represent 0 % RH, 10 % RH, 20 % RH, 30 % RH, 40 % RH and 50 % RH. The GET and SL calculations were performed using the SL parameters of IND and PVP listed in Table 4.1, the SL parameters of water listed in Table 4.3, the k_p of IND and PVP listed in Table 4.5, the k_p of water listed in Table 4.8 and the binary interaction parameters listed in Tables 4.7 and 4.8. The GT calculations were carried out using the properties of IND and PVP listed in Table 4.7, the properties of water listed in Table 4.8 and the T_G of IND and PVP listed in Table 4.5.

On the other hand, the influence of the absorbed moisture on the SLE predicted via SL is considerable and stronger towards higher IND mass fractions than predicted by for instance the PC-SAFT EOS [142]. Unfortunately and to the best of my knowledge, no experimental data on the ternary SLVE of IND-PVP-water is available in the literature for comparison. At this point it must be pointed out that the glass temperature of the humid ASD shown in Figure 4.29 was calculated regardless of the position of the SLVE curve. In other words, the T_G lines encapsulated by the SLVE curves at the corresponding RH were calculated using the predicted absorbed water in the ASD without considering the SLVE. The justification relies on the fact that Crowley and Zografi [56] reported no presence of crystals at any RH and ASD composition as measured via XRPD after four weeks storage at 303 K. Thus, even though the IND in the humid ASD must eventually recrystallize, it does so at a very slow rate as the ASD is still kinetically hindered. However, Prudic et al. [142] did measure recrystallization of IND as previously mentioned. Furthermore, the strong plasticization effect of small amounts of absorbed water predicted by the model was already reported for instance by Crowley and Zografi [56] and Prudic et al. [142]. This last behavior is at best seen by comparing the solid lines at RH values of 0 % and 10 % in Figure 4.29 at the left side of the phase diagram. The difference in the predicted T_G of pure PVP is clearly higher than the difference at RH values of 40 % and 50 %, even though the step is 10 % RH in both cases.

The phase diagram and glass temperature can be also depicted using a ternary diagram whose height denotes the temperature, as shown in Figure 4.30.

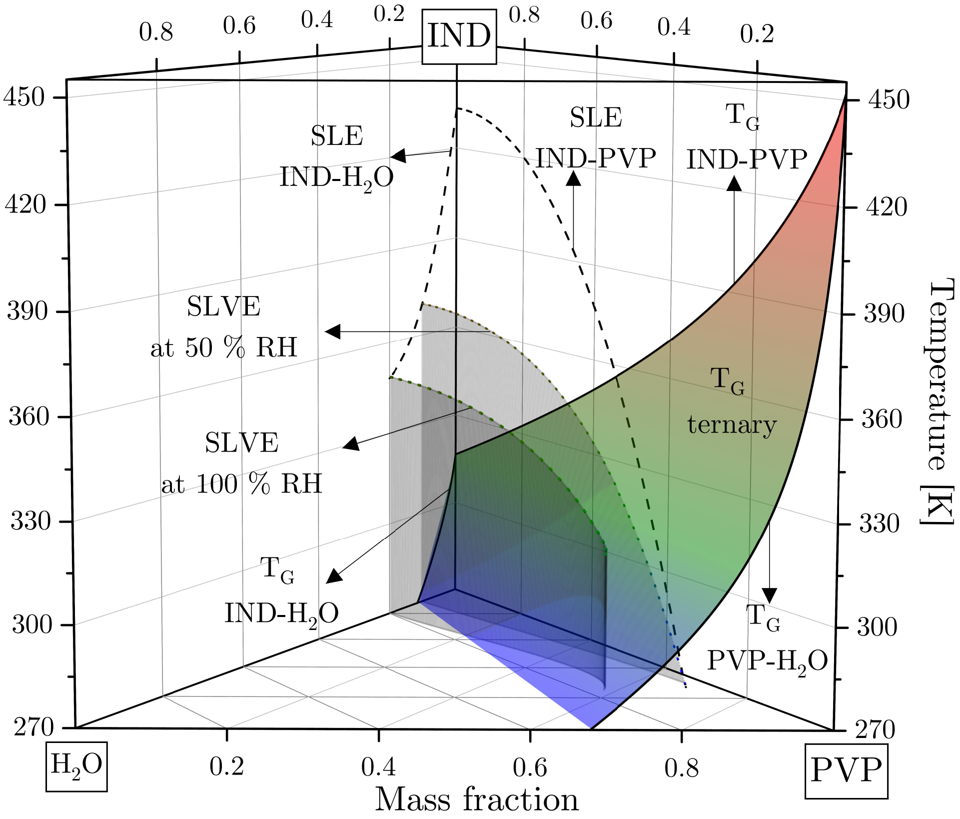

Figure 4.30: Predicted (— T_G prediction of corresponding binary subsystem via GET, – – SL calculation of corresponding binary SLEs, ··· SLVE prediction of ternary system via SL, colored surface: T_G prediction of ternary system, whereas gray surfaces denote the projection of the ternary SLVE lines on the composition plane at 50 % and 100 % RH) phase diagram and glass temperature of IND-PVP-water at 1 bar. All calculations were performed using the SL parameters of IND and PVP listed in Table 4.1, the SL parameters of water listed in Table 4.3, the fusion properties of IND listed in Table 4.2, the k_p of IND and PVP listed in Table 4.5, the k_p of water listed in Table 4.8 and the binary interaction parameters listed in Tables 4.7 and 4.8.

Given that the formulation is stored at room temperature, the further analysis is limited to the horizontal plane at 300 K in Figure 4.30. The predicted ternary T_G is above the storage temperature for water mass fractions lower than ≈ 0.2, whereas the formulation is stable against recrystallization at both 50 % and 100 % RH for mass fractions of IND lower than 30 %. Following the prediction shown in Figure 4.30, any formulation stored at room temperature containing 40 % weight of IND will eventually recrystallize, even if stored at dry conditions. Increasing the RH leads to an even larger recrystallization region, as is expected. On the other hand, decreasing the storage temperature to approximately 10 °C leads to a formulation stable against relaxation into the metastable liquid, however, the recrystallization region becomes also larger.

Consequently, choosing the most suitable drug load in the formulation is to be taken with care, as the stability of the humid ASD strongly depends on the RH and storage temperature which can have opposite effects on the recrystallization and relaxation processes. Moreover, the predicted SLVE also shows that the absorbed water mass fraction is always lower than 20 %, no matter the RH and storage temperature. At maximal RH, the glass temperature of the formulation is lower than 270 K only at drug loads higher than 80 %. However, regarding the results shown in Figure 4.26, the T_G line of IND-water should have a higher slope than shown in Figure 4.30. Nonetheless, the model presented in this work proofed to be a powerful tool in the prediction of the phase behavior of humid IND-PVP in the presence of moisture.

4.3.4 Naproxen + water

The binary interaction parameter of the mixture NAP-water could not be fitted to water sorption data due to lack of experimental data. Thus, the k_{ij} was fitted to SLE experimental data [151] as shown in Figure 4.31.

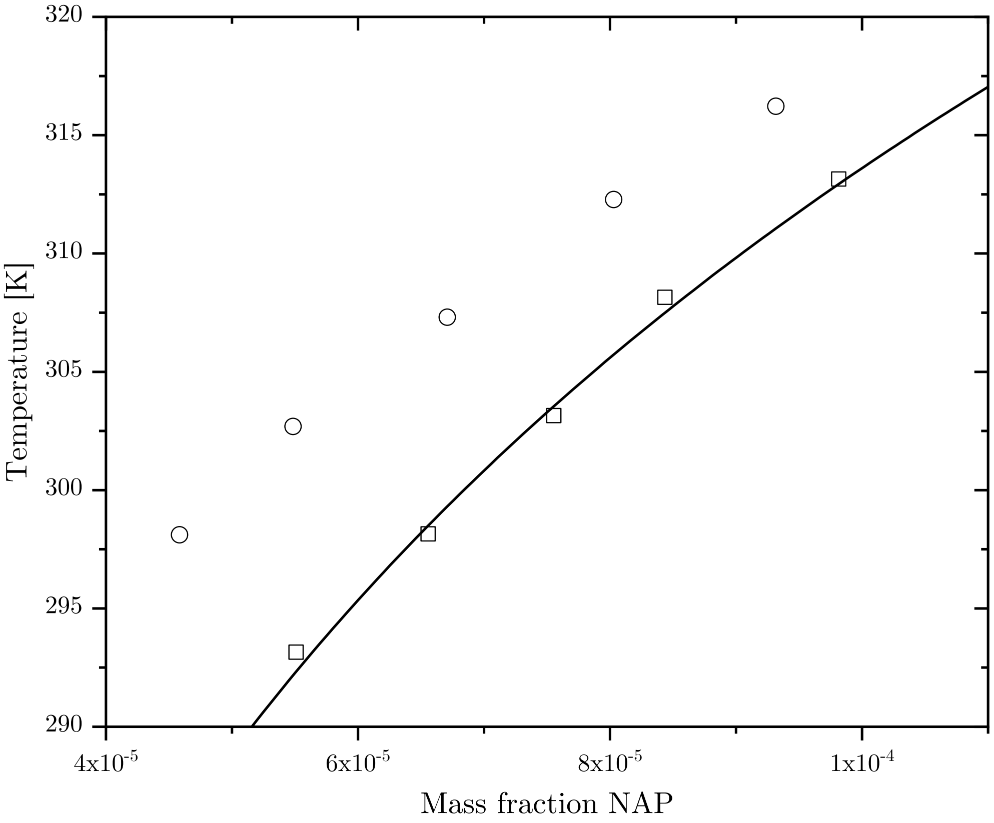

Figure 4.31: Experimental (□ [151], ○ [155]) and calculated (— SL) SLE of NAP-water at 1 bar. The calculations with SL were carried out using the SL parameters of NAP and water listed in Tables 4.1 and 4.3, respectively, the fusion properties listed in Table 4.2 and the binary interaction parameter listed in Table 4.8. The experimental data from Paus et al. [155] is shown only for comparison and was not used to fit the k_{ij}.

Pacheco and Martínez [151] measured the solubility of crystalline NAP in ethanol-water solutions via UV spectrophotometry as described in section 2.3.2.2. The density of the saturated solutions used to convert molarity into the mole fraction was measured using a digital densimeter, whereas each reported value was the average of three measurements [151].

Paus et al. [155] measured the SLE of NAP in water shown in Figure 4.31 also by using UV spectrophotometry as described in section 2.3.2.2. The densities of the saturated solutions were assumed to be equal to the density of pure water due to the low solubility, whereas a temperature-dependent correlation was used for calculations and the reported values were the average of three measurements [155].

Since the density of the saturated solutions was actually measured and written values of the NAP solubility in water were reported by Pacheco and Martínez [151], the data reported by Paus et al. [155] was not used to fit the binary interaction parameter of NAP-water. Nevertheless, both data sets [151, 155] are in good agreement with each other, given the low solubility of NAP in water as shown in Figure 4.31. The fitted binary interaction parameter according to equation (3.12) of NAP-water is listed in Table 4.8 resulting in excellent agreement with the experimental data [151] as shown in Figure 4.31.

4.3.5 Naproxen + poly vinyl pyrrolidone + water

The experimental [142] and predicted water sorption in the ASD NAP-PVP is shown in Figure 4.32.

Prudic et al. [142] prepared the ASD NAP-PVP using the same procedure as for IND-PVP, whereas the vapor uptake in the ASD shown in Figure 4.32 was measured using the gravimetric method as previously described in section 4.3.3.

The predicted water sorption in NAP-PVP shown in Figure 4.32 is in excellent agreement with the experimental data [142] for the ASD containing 30 % NAP. On the other hand, the predicted water sorption in the ASDs containing 50 % and 80 % NAP at constant RH are higher than the experimental data [142]. The disagreement between prediction and experiment [142] grows with the NAP content in the dry ASD. This behavior indicates that the predicted water sorption in amorphous NAP is overestimated by the SL EOS. The blue line shown in Figure 4.32 denotes the water sorption in amorphous NAP, however, no experimental data was found in the literature for comparison. Nevertheless, the SL calculation correctly predicts the order of magnitude of water sorption in NAP, even after fitting the binary interaction parameter to SLE data.

Moreover, the predicted glass temperature of NAP-PVP over the absorbed moisture is shown in Figure 4.33. Unfortunately, no experimental data was found in the literature for comparison.

The predicted T_G of humid NAP-PVP shown in Figure 4.33 exhibits a similar behavior as the ASD composed of IND-PVP shown in Figure 4.28. However, the formulation containing NAP can absorb almost three times more water than the one containing IND according to the prediction.

Furthermore, formulations containing 70 % or more NAP will relax to the corresponding metastable liquid if stored at room temperature due to the lower T_G of NAP compared to IND. However, additional experimental data is still required to validate the predicted behavior.

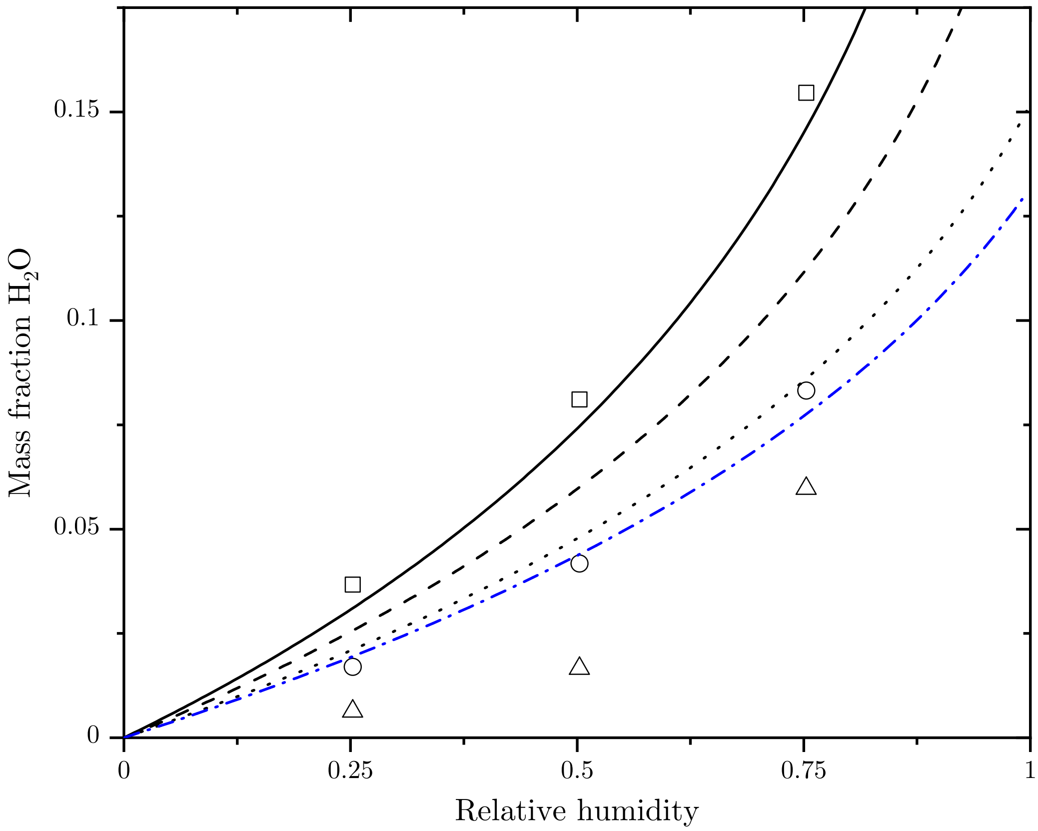

Figure 4.32: Experimental (□ 30 % NAP, ○ 50 % NAP, △ 80 % NAP) [142] and predicted (── SL 30 % NAP, – – SL 50 % NAP, ··· SL 80 % NAP, – · – 100 % NAP) water absorption in NAP-PVP over the relative humidity at 298.15 K and 1 bar. The percentages denote mass fractions of dry ASDs. All calculations were performed using the SL parameters of NAP and PVP listed in Table 4.1, the SL parameters of water listed in Table 4.3 and the binary interaction parameters listed in Tables 4.7 and 4.8.

Finally, the experimental T_G of the humid ASD NAP-PVP [58] such as the predicted ternary phase diagram and glass temperature at atmospheric pressure are depicted in Figure 4.34.

Paudel et al. [58] measured the T_G of the humid ASD NAP-PVP shown in Figure 4.34 via mDSC. The ASDs were prepared by spray drying using dicloromethane as solvent, whereas the exact parameters of the apparatus are given in the original publication [58]. Prior to the T_G measurement, a heating cycle was applied on the samples to remove their thermal history [58]. Thereafter, the samples were cooled to −20 °C and held isothermally for 2 min upon applying another heating cycle at 2 K min^{-1} using a modulation of 0.0212 °C every 40 s, whereas the T_G was measured in duplicate for all samples [58]. The reported values shown in Figure 4.34 were measured on the second heating run and the water content of the ASDs was estimated using a thermogravimetric analysis by drying the samples from 30 °C to 160 °C using dry nitrogen [58].

The predicted T_G of the ternary system NAP-PVP-water shown in Figure 4.34 is in very good agreement with the experimental glass temperature [58], even though the plasticization effect of water on the ASD is always slightly overestimated. Furthermore and according to the prediction, the region where the formulation containing NAP is stable against recrystallization is narrower than in formulations containing IND, if

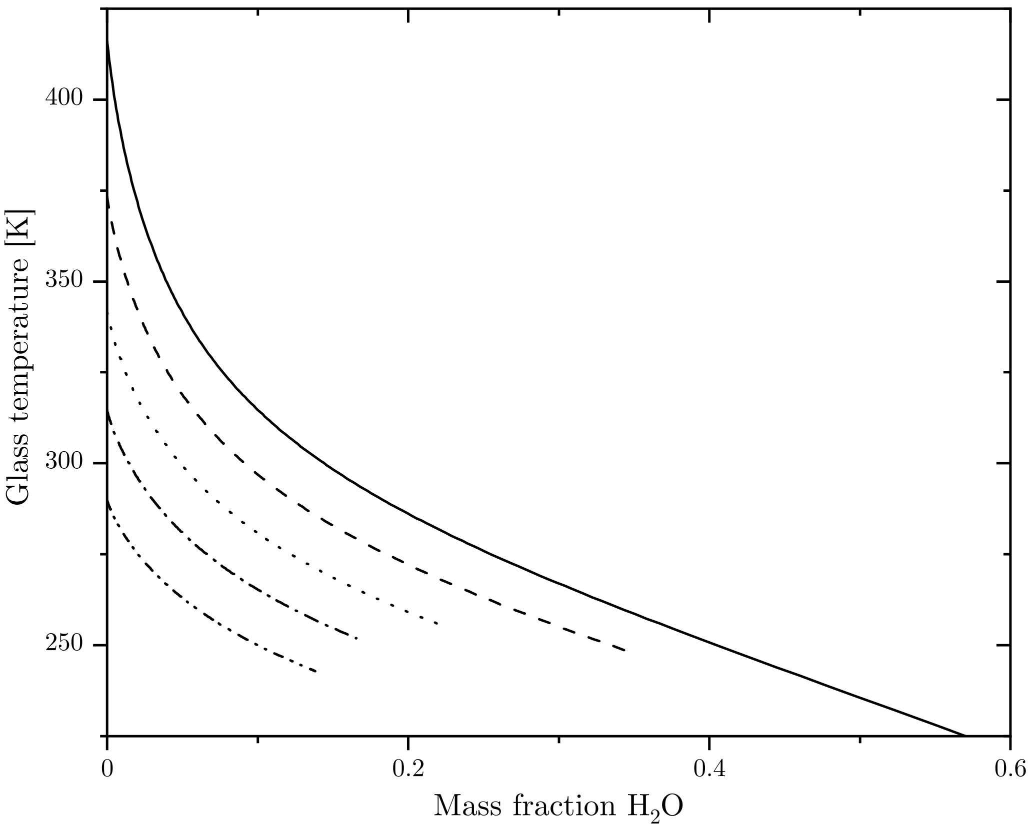

Figure 4.33: Predicted (— GET 10 % NAP, – – GET 30 % NAP, · · · GET 50 % NAP, – · – GET 70 % NAP, – · · GET 90 % NAP) glass temperature of humid NAP-PVP stored at 300 K and 1 bar. The percentages denote mass fractions of dry ASDs. All calculations were performed using the SL parameters of NAP and PVP listed in Table 4.1, the SL parameters of water listed in Table 4.3, the k_p of NAP and PVP listed in Table 4.5, the k_p of water listed in Table 4.8 and the binary interaction parameters listed in Tables 4.7 and 4.8.

stored at room temperature. For instance, a dry ASD of NAP-PVP stored at 300 K will eventually recrystallize for NAP loads higher than ≈ 25 % weight according to Figure 4.34. Besides, the absorbed water at maximal RH exceeds 20 %, whereas the corresponding equilibrium temperature is in the vicinity of 330 K. Consequently, a formulation containing NAP-PVP stored at 100 % RH and room temperature will recrystallize much faster, as the corresponding predicted T_G is below 270 K.

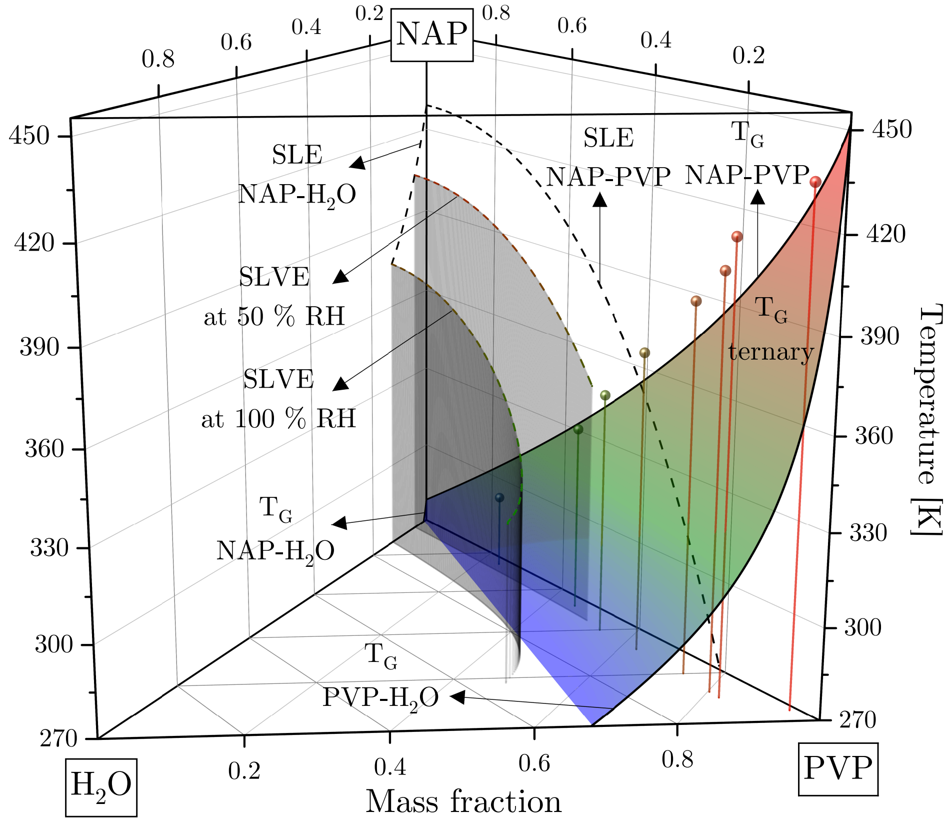

Figure 4.34: Experimental [58] and predicted (— T_G prediction of corresponding binary subsystem via GET, – – SL calculation of corresponding binary SLEs, ··· SLVE prediction of ternary system via SL, colored surface: T_G prediction of ternary system, whereas gray surfaces denote the projection of the ternary SLVE lines on the composition plane at 50 % and 100 % RH) phase diagram and glass temperature of NAP-PVP-water at 1 bar. All calculations were performed using the SL parameters of NAP and PVP listed in Table 4.1, the SL parameters of water listed in Table 4.3, the fusion properties of NAP listed in Table 4.2, the k_p of NAP and PVP listed in Table 4.5, the k_p of water listed in Table 4.8 and the binary interaction parameters listed in Table 4.7 and 4.8.

5 Conclusions and outlook

In the present work, a model to predict the glass temperature and phase behavior of dry and humid ASDs was developed by combining the GET [9, 22] with the SL EOS [23, 24].

First of all, the SL parameters of the polymer PVP and the APIs IBU and IND were fitted to pure PVT experimental data available in the literature. The density of all three components over the pressure and temperature could be described with an unambiguous SL parameter set in very good agreement with experimental data. On the other hand, the SL parameters of NAP and GRI were fitted to experimental binary SLE data in pure organic solvents, since no PVT data of the pure components was found in the literature. Fitting the SL parameters to SLE data in several solvents is far from trivial and needs to be systematically performed as described in detail in section 3.5. The SLEs of NAP and GRI in organic solvents could be described in very good agreement with the experimental data using, at most, a linearly temperature-dependent binary interaction parameter.

Furthermore, the relaxation time and the T_G of IBU and IND as a function of pressure were predicted using the previously adjusted SL parameters after fitting the adjustable parameter, k_p in equation (2.11), to the experimentally measured glass temperature of the pure components at atmospheric pressure. In the case of IBU, the relaxation time was overestimated in several orders of magnitude between 10 MPa and 1000 MPa. Consequently, the T_G of IBU as a function of pressure was also overestimated, although the linear trend was correctly predicted. On the other hand, the relaxation time of IND as a function of pressure was overestimated in only a few orders of magnitude, whereas the T_G was predicted in excellent agreement with the experimental data from atmospheric pressure up to 250 MPa. Therefore, it can be concluded that the pressure range in which the SL parameters of the API are fitted is decisive for the correct prediction of the glass temperature as a function of pressure. Although the PVT behavior of IBU could be predicted in good agreement with the experimental data, there is a small discrepancy at elevated pressures. Furthermore, the SL parameters of IBU were fitted using data from 10 MPa up to 160 MPa. Thus, predicting the T_G at higher pressures includes a rough extrapolation. In the case of IND, the SL parameters were adjusted between 1 MPa and 200 MPa, which is a very similar pressure range within which T_G was correctly predicted.

Moreover, the binary interaction parameter included in the SL EOS of the dry ASDs composed of PVP and IBU, IND and NAP, respectively, was fitted to experimental SLE data obtaining a temperature-independent value in all cases. The T_G of the dry ASDs was predicted using the adjusted k_{ij}s yielding a very good agreement with the experimentally measured T_G. Besides, the T_G predictions of ASDs containing IND and NAP were better than the corresponding calculation using the GT equation (2.6). In the case of the ASD PVP-IBU, the prediction was close to the GT equation (2.6), however, the empirical correlation still delivered better results compared to the experimental value of T_G.

Additionally, the binary interaction parameters of the mixtures containing water were fitted to isothermal experimental water sorption data above the glass temperature, in the case of PVP and IND. The water sorption of PVP above T_G could be well described in agreement with experimental data using a linearly temperature-dependent k_{ij}, however, the water sorption in the glassy state was overestimated at all investigated temperatures. The glass temperature of PVP-water was predicted using the fitted k_{ij} yielding a better description of the experimentally measured T_G than the GT equation (2.6). In the case of IND-water, the water sorption at 298.15 K and 303.15 K could be well described in agreement with experimental data using a linearly temperature-dependent k_{ij}. Since the water sorption in IND is greatly lower than in PVP, both regions below and above the T_G could be well described with the adjusted binary interaction parameter. However, the GET prediction and GT calculation using equation (2.6) of T_G overestimate the experimental data for still unknown reasons. Conversely, the binary interaction parameter of the mixture NAP-water was fitted to experimental SLE data also yielding a temperature-dependent k_{ij}. The water sorption of pure NAP could not be validated due to lack of experimental values, however, the water sorption in the ASD PVP-NAP was predicted yielding a slight overestimation compared to the experimentally measured water sorption for ASDs with 50 % and 80 % drug load. Moreover, the predicted water sorption in the ASD containing 30 % NAP was in very good agreement with the experimental data.

Finally, the phase equilibria of the ternary systems IND-PVP-water and NAP-PVP-water was calculated after expanding the SL EOS to ternary mixture without using any further adjustable parameters. In the case of the humid ASD containing IND, the water sorption was predicted in very good agreement with the experimental data for drug loads of 80 %, however, the water sorption in ASDs containing lower drug loads was slightly underestimated. On the other hand, the T_G of the humid ASD IND-PVP containing drug loads varying from 10 % to 90 % was predicted in very good agreement with the experimentally measured values with a maximal deviation of approximately 12 K at a water mass fraction of 0.16. Furthermore, the T_G of the humid formulation IND-PVP as a function of the drug load at different relative humidities was also predicted and always in better agreement with the experimental data than the GT calculation using equation (2.8). The predicted ternary SLVE of the system IND-PVP-water was also presented, however, the prediction needs to be validated against experimental data still missing from the literature. Conversely, the glass temperature of the humid ASD NAP-PVP was predicted in very good agreement with experimental data without using any further adjustable parameters to describe the ternary mixture or to adjust the glass temperature of the humid ASD.

In summary, it could be shown that the T_G and the phase behavior of ASDs containing PVP and IBU, IND and NAP, respectively, can be described in agreement with experimental data disregarding association between the components. Furthermore, it could be shown that the AG relation [26] can still be used to this day to accurately predict the glass transition of mixtures containing polymers and pharmaceutical components by using the entropy density as considered in the GET [9, 22] and fitting the parameter k_p included in the activation energy via equation (2.11) to the experimentally measured T_G of the pure component. Even though the relaxation time cannot be quantitatively described with the presented model, the influence of pressure on the glass temperature may be well described, given that the SL parameters are fitted within the same pressure range in which the T_G is to be investigated. Insofar, the model presented here may be used to analyze the influence of processing and storage parameters on the phase behavior and the glass temperature of ASDs. However, its suitability for other formulations containing different polymers and APIs needs to be further investigated.

This page is intentionally left blank.

References

[1] P. G. Debenedetti. *Metastable liquids.* Princeton University Press, 1997. ISBN 9780691213941.

[2] S. Vyazovkin. *Isoconversional kinetics of thermally stimulated processes.* Springer, 2015. ISBN 978-3-319-14174-9.

[3] A. Mathers, F. Hassouna, M. Klajmon, and M. Fulem. Comparative study of DSC-based protocols for API-polymer solubility determination. *Molecular Pharmaceutics*, 18(4):1742–1757, 2021. doi: 10.1021/acs.molpharmaceut.0c01232.

[4] K. Löbmann, R. Laitinen, H. Grohganz, K. C. Gordon, C. Strachan, and T. Rades. Coamorphous drug systems: Enhanced physical stability and dissolution rate of indomethacin and naproxen. *Molecular Pharmaceutics*, 8(5): 1919–1928, 2011. doi: 10.1021/mp2002973.

[5] C. Huang, S. Ruan, T. Cai, and L. Yu. Fast surface diffusion and crystallization of amorphous griseofulvin. *The Journal of Physical Chemistry*, 121(40):9463–9468, 2017. doi: 10.1021/acs.jpcb.7b07319.

[6] N. Shah, H. Sandhu, D.S. Choi, H. Choksi, and A. W. Malick, editors. *Amorphous solid dispersions: Theory and practice.* Springer New York, 2014. ISBN 9781493915989.

[7] M. Rams-Baron, R. Jachowicz, E. Boldyreva, D. Zhou, W. Jamroz, and M. Paluch. Why amorphous drugs? In *Amorphous Drugs*, pages 1–7. Springer International Publishing, 2018. ISBN 978-3-319-72001-2.

[8] B. C. Hancock and M. Parks. What is the true solubility advantage for amorphous pharmaceuticals? *Pharmaceutical Research*, 17(4):397–404, 2000. doi: 10.1023/A:1007516718048.

[9] J. Dudowicz, K. F. Freed, and J. F. Douglas. Generalized entropy theory of polymer glass formation. *Advances in Chemical Physics*, 137:125–222, 2007. doi: 10.1002/9780470238080.ch3.

[10] S. V. Bhujbal, B. Mitra, U. Jain, Y. Gong, A. Agrawal, S. Karki, L. S. Taylor, S. Kumar, and Q. Tony Zhou. Pharmaceutical amorphous solid dispersion: A review of manufacturing strategies. *Acta Pharmaceutica Sinica B*, 11(8):2505–2536, 2021. doi: 10.1016/j.apsb.2021.05.014.

[11] S. Tambe, D. Jain, S. K. Meruva, G. Rongala, A. Juluri, G. Nihalani, H. K. Mamidi, P. K. Nukala, and P. K. Bolla. Recent advances in amorphous solid dispersions: Preformulation, formulation strategies, technological advancements and characterization. *Pharmaceutics*, 14(10):2203, 2022. doi: 10.3390/pharmaceutics14102203.

[12] S. Janssens and G. Van den Mooter. Review: Physical chemistry of solid dispersions. *Journal of Pharmacy and Pharmacology*, 61(12):1571–1586, 2009. doi: 10.1211/jpp.61.12.0001.

[13] S. Baghel, H. Cathcart, and N. J. O'Reilly. Polymeric amorphous solid dispersions: A review of amorphization, crystallization, stabilization, solid-state characterization, and aqueous solubilization of biopharmaceutical classification system class ii drugs. *Journal of Pharmaceutical Sciences*, 105(9):2527–2544, 2016. doi: 10.1016/j.xphs.2015.10.008.

[14] X. Lin, Y. Hu, L. Liu, L. Su, N. Li, J. Yu, B. Tang, and Z. Yang. Physical stability of amorphous solid dispersions: A physicochemical perspective with thermodynamic, kinetic and environmental aspects. *Pharmaceutical Research*, 35(6):125, 2018. doi: 10.1007/s11095-018-2408-3.

[15] C. Luebbert, F. Huxoll, and G. Sadowski. Amorphous-amorphous phase separation in API/polymer formulations. *Molecules*, 22(2), 2017. doi: 10.3390/molecules22020296.

[16] C. Luebbert and G. Sadowski. Moisture-induced phase separation and recrystallization in amorphous solid dispersions. *International Journal of Pharmaceutics*, 532(1):635–646, 2017. doi: 10.1016/j.ijpharm.2017.08.121.

[17] C. Luebbert, C. Klanke, and G. Sadowski. Investigating phase separation in amorphous solid dispersions via Raman mapping. *International Journal of Pharmaceutics*, 535(1-2):245–252, 2018. doi: 10.1016/j.ijpharm.2017.11.014.

[18] S. Dohrn, C. Luebbert, K. Lehmkemper, S. O. Kyeremateng, M. Degenhardt, and G. Sadowski. Solvent influence on the phase behavior and glass transition of amorphous solid dispersions. *European Journal of Pharmaceutics and Biopharmaceutics*, 158:132–142, 2021. doi: 10.1016/j.ejpb.2020.11.002.

[19] J. Gross and G. Sadowski. Perturbed-chain SAFT: An equation of state based on a perturbation theory for chain molecules. *Industrial & Engineering Chemistry Research*, 40(4):1244–1260, 2001. doi: 10.1021/ie0003887.

[20] A. Prudic, Y. Ji, and G. Sadowski. Thermodynamic phase behavior of API/polymer solid dispersions. *Molecular Pharmaceutics*, 11(7):2294–2304, 2014. doi: 10.1021/mp400729x.

[21] M. Gordon and J. S. Taylor. Ideal copolymers and the second-order transitions of synthetic rubbers. I. Non-crystalline copolymers. *Journal of Applied Chemistry*, 2(9):493–500, 1952. doi: 10.1002/jctb.5010020901.

[22] J. Dudowicz, K. F. Freed, and J. F. Douglas. Entropy theory of polymer glass formation revisited. I. General formulation. *The Journal of Chemical Physics*, 124(6), 2006. doi: 10.1063/1.2166391.

[23] I. C. Sanchez and R. H. Lacombe. An elementary molecular theory of classical fluids. Pure fluids. *The Journal of Physical Chemistry*, 80(21):2352–2362, 1976. doi: 10.1021/j100562a008.

[24] I. C. Sanchez and R. H. Lacombe. Statistical thermodynamics of polymer solutions. *Macromolecules*, 11(6):1145–1156, 1978. doi: 10.1021/ma60066a017.

[25] J. H. Gibbs and E. A. DiMarzio. Nature of the glass transition and the glassy state. *The Journal of Chemical Physics*, 28(3):373–383, 1958. doi: 10.1063/1.1744141.

[26] G. Adam and J. H. Gibbs. On the temperature dependence of cooperative relaxation properties in glass–forming liquids. *The Journal of Chemical Physics*, 43 (1):139–146, 1965. doi: 10.1063/1.1696442.

[27] P. G. Debenedetti. Supercooled and glassy water. *Journal of Physics - Condensed Matter*, 15(45):R1669–R1726, 2003. doi: 10.1088/0953-8984/15/45/R01.

[28] L. Berthier and G. Biroli. Theoretical perspective on the glass transition and amorphous materials. *Reviews of Modern Physics*, 83(2):587–645, 2011. doi: 10.1103/RevModPhys.83.587.

[29] L. Berthier, M. Ozawa, and C. Scalliet. Configurational entropy of glass-forming liquids. *The Journal of Chemical Physics*, 150(16):160902, 2019. doi: 10.1063/1.5091961.

[30] G. P. Johari. Phenomenological aspects of glass transition and molecular motions in glasses. In K. L. Ngai and G. B. Wright, editors, *Relaxations in complex systems*, pages 17–41. Naval Research Laboratory and Office of Naval Research, 1985.

[31] H. Vogel. Das Temperaturabhängigkeitsgesetz der Viskosität von Flüssigkeiten. *Physikalische Zeitschrift*, 22:645–646, 1921.

[32] G. S. Fulcher. Analysis of recent measurements of the viscosity of glasses. *Journal of the American Ceramic Society*, 8(6):339–355, 1925. doi: 10.1111/j.1151-2916.1925.tb16731.x.

[33] G. Tammann and W. Hesse. Die Abhängigkeit der Viscosität von der Temperatur bei unterkühlten Flüssigkeiten. *Zeitschrift für anorganische und allgemeine Chemie*, 156(1):245–257, 1926. doi: 10.1002/zaac.19261560121.

[34] M. L. Williams. The temperature dependence of mechanical and electrical relaxations in polymers. *The Journal of Physical Chemistry*, 59(1):95–96, 1955. doi: 10.1021/j150523a029.

[35] M. L. Williams, R. F. Landel, and J. D. Ferry. The temperature dependence of relaxation mechanisms in amorphous polymers and other glass-forming liquids. *Journal of the American Chemical Society*, 77(14):3701–3707, 1955. doi: 10.1021/ja01619a008.

[36] C. A. Angell and L. M. Torell. Short time structural relaxation processes in liquids: Comparison of experimental and computer simulation glass transitions on picosecond time scales. *The Journal of Chemical Physics*, 78(2):937–945, 1983. doi: 10.1063/1.444798.

[37] C. T. Moynihan, P. B. Macedo, C. J. Montrose, P. K. Gupta, M. A. DeBolt, J. F. Dill, B. E. Dom, P. W. Drake, A. J. Easteal, P. B. Elterman, R. P. Moeller, H. Sasabe, and J. A. Wilder. Structural relaxation in vitreous materials. *Annals of the New York Academy of Sciences*, 279(1):15–35, 1976. doi: 10.1111/j.1749-6632.1976.tb39688.x.

[38] D. Cangialosi. Dynamics and thermodynamics of polymer glasses. *Journal of Physics - Condensed Matter*, 26(15):153101, 2014. doi: 10.1088/0953-8984/26/15/153101.

[39] R. Richert. Supercooled liquids and glasses by dielectric relaxation spectroscopy. *Advances in Chemical Physics*, 156:101–195, 2014. doi: 10.1002/9781118949702.ch4.

[40] W. Kauzmann. The nature of the glassy state and the behavior of liquids at low temperatures. *Chemical Reviews*, 43(2):219–256, 1948. doi: 10.1021/cr60135a002.

[41] R. S. Welch, E. D. Zanotto, C. J. Wilkinson, D. R. Cassar, M. Montazerian, and J. C. Mauro. Cracking the kauzmann paradox. *Acta Materialia*, 254:118994, 2023. doi: 10.1016/j.actamat.2023.118994.

[42] G. P. Bettinetti, P. Mura, F. Giordano, and M. Setti. Thermal behaviour and physicochemical properties of naproxen in mixtures with polyvinylpyrrolidone. *Thermochimica Acta*, 199:165–171, 1992. doi: 10.1016/0040-6031(92)80260-4.

[43] F. L. Lopez, G. C. Shearman, S. Gaisford, and G. R. Williams. Amorphous formulations of indomethacin and griseofulvin prepared by electrospinning. *Molecular Pharmaceutics*, 11(12):4327–4338, 2014. doi: 10.1021/mp500391y.

[44] M. M. Knopp, N. E. Olesen, P. Holm, P. Langguth, R. Holm, and T. Rades. Influence of polymer molecular weight on drug-polymer solubility: A comparison between experimentally determined solubility in PVP and prediction derived from solubility in monomer. *Journal of Pharmaceutical Sciences*, 104(9):2905–2912, 2015. doi: 10.1002/jps.24410.

[45] B. Wang, D. Wang, S. Zhao, X. Huang, J. Zhang, Y. Lv, X. Liu, G. Lv, and X. Ma. Evaluate the ability of PVP to inhibit crystallization of amorphous solid dispersions by density functional theory and experimental verify. *European Journal of Pharmaceutical Sciences*, 96:45–52, 2017. doi: 10.1016/j.ejps.2016.08.046.

[46] J. E. McKinney and M. Goldstein. PVT relationships for liquid and glassy poly(vinyl acetate). *Journal of research of the National Bureau of Standards*, 78A(3):331–353, 1974. doi: 10.6028/jres.078A.018.

[47] K. L. Ngai and G. B. Wright, editors. *Relaxations in complex systems.* Naval Research Laboratory and Office of Naval Research, 1985.

[48] K. L. Ngai. Universal properties of relaxation and diffusion in complex materials: Originating from fundamental physics with rich applications. *Progress in Materials Science*, 139:101130, 2023. doi: 10.1016/j.pmatsci.2023.101130.

[49] C. A. Angell. Relaxation in liquids, polymers and plastic crystals – strong/fragile patterns and problems. *Journal of Non-Crystalline Solids*, 131-133:13–31, 1991. doi: 10.1016/0022-3093(91)90266-9.

[50] I. M. Hodge. Strong and fragile liquids – a brief critique. *Journal of Non-Crystalline Solids*, 202(1-2):164–172, 1996. doi: 10.1016/0022-3093(96)00151-2.

[51] G. P. Johari, S. Kim, and Ravi M. Shanker. Dielectric studies of molecular motions in amorphous solid and ultraviscous acetaminophen. *Journal of Pharmaceutical Sciences*, 94(10):2207–2223, 2005. doi: 10.1002/jps.20455.

[52] K. L. Ngai. Dynamic and thermodynamic properties of glass-forming substances. *Journal of Non-Crystalline Solids*, 275(1-2):7–51, 2000. doi: 10.1016/S0022-3093(00)00238-6.

[53] J. Dudowicz, J. F. Douglas, and K. F. Freed. The meaning of the universal WLF parameters of glass-forming polymer liquids. *The Journal of Chemical Physics*, 142(1):014905, 2015. doi: 10.1063/1.4905216.

[54] M. Yoshioka, B. C. Hancock, and G. Zografi. Inhibition of indomethacin crystallization in poly(vinylpyrrolidone) coprecipitates. *Journal of Pharmaceutical Sciences*, 84(8):983–986, 1995. doi: 10.1002/jps.2600840814.

[55] R. Nair, N. Nyamweya, S. Gönen, L. J. Martínez-Miranda, and S. W. Hoag. Influence of various drugs on the glass transition temperature of poly(vinylpyrrolidone): A thermodynamic and spectroscopic investigation. *International Journal of Pharmaceutics*, 225(1-2):83–96, 2001. doi: 10.1016/S0378-5173(01)00767-0.

[56] K. J. Crowley and G. Zografi. Water vapor absorption into amorphous hydrophobic drug/poly(vinylpyrrolidone) dispersions. *Journal of Pharmaceutical Sciences*, 91(10):2150–2165, 2002. doi: 10.1002/jps.10205.

[57] K. Gong, R. Viboonkiat, I. U. Rehman, G. Buckton, and J. A. Darr. Formation and characterization of porous indomethacin-PVP coprecipitates prepared using solvent-free supercritical fluid processing. *Journal of Pharmaceutical Sciences*, 94(12):2583–2590, 2005. doi: 10.1002/jps.20474.

[58] A. Paudel, J. van Humbeeck, and G. van den Mooter. Theoretical and experimental investigation on the solid solubility and miscibility of naproxen in poly(vinylpyrrolidone). *Molecular Pharmaceutics*, 7(4):1133–1148, 2010. doi: 10.1021/mp100013p.

[59] A. Paudel, E. Nies, and G. van den Mooter. Relating hydrogen-bonding interactions with the phase behavior of naproxen/PVP K-25 solid dispersions: Evaluation of solution-cast and quench-cooled films. *Molecular Pharmaceutics*, 9(11):3301–3317, 2012. doi: 10.1021/mp3003495.

[60] A. Prudic, T. Kleetz, M. Korf, Y. Ji, and G. Sadowski. Influence of copolymer composition on the phase behavior of solid dispersions. *Molecular Pharmaceutics*, 11(11):4189–4198, 2014. doi: 10.1021/mp500412d.

[61] M. M. Knopp, N. E. Olesen, P. Holm, K. Löbmann, R. Holm, P. Langguth, and T. Rades. Evaluation of drug-polymer solubility curves through formal statistical analysis: Comparison of preparation techniques. *Journal of Pharmaceutical Sciences*, 104(1):44–51, 2015. doi: 10.1002/jps.24207.

[62] K. Lehmkemper, S. O. Kyeremateng, O. Heinzerling, M. Degenhardt, and G. Sadowski. Impact of polymer type and relative humidity on the long-term physical stability of amorphous solid dispersions. *Molecular Pharmaceutics*, 14(12):4374–4386, 2017. doi: 10.1021/acs.molpharmaceut.7b00492.

[63] K. Lehmkemper, S. O. Kyeremateng, O. Heinzerling, M. Degenhardt, and G. Sadowski. Long-term physical stability of PVP- and PVPVA-amorphous solid dispersions. *Molecular Pharmaceutics*, 14(1):157–171, 2017. doi: 10.1021/acs.molpharmaceut.6b00763.

[64] Q. Lu and G. Zografi. Phase behavior of binary and ternary amorphous mixtures containing indomethacin, citric acid, and pvp. *Pharmaceutical Research*, 15(8):1202–1206, 1998. doi: 10.1023/a:1011983606606.

[65] G. B. McKenna. Looking at the glass transition: Challenges of extreme time scales and other interesting problems. *Rubber Chemistry and Technology*, 93(1):79–120, 2020. doi: 10.5254/rct.20.80376.

[66] K. H. Meyer. Über die Mischungsentropie von Systemen mit langkettigen Verbindungen und ihre statistische Erklärung. *Zeitschrift für Physikalische Chemie*, 44B(1):383–391, 1939. doi: 10.1515/zpch-1939-4429.

[67] K. H. Meyer. Propriétés de polymères en solution xvi. interprétation statistique des propriétés thermodynamiques de systèmes binaires liquides. *Helvetica Chimica Acta*, 23(1):1063–1070, 1940. doi: 10.1002/hlca.194002301130.

[68] M. L. Huggins. Solutions of long chain compounds. *The Journal of Chemical Physics*, 9(5):440–440, 1941. doi: 10.1063/1.1750930.

[69] P. J. Flory. Thermodynamics of high polymer solutions. *The Journal of Chemical Physics*, 10(1):51–61, 1942. doi: 10.1063/1.1723621.

[70] M. L. Huggins. Thermodynamic properties of solutions of long-chain compounds. *Annals of the New York Academy of Sciences*, 43(1):1–32, 1942. doi: 10.1111/j.1749-6632.1942.tb47940.x.

[71] P. Ehrenfest. Phasenumwandlungen im ueblichen und erweiterten Sinn, classifiziert nach den entsprechenden Singularitaeten des thermodynamischen Potentiales. *Leiden Comm. Suppl.*, 756, 1933.

[72] G. P. Johari. A resolution for the enigma of a liquid's configurational entropy-molecular kinetics relation. *The Journal of Chemical Physics*, 112(20):8958–8969, 2000. doi: 10.1063/1.481509.

[73] K. L. Ngai. Synergy of entropy and intermolecular coupling in supercooling liquids. *The Journal of Chemical Physics*, 111(8):3639–3643, 1999. doi: 10.1063/1.479644.

[74] C. A. Angell. Strong and fragile liquids. In K. L. Ngai and G. B. Wright, editors, *Relaxations in complex systems*, pages 3–11. Naval Research Laboratory and Office of Naval Research, 1985.

[75] J. Dudowicz, J. F. Douglas, and K. F. Freed. Advances in the generalized entropy theory of glass-formation in polymer melts. *The Journal of Chemical Physics*, 141(23):234903, 2014. doi: 10.1063/1.4903842.

[76] A. M. Nemirovsky, M. G. Bawendi, and K. F. Freed. Lattice models of polymer solutions: Monomers occupying several lattice sites. *The Journal of Chemical Physics*, 87(12):7272–7284, 1987. doi: 10.1063/1.453320.

[77] J. Dudowicz and K. F. Freed. Effect of monomer structure and compressibility on the properties of multicomponent polymer blends and solutions: 1. lattice cluster theory of compressible systems. *Macromolecules*, 24(18):5076–5095, 1991. doi: 10.1021/ma00018a014.

[78] K.F. Freed and J. Dudowicz. A lattice-model molecular theory for the properties of polymer blends. *Trends in Polymer Science*, 3(8):248–255, 1995.

[79] K. F. Freed and J. Dudowicz. Lattice cluster theory for pedestrians: Models for random copolymer blends. *Macromolecular Symposia*, 149(1):11–16, 2000. doi: 10.1002/1521-3900(200001)149:1⟨11::aid-masy11⟩3.0.co;2-n.

[80] J. Dudowicz, K. F. Freed, and J. F. Douglas. Fragility of glass-forming polymer liquids. *The Journal of Physical Chemistry B*, 109(45):21350–21356, 2005. doi: 10.1021/jp053693k.

[81] M. Roericht. *Thermodynamik des Glasübergangs*. PhD thesis, Karlsruher Institut für Technologie, 2021.

[82] J. Dudowicz, K. F. Freed, and J. F. Douglas. Concentration fluctuations in miscible polymer blends: Influence of temperature and chain rigidity. *The Journal of Chemical Physics*, 140(19):194901, 2014. doi: 10.1002/9780470238080.ch3.

[83] J. G. Kirkwood and F. P. Buff. The statistical mechanical theory of solutions. I. *The Journal of Chemical Physics*, 19(6):774–777, 1951. doi: 10.1063/1.1748352.

[84] A. Ben-Naim. Inversion of the Kirkwood–Buff theory of solutions: Application to the water–ethanol system. *The Journal of Chemical Physics*, 67(11):4884–4890, 1977. doi: 10.1063/1.434669.

[85] G. L. Amidon, H. Lennernäs, V. P. Shah, and J. R. Crison. A theoretical basis for a biopharmaceutic drug classification: The correlation of in vitro drug product dissolution and in vivo bioavailability. *Pharmaceutical Research*, 12(3):413–420, 1995. doi: 10.1023/A:1016212804288.

[86] B. C. Hancock and G. Zografi. Characteristics and significance of the amorphous state in pharmaceutical systems. *Journal of Pharmaceutical Sciences*, 86(1):1–12, 1997. doi: 10.1021/js9601896.

[87] X. Ma and R. O. Williams. Characterization of amorphous solid dispersions: An update. *Journal of Drug Delivery Science and Technology*, 50:113–124, 2019. doi: 10.1016/j.jddst.2019.01.017.

[88] S. Dedroog, T. Pas, B. Vergauwen, C. Huygens, and G. van den Mooter. Solid-state analysis of amorphous solid dispersions: Why DSC and XRPD may not be regarded as stand-alone techniques. *Journal of Pharmaceutical and Biomedical Analysis*, 178:112937, 2020. doi: 10.1016/j.jpba.2019.112937.

[89] C. Ahlneck and G. Zografi. The molecular basis of moisture effects on the physical and chemical stability of drugs in the solid state. *International Journal of Pharmaceutics*, 62(2-3):87–95, 1990. doi: 10.1016/0378-5173(90)90221-O.

[90] C. A. Oksanen and G. Zografi. Molecular mobility in mixtures of absorbed water and solid poly(vinylpyrrolidone). *Pharmaceutical Research*, 10(6):791–799, 1993. doi: 10.1023/A:1018988506336.

[91] H. Levine and L. Slade. Water as a plasticizer: Physico-chemical aspects of low-moisture polymeric systems. In F. Franks, editor, *Water Science Reviews 3*, pages 79–185. Cambridge University Press, 2009. ISBN 9780521350143.

[92] B. C. Hancock and G. Zografi. The relationship between the glass transition temperature and the water content of amorphous pharmaceutical solids. *Pharmaceutical Research*, 11(4):471–477, 1994. doi: 10.1023/A:1018941810744.

[93] C. A. Oksanen and G. Zografi. The relationship between the glass transition temperature and water vapor absorption by poly(vinylpyrrolidone). *Pharmaceutical Research*, 7(6):654–657, 1990. doi: 10.1023/A:1015834715152.

[94] F. Doghieri and G. C. Sarti. Nonequilibrium lattice fluids: A predictive model for the solubility in glassy polymers. *Macromolecules*, 29(24):7885–7896, 1996. doi: 10.1021/ma951366c.

[95] G. C. Sarti and F. Doghieri. Predictions of the solubility of gases in glassy polymers based on the NELF model. *Chemical Engineering Science*, 53(19): 3435–3447, 1998. doi: 10.1016/S0009-2509(98)00143-2.

[96] F. Grassia, M. Giacinti Baschetti, F. Doghieri, and G. C. Sarti. Solubility of gases and vapors in glassy polymer blends. In I. Pinnau and B. D. Freeman, editors, *Advanced Materials for Membrane Separations*, volume 876, pages 55–73. American Chemical Society, 2004. ISBN 9780841238336.

[97] D. Borrmann, A. Danzer, and G. Sadowski. Water sorption in glassy polyvinylpyrrolidone-based polymers. *Membranes*, 12(4), 2022. doi: 10.3390/membranes12040434.

[98] D. Borrmann, A. Danzer, and G. Sadowski. Predicting the water sorption in ASDs. *Pharmaceutics*, 14(6):1181, 2022. doi: 10.3390/pharmaceutics14061181.

[99] B. Grönniger, E. Fritschka, I. Fahrig, A. Danzer, and G. Sadowski. Water sorption in rubbery and glassy polymers, nifedipine, and their ASDs. *Molecular Pharmaceutics*, 20(4):2194–2206, 2023. doi: 10.1021/acs.molpharmaceut.3c00006.

[100] L. De Carli and L. Larizza. Griseofulvin. *Mutation Research/Reviews in Genetic Toxicology*, 195(2):91–126, 1988. doi: 10.1016/0165-1110(88)90020-6.

[101] A. B. Petersen, M. H. Rønnest, T. O. Larsen, and M. H. Clausen. The chemistry of griseofulvin. *Chemical Reviews*, 114(24):12088–12107, 2014. doi: 10.1021/cr400368e.

[102] X. Ou, X. Li, H. Rong, L. Yu, and M. Lu. A general method for cultivating single crystals from melt microdroplets. *Chemical Communications*, 56(69):9950–9953, 2020. doi: 10.1039/d0cc03157g.

[103] T. G. Kantor. Ibuprofen. *Annals of Internal Medicine*, 91(6):877, 1979. doi: 10.7326/0003-4819-91-6-877.

[104] K. D. Rainsford. Ibuprofen: Pharmacology, efficacy and safety. *Inflammopharmacology*, 17(6):275–342, 2009. doi: 10.1007/s10787-009-0016-x.

[105] A. M. Evans. Comparative pharmacology of S(+)-ibuprofen and (RS)-ibuprofen. *Clinical Rheumatology*, 20(S1):9–14, 2001. doi: 10.1007/bf03342662.

[106] E. Dudognon, F. Danède, M. Descamps, and N. T. Correia. Evidence for a new crystalline phase of racemic ibuprofen. *Pharmaceutical Research*, 25(12): 2853–2858, 2008. doi: 10.1007/s11095-008-9655-7.

[107] G. Alván, M. Orme, L. Bertilsson, R. Ekstrand, and L. Palmér. Pharmacokinetics of indomethacin. *Clinical Pharmacology & Therapeutics*, 18(3):364–373, 1975. doi: 10.1002/cpt1975183364.

[108] M. O'Brien, J. McCauley, and E. Cohen. Indomethacin. *Analytical Profiles of Drug Substances*, 13:211–238, 1984. doi: 10.1016/s0099-5428(08)60192-6.

[109] S. Lucas. The pharmacology of indomethacin. *Headache: The Journal of Head and Face Pain*, 56(2):436–446, 2016. doi: 10.1111/head.12769.

[110] X. Ou, S. Li, Y. Chen, H. Rong, A. Li, and M. Lu. Polymorphism in griseofulvin: New story between an old drug and polyethylene glycol. *Crystal Growth & Design*, 22(6):3778–3785, 2022. doi: 10.1021/acs.cgd.2c00156.

[111] V. Štejfa, V. Pokorný, A. Mathers, K. Růžička, and M. Fulem. Heat capacities of selected active pharmaceutical ingredients. *The Journal of Chemical Thermodynamics*, 163:106585, 2021. doi: 10.1016/j.jct.2021.106585.

[112] K. J. Crowley and G. Zografi. Cryogenic grinding of indomethacin polymorphs and solvates: Assessment of amorphous phase formation and amorphous phase physical stability. *Journal of Pharmaceutical Sciences*, 91(2):492–507, 2002. doi: 10.1002/jps.10028.

[113] M. Lightowler, S. Li, X. Ou, X. Zou, M. Lu, and H. Xu. Indomethacin polymorph δ revealed to be two plastically bendable crystal forms by 3d electron diffraction: Correcting a 47-year-old misunderstanding. *Angewandte Chemie International Edition*, 61(7), 2022. doi: 10.1002/anie.202114985.

[114] J. S. Song and Y. T. Sohn. Crystal forms of naproxen. *Archives of Pharmacal Research*, 34(1):87–90, 2011. doi: 10.1007/s12272-011-0110-7.

[115] S. A. Surwase, J. P. Boetker, D. Saville, B. J. Boyd, K. C. Gordon, L. Peltonen, and C. J. Strachan. Indomethacin: New polymorphs of an old drug. *Molecular Pharmaceutics*, 10(12):4472–4480, 2013. doi: 10.1021/mp400299a.

[116] R. Maxwell and J. Chickos. An examination of the thermodynamics of fusion, vaporization, and sublimation of ibuprofen and naproxen by correlation gas chromatography. *Journal of Pharmaceutical Sciences*, 101(2):805–814, 2012. doi: 10.1002/jps.22803.

[117] P. A. Todd and S. P. Clissold. Naproxen a reappraisal of its pharmacology, and therapeutic use in rheumatic diseases and pain states. *Drugs*, 40(1):91–137, 1990. doi: 10.2165/00003495-199040010-00006.

[118] D. J. Angiolillo and S. M. Weisman. Clinical pharmacology and cardiovascular safety of naproxen. *American Journal of Cardiovascular Drugs*, 17(2):97–107, 2016. doi: 10.1007/s40256-016-0200-5.

[119] N. M. Davies and K. E. Anderson. Clinical pharmacokinetics of naproxen. *Clinical Pharmacokinetics*, 32(4):268–293, 1997. doi: 10.2165/00003088-199732040-00002.

[120] K. T. Wan and M. E. Davis. Asymmetric synthesis of naproxen by supported aqueous-phase catalysis. *Journal of Catalysis*, 148(1):1–8, 1994. doi: 10.1006/jcat.1994.1179.

[121] P. J. Harrington and E. Lodewijk. Twenty years of naproxen technology. *Organic Process Research & Development*, 1(1):72–76, 1997. doi: 10.1021/op960009e.

[122] M. W. Ha and S. M. Paek. Recent advances in the synthesis of ibuprofen and naproxen. *Molecules*, 26(16):4792, 2021. doi: 10.3390/molecules26164792.

[123] D. T. Turner and A. Schwartz. The glass transition temperature of poly(n-vinyl pyrrolidone) by differential scanning calorimetry. *Polymer*, 26(5):757–762, 1985. doi: 10.1016/0032-3861(85)90114-4.

[124] L. N. Bell. Investigations regarding the determination of glass transition temperatures from moisture sorption isotherms. *Drug Development and Industrial Pharmacy*, 21(14):1649–1659, 1995. doi: 10.3109/03639049509069254.

[125] B. C. Hancock, S. L. Shamblin, and G. Zografi. Molecular mobility of amorphous pharmaceutical solids below their glass transition temperatures. *Pharmaceutical Research*, 12(6):799–806, 1995. doi: 10.1023/A:1016292416526.

[126] T. Matsumoto and G. Zografi. Physical properties of solid molecular dispersions of indomethacin with poly(vinylpyrrolidone) and poly(vinylpyrrolidone-co-vinyl-acetate) in relation to indomethacin crystallization. *Pharmaceutical Research*, 16 (11):1722–1728, 1999. doi: 10.1023/A:1018906132279.

[127] J. Zhang and G. Zografi. The relationship between "BET" and "free volume"–derived parameters for water vapor absorption into amorphous solids. *Journal of Pharmaceutical Sciences*, 89(8):1063–1072, 2000. doi: 10.1002/1520-6017(200008)89:8⟨1063::AID-JPS11⟩3.0.CO;2-0.

[128] L. Tajber, O. I. Corrigan, and A. M. Healy. Physicochemical evaluation of PVP-thiazide diuretic interactions in co-spray-dried composites–analysis of glass transition composition relationships. *European Journal of Pharmaceutical Sciences*, 24(5):553–563, 2005. doi: 10.1016/j.ejps.2005.01.007.

[129] U. S. Kestur, H. Lee, D. Santiago, C. Rinaldi, Y.-Y. Won, and L. S. Taylor. Effects of the molecular weight and concentration of polymer additives, and temperature on the melt crystallization kinetics of a small drug molecule. *Crystal Growth & Design*, 10(8):3585–3595, 2010. doi: 10.1021/cg1004853.

[130] S. Mohapatra, S. Samanta, K. Kothari, P. Mistry, and R. Suryanarayanan. Effect of polymer molecular weight on the crystallization behavior of indomethacin amorphous solid dispersions. *Crystal Growth & Design*, 17(6):3142–3150, 2017. doi: 10.1021/acs.cgd.7b00096.

[131] M. Doreth, K. Löbmann, P. Priemel, H. Grohganz, R. Taylor, R. Holm, H. Lopez de Diego, and T. Rades. Influence of PVP molecular weight on the microwave assisted in situ amorphization of indomethacin. *European Journal of Pharmaceutics and Biopharmaceutics*, 122:62–69, 2018. doi: 10.1016/j.ejpb.2017.10.001.

[132] W. Liu, Y. H. Roos, and F. Fan. Physicochemical properties and relaxation time in strength analysis of amorphous poly (vinyl-pyrrolidone) and maltodextrin: Effects of water, molecular weight, and lactose addition. *Journal of Food Engineering*, 226:82–95, 2018. doi: 10.1016/j.jfoodeng.2018.01.020.

[133] J. Pacułt, M. Rams-Baron, B. Chrząszcz, R. Jachowicz, and M. Paluch. Effect of polymer chain length on the physical stability of amorphous drug-polymer blends at ambient pressure. *Molecular Pharmaceutics*, 15(7):2807–2815, 2018. doi: 10.1021/acs.molpharmaceut.8b00312.

[134] K. Sarpal, S. Delaney, G. G. Z. Zhang, and E. J. Munson. Phase behavior of amorphous solid dispersions of felodipine: Homogeneity and drug-polymer interactions. *Molecular Pharmaceutics*, 16(12):4836–4851, 2019. doi: 10.1021/acs.molpharmaceut.9b00731.

[135] I. Saraf, R. Roskar, D. Modhave, M. Brunsteiner, A. Karn, D. Neshchadin, G. Gescheidt, and A. Paudel. Forced solid-state oxidation studies of nifedipine-PVP amorphous solid dispersion. *Molecular Pharmaceutics*, 19(2):568–583, 2022. doi: 10.1021/acs.molpharmaceut.1c00678.

[136] Y. Sun, J. Tao, G. G. Z. Zhang, and L. Yu. Solubilities of crystalline drugs in polymers: An improved analytical method and comparison of solubilities of indomethacin and nifedipine in PVP, PVP/VA, and PVAc. *Journal of Pharmaceutical Sciences*, 99(9):4023–4031, 2010. doi: 10.1002/jps.22251.

[137] R. J. Chokshi, N. H. Shah, H. K. Sandhu, A. W. Malick, and H. Zia. Stabilization of low glass transition temperature indomethacin formulations: Impact of polymer-type and its concentration. *Journal of Pharmaceutical Sciences*, 97(6): 2286–2298, 2008. doi: 10.1002/jps.21174.

[138] C. P. Oliveira, Ribeiro, M. E. N. P., Ricardo, N. M. P. S., Souza, T. V. de P., C. L. Moura, C. Chaibundit, S. G. Yeates, K. Nixon, and D. Attwood. The effect of water-soluble polymers, PEG and PVP, on the solubilisation of griseofulvin in aqueous micellar solutions of Pluronic F127. *International Journal of Pharmaceutics*, 421(2):252–257, 2011. doi: 10.1016/j.ijpharm.2011.10.010.

[139] L. Malaj, R. Censi, M. Mozzicafreddo, L. Pellegrino, M. Angeletti, R. Gobetto, and P. Di Martino. Influence of relative humidity on the interaction between different aryl propionic acid derivatives and poly(vinylpyrrolydone) K30: Evaluation of the effect on drug bioavailability. *International Journal of Pharmaceutics*, 398(1-2):61–72, 2010. doi: 10.1016/j.ijpharm.2010.07.024.

[140] A. C. F. Rumondor, H. Konno, P. J. Marsac, and L. S. Taylor. Analysis of the moisture sorption behavior of amorphous drug-polymer blends. *Journal of Applied Polymer Science*, 117(2):1055–1063, 2010. doi: 10.1002/app.31803.

[141] H. Ueda, S. Aikawa, Y. Kashima, J. Kikuchi, Y. Ida, T. Tanino, K. Kadota, and Y. Tozuka. Anti-plasticizing effect of amorphous indomethacin induced by specific intermolecular interactions with PVA copolymer. *Journal of Pharmaceutical Sciences*, 103(9):2829–2838, 2014. doi: 10.1002/jps.24023.

[142] A. Prudic, Y. Ji, C. Luebbert, and G. Sadowski. Influence of humidity on the phase behavior of API/polymer formulations. *European Journal of Pharmaceutics and Biopharmaceutics*, 94:352–362, 2015. doi: 10.1016/j.ejpb.2015.06.009.

[143] V. Bühler. *Polyvinylpyrrolidone excipients for pharmaceuticals: Povidone, crospovidone and copovidone.* Springer, Berlin and Heidelberg, 2005. ISBN 3-540-23412-8.

[144] F. Haaf, A. Sanner, and F. Straub. Polymers of n-vinylpyrrolidone: Synthesis, characterization and uses. *Polymer Journal*, 17(1):143–152, 1985. doi: 10.1295/polymj.17.143.

[145] B. V. Robinson, F. M. Sullivan, J. F. Borzelleca, and S. L. Schwartz. *PVP: A critical review of the kinetics and toxicology of polyvinylpyrrolidone (Povidone).* Routledge, 2018. ISBN 9780203741672.

[146] M. S. Shin, J. H. Lee, and H. Kim. Phase behavior of the poly(vinyl pyrrolidone) + dichloromethane + supercritical carbon dioxide system. *Fluid Phase Equilibria*, 272(1-2):42–46, 2008. doi: 10.1016/j.fluid.2008.07.016.

[147] K. Adrjanowicz, Z. Wojnarowska, M. Paluch, and J. Pionteck. Thermodynamic scaling of molecular dynamics in supercooled ibuprofen. *The Journal of Physical Chemistry*, 115(16):4559–4567, 2011. doi: 10.1021/jp109135w.

[148] P. Zoller, P. Bolli, V. Pahud, and H. Ackermann. Apparatus for measuring pressure-volume-temperature relationships of polymers to 350 degrees C and 2200kg/cm2. *The Review of Scientific Instruments*, 47(8):948–952, 1976. doi: 10.1063/1.1134779.

[149] S. Gracin and Å. C. Rasmuson. Solubility of phenylacetic acid, p-hydroxyphenylacetic acid, p-aminophenylacetic acid, p-hydroxybenzoic acid, and ibuprofen in pure solvents. *Journal of Chemical & Engineering Data*, 47(6):1379–1383, 2002. doi: 10.1021/je0255170.

[150] S. Zhao, Y. Ma, J. Gong, B. Hou, and W. Tang. Solid-liquid phase equilibrium and thermodynamic analysis of griseofulvin in twelve mono-solvents. *Journal of Molecular Liquids*, 296:111861, 2019. doi: 10.1016/j.molliq.2019.111861.

[151] D. P. Pacheco and F. Martínez. Thermodynamic analysis of the solubility of naproxen in ethanol + water cosolvent mixtures. *Physics and Chemistry of Liquids*, 45(5):581–595, 2007. doi: 10.1080/00319100701313862.

[152] C. P. Mora and F. Martínez. Solubility of naproxen in several organic solvents at different temperatures. *Fluid Phase Equilibria*, 255(1):70–77, 2007. doi: 10.1016/j.fluid.2007.03.029.

[153] M. A. Ruidiaz, D. R. Delgado, F. Martínez, and Y. Marcus. Solubility and preferential solvation of indomethacin in 1,4-dioxane+water solvent mixtures. *Fluid Phase Equilibria*, 299(2):259–265, 2010. doi: 10.1016/j.fluid.2010.09.027.

[154] F. Martínez, M. A. Peña, and P. Bustamante. Thermodynamic analysis and enthalpy–entropy compensation for the solubility of indomethacin in aqueous and non-aqueous mixtures. *Fluid Phase Equilibria*, 308(1-2):98–106, 2011. doi: 10.1016/j.fluid.2011.06.016.

[155] R. Paus, Y. Ji, F. Braak, and G. Sadowski. Dissolution of crystalline pharmaceuticals: Experimental investigation and thermodynamic modeling. *Industrial & Engineering Chemistry Research*, 54(2):731–742, 2015. doi: 10.1021/ie503939w.

[156] J. Østergaard. *UV/Vis spectrophotometry and UV imaging*, pages 3–27. Springer New York, 2016. ISBN 9781493940295.

[157] A. Pobudkowska, U. Domańska, B. A. Jurkowska, and K. Dymczuk. Solubility of pharmaceuticals in water and alcohols. *Fluid Phase Equilibria*, 392:56–64, 2015. doi: 10.1016/j.fluid.2015.02.018.

[158] M. del P. Buera, G. Levi, and M. Karel. Glass transition in poly(vinylpyrrolidone): Effect of molecular weight and diluents. *Biotechnology Progress*, 8(2):144–148, 1992. doi: 10.1021/bp00014a008.

[159] V. Andronis, M. Yoshioka, and G. Zografi. Effects of sorbed water on the crystallization of indomethacin from the amorphous state. *Journal of Pharmaceutical Sciences*, 86(3):346–351, 1997. doi: 10.1021/js9602711.

[160] S. Fitzpatrick, J. F. McCabe, C. R. Petts, and S. W. Booth. Effect of moisture on polyvinylpyrrolidone in accelerated stability testing. *International Journal of Pharmaceutics*, 246(1-2):143–151, 2002. doi: 10.1016/S0378-5173(02)00375-7.

[161] S. Hasegawa, T. Hamaura, N. Furuyama, A. Kusai, E. Yonemochi, and K. Terada. Effects of water content in physical mixture and heating temperature on crystallinity of troglitazone-PVP K30 solid dispersions prepared by closed melting method. *International Journal of Pharmaceutics*, 302(1-2):103–112, 2005. doi: 10.1016/j.ijpharm.2005.06.021.

[162] R. D. Saklatvala, M. H. Saunders, S. Fitzpatrick, and G. Buckton. A comparison of high speed differential scanning calorimetry (Hyper-DSC) and modulated differential scanning calorimetry to detect the glass transition of polyvinylpyrrolidone: The effect of water content and detection sensitivity in powder mixtures (a model formulation). *Journal of Drug Delivery Science and Technology*, 15(4): 257–260, 2005. doi: 10.1016/S1773-2247(05)50046-7.

[163] G. W. H. Höhne, W. F. Hemminger, and H.-J. Flammersheim. *Differential scanning calorimetry*. Springer Berlin Heidelberg, 2003. ISBN 9783662067109.

[164] Q. Zheng, Y. Zhang, M. Montazerian, O. Gulbiten, J. C. Mauro, E. D. Zanotto, and Y. Yue. Understanding glass through differential scanning calorimetry. *Chemical Reviews*, 119(13):7848–7939, 2019. doi: 10.1021/acs.chemrev.8b00510.

[165] I. M. Hodge. Enthalpy relaxation and recovery in amorphous materials. *Journal of Non-Crystalline Solids*, 169(3):211–266, 1994. doi: 10.1016/0022-3093(94) 90321-2.

[166] P. S. Gill, S. R. Sauerbrunn, and M. Reading. Modulated differential scanning calorimetry. *Journal of Thermal Analysis*, 40(3):931–939, 1993. doi: 10.1007/BF02546852.

[167] A. R. Brás, J. P. Noronha, A. M. M. Antunes, M. M. Cardoso, A. Schönhals, F. Affouard, M. Dionísio, and N. T. Correia. Molecular motions in amorphous ibuprofen as studied by broadband dielectric spectroscopy. *The Journal of Physical Chemistry*, 112(35):11087–11099, 2008. doi: 10.1021/jp8040428.

[168] Z. Wojnarowska, K. Adrjanowicz, P. Wlodarczyk, E. Kaminska, K. Kaminski, K. Grzybowska, R. Wrzalik, M. Paluch, and K. L. Ngai. Broadband dielectric relaxation study at ambient and elevated pressure of molecular dynamics of pharmaceutical: Indomethacin. *The Journal of Physical Chemistry*, 113(37): 12536–12545, 2009. doi: 10.1021/jp905162r.

[169] K. Adrjanowicz, K. Kaminski, Z. Wojnarowska, M. Dulski, L. Hawelek, S. Pawlus, M. Paluch, and W. Sawicki. Dielectric relaxation and crystallization kinetics of ibuprofen at ambient and elevated pressure. *The Journal of Physical Chemistry*, 114(19):6579–6593, 2010. doi: 10.1021/jp910009b.

[170] K. Kothari, V. Ragoonanan, and R. Suryanarayanan. Influence of molecular mobility on the physical stability of amorphous pharmaceuticals in the supercooled and glassy states. *Molecular Pharmaceutics*, 11(9):3048–3055, 2014. doi: 10.1021/mp500229d.

[171] T. Cordeiro, A. F. M. Santos, G. Nunes, G. Cunha, J. C. Sotomayor, I. M. Fonseca, F. Danède, C. J. Dias, M. M. Cardoso, N. T. Correia, M. T. Viciosa, and M. Dionísio. Accessing the physical state and molecular mobility of naproxen

confined to nanoporous silica matrixes. *The Journal of Physical Chemistry C*, 120(26):14390–14401, 2016. doi: 10.1021/acs.jpcc.6b04078.

[172] K. Grzybowska, S. Capaccioli, and M. Paluch. Recent developments in the experimental investigations of relaxations in pharmaceuticals by dielectric techniques at ambient and elevated pressure. *Advanced Drug Delivery Reviews*, 100:158–182, 2016. doi: 10.1016/j.addr.2015.12.008.

[173] L. R. Ochs, M. Kabiri-badr, and H. Cabezas. An improved isopiestic method to determine activities in multicomponent mixtures. *AIChE Journal*, 36(12): 1908–1912, 1990. doi: 10.1002/aic.690361216.

[174] R. Sadeghi and M. Taghi Zafarani-Moattar. Thermodynamics of aqueous solutions of polyvinylpyrrolidone. *The Journal of Chemical Thermodynamics*, 36(8): 665–670, 2004. doi: 10.1016/j.jct.2004.04.008.

[175] K. S. Pitzer, editor. *Activity coefficients in electrolyte solutions.* CRC Press, 1991. ISBN 0849354153.

[176] E. J. Le Fevre, M. R. Nightingale, and J. W. Rose. The second virial coefficient of ordinary water substance: A new correlation. *Journal of Mechanical Engineering Science*, 17(5):243–251, 1975. doi: 10.1243/jmes_jour_1975_017_036_02.

[177] G. S. Kell. Density, thermal expansivity, and compressibility of liquid water from 0 deg to 150 deg. correlations and tables for atmospheric pressure and saturation reviewed and expressed on 1968 temperature scale. *Journal of Chemical & Engineering Data*, 20(1):97–105, 1975. doi: 10.1021/je60064a005.

[178] A. Wexler and L. Greenspan. Vapor pressure equation for water in the range 0 to 100 C. *Journal of Research of the National Bureau of Standards Section A*, 75A(3):213, 1971. doi: 10.6028/jres.075a.022.

[179] K. J. Dawson, K. L. Kearns, M. D. Ediger, M. J. Sacchetti, and G. D. Zografi. Highly stable indomethacin glasses resist uptake of water vapor. *The Journal of Physical Chemistry B*, 113(8):2422–2427, 2009. doi: 10.1021/jp808838t.

[180] D. Borrmann, A. Danzer, and G. Sadowski. Measuring and modeling water sorption in amorphous indomethacin and ritonavir. *Molecular Pharmaceutics*, 19 (3):998–1007, 2022. doi: 10.1021/acs.molpharmaceut.1c00984.

[181] M. J. Kontny, G. P. Grandolfi, and G. Zografi. *Pharmaceutical Research*, 04(2): 104–112, 1987. doi: 10.1023/a:1016458701059.

[182] R. H. Lacombe and I. C. Sanchez. Statistical thermodynamics of fluid mixtures. *The Journal of Physical Chemistry*, 80(23):2568–2580, 1976. doi: 10.1021/j100564a009.

[183] R. K. Pathria. *Statistical mechanics*, volume 45. Pergamon Press, 1993. ISBN 0080167470.

[184] M. B. Lewis and A. J. F. Siegert. Extension of the condensation theory of Yang and Lee to the pressure ensemble. *Physical Review*, 101(4):1227–1233, 1956. doi: 10.1103/physrev.101.1227.

[185] K. von Konigslow, C. B. Park, and R. B. Thompson. Polymeric foaming predictions from the Sanchez-Lacombe equation of state: Application to polypropylene-carbon dioxide mixtures. *Physical Review Applied*, 8(4), 2017. doi: 10.1103/PhysRevApplied.8.044009.

[186] N. Koak and R. A. Heidemann. Phase boundary calculations for solutions of a polydisperse polymer. *AIChE Journal*, 47(5):1219–1225, 2001. doi: 10.1002/aic.690470528.

[187] Y. Xiong and E. Kiran. Prediction of high-pressure phase behaviour in polyethylene/n-pentane/carbon dioxide ternary system with the sanchez-lacombe model. *Polymer*, 35(20):4408–4415, 1994. doi: 10.1016/0032-3861(94)90100-7.

[188] J. P. O'Connell and J. M. Haile. *Thermodynamics*. Cambridge University Press, 2012. ISBN 9780521588188.

[189] J. A. Nelder and R. Mead. A simplex method for function minimization. *The Computer Journal*, 7(4):308–313, 1965. doi: 10.1093/comjnl/7.4.308.

[190] K. Adrjanowicz, A. Grzybowski, K. Grzybowska, J. Pionteck, and M. Paluch. Toward better understanding crystallization of supercooled liquids under compression: Isochronal crystallization kinetics approach. *Crystal Growth & Design*, 13(11):4648–4654, 2013. doi: 10.1021/cg401274p.

[191] F. Y. Yan, L. Chen, D. Q. Liu, L. F. SiMa, M. J. Chen, H. Shi, and J. X. Zhu. Solubility of (+)-(S)-2-(6-methoxynaphthalen-2-yl) propanoic acid in acetone, methanol, ethanol, propan-2-ol, and ethyl ethanoate at temperatures between (278 and 320) K. *Journal of Chemical & Engineering Data*, 54(3):1117–1119, 2009. doi: 10.1021/je8008039.

[192] L. Zhu, J. Jona, K. Nagapudi, and T. Wu. Fast surface crystallization of amorphous griseofulvin below Tg. *Pharmaceutical Research*, 27(8):1558–1567, 2010. doi: 10.1007/s11095-010-0140-8.

[193] J. A. Baird, B. van Eerdenbrugh, and L. S. Taylor. A classification system to assess the crystallization tendency of organic molecules from undercooled melts. *Journal of Pharmaceutical Sciences*, 99(9):3787–3806, 2010. doi: 10.1002/jps.22197.

[194] A. Forster, J. Hempenstall, I. Tucker, and T. Rades. Selection of excipients for melt extrusion with two poorly water-soluble drugs by solubility parameter calculation and thermal analysis. *International Journal of Pharmaceutics*, 226 (1-2):147–161, 2001. doi: 10.1016/S0378-5173(01)00801-8.

[195] S. Wang, Z. Song, J. Wang, Y. Dong, and M. Wu. Solubilities of ibuprofen in different pure solvents. *Journal of Chemical & Engineering Data*, 55(11):5283–5285, 2010. doi: 10.1021/je100255z.

[196] D. R. Stull. Vapor pressure of pure substances. Organic and inorganic Compounds. *Industrial & Engineering Chemistry*, 39(4):517–540, 1947. doi: 10.1021/ie50448a022.

[197] J. C. Rintelen, J. H. Saylor, and P. M. Gross. The densities and vapor pressures of some alkylbenzenes, aliphatic ketones and n-amyl chloride 1. *Journal of the American Chemical Society*, 59(6):1129–1130, 1937. doi: 10.1021/ja01285a050.

[198] E. T. J. Fuge, S. T. Bowden, and W. J. Jones. Some physical properties of diacetone alcohol, mesityl oxide and methyl isobutyl ketone. *The Journal of Physical Chemistry*, 56(8):1013–1016, 1952. doi: 10.1021/j150500a022.

[199] S. Wang, J. Wang, and Q. Yin. Measurement and correlation of solubility of 7-aminocephalosporanic acid in aqueous acetone mixtures. *Industrial & Engineering Chemistry Research*, 44(10):3783–3787, 2005. doi: 10.1021/ie048938e.

[200] A. Bejarano, N. Quezada, and J. C. de La Fuente. Complementary vapor pressure data for 2-methyl-1-propanol and 3-methyl-1-butanol at a pressure range of (15 to 177)kPa. *The Journal of Chemical Thermodynamics*, 41(9):1020–1024, 2009. doi: 10.1016/j.jct.2009.04.009.

[201] G. V. Stepanov, A. R. Rasulov, K. A. Shakhbanov, and L. M. Radzhabova. Phase coexistence curve for isobutanol. *High Temperature*, 39(2):322–324, 2001. doi: 10.1023/A:1017595421248.

[202] S. I. Sandler, editor. *Models for thermodynamic and phase equilibria calculations*, volume 52. Dekker, 1994. ISBN 0824791304.

[203] C. Panayiotou and I. C. Sanchez. Hydrogen bonding in fluids: An equation-of-state approach. *The Journal of Physical Chemistry*, 95(24):10090–10097, 1991. doi: 10.1021/j100177a086.

[204] M. E. Donaldson, L. C. Draucker, V. Blasucci, C. L. Liotta, and C. A. Eckert. Liquid–liquid equlibria of polyethylene glycol (PEG) 400 and CO2 with common organic solvents. *Fluid Phase Equilibria*, 277(2):81–86, 2009. doi: 10.1016/j.fluid.2008.11.003.

[205] A. O. Onyekweli and N. Pilpel. Effect of temperature changes on the densification and compression of griseofulvin and sucrose powders. *The Journal of Pharmacy and Pharmacology*, 33(6):377–381, 1981. doi: 10.1111/j.2042-7158.1981.tb13808.x.

[206] D. Zhou, G. G. Z. Zhang, D. Law, D. J. W. Grant, and E. A. Schmitt. Thermodynamics, molecular mobility and crystallization kinetics of amorphous griseofulvin. *Molecular Pharmaceutics*, 5(6):927–936, 2008. doi: 10.1021/mp800169g.

[207] H. Al-Obaidi and G. Buckton. Evaluation of griseofulvin binary and ternary solid dispersions with HPMCAS. *AAPS PharmSciTech*, 10(4):1172–1177, 2009. doi: 10.1208/s12249-009-9319-x.

[208] Q. Shi, C. Zhang, Y. Su, J. Zhang, D. Zhou, and T. Cai. Acceleration of crystal growth of amorphous griseofulvin by low-concentration poly(ethylene oxide): Aspects of crystallization kinetics and molecular mobility. *Molecular Pharmaceutics*, 14(7):2262–2272, 2017. doi: 10.1021/acs.molpharmaceut.7b00097.

[209] W. Tu, J. Knapik-Kowalczuk, K. Chmiel, and M. Paluch. Glass transition dynamics and physical stability of amorphous griseofulvin in binary mixtures with low-Tg excipients. *Molecular Pharmaceutics*, 16(8):3626–3635, 2019. doi: 10.1021/acs.molpharmaceut.9b00476.

[210] E. Tombari, S. Presto, G. P. Johari, and R. M. Shanker. Molecular mobility, thermodynamics and stability of griseofulvin's ultraviscous and glassy states from dynamic heat capacity. *Pharmaceutical Research*, 25(4):902–912, 2008. doi: 10.1007/s11095-007-9444-8.

[211] J. F. Willart, L. Carpentier, F. Danède, and M. Descamps. Solid-state vitrification of crystalline griseofulvin by mechanical milling. *Journal of Pharmaceutical Sciences*, 101(4):1570–1577, 2012. doi: 10.1002/jps.23041.

[212] G. P. Johari, S. Kim, and R. M. Shanker. Dielectric relaxation and crystallization of ultraviscous melt and glassy states of aspirin, ibuprofen, progesterone, and quinidine. *Journal of Pharmaceutical Sciences*, 96(5):1159–1175, 2007. doi: 10.1002/jps.20921.

[213] A. R. Brás, M. Dionísio, N. T. Correia, M. Tokuyama, I. Oppenheim, and H. Nishiyama. Molecular motions in amorphous pharmaceuticals. In *AIP Conference Proceedings*, pages 91–96, 2008. doi: 10.1063/1.2897912.

[214] J. J. M. Ramos, R. Taveira-Marques, and H. P. Diogo. Estimation of the fragility index of indomethacin by DSC using the heating and cooling rate dependency of the glass transition. *Journal of Pharmaceutical Sciences*, 93(6):1503–1507, 2004. doi: 10.1002/jps.20061.

[215] S. Vyazovkin and I. Dranca. Physical stability and relaxation of amorphous indomethacin. *The Journal of Physical Chemistry*, 109(39):18637–18644, 2005. doi: 10.1021/jp052985i.

[216] T. Wu and L. Yu. Surface crystallization of indomethacin below Tg. *Pharmaceutical Research*, 23(10):2350–2355, 2006. doi: 10.1007/s11095-006-9023-4.

[217] P. Karmwar, J. P. Boetker, K. A. Graeser, C. J. Strachan, J. Rantanen, and T. Rades. Investigations on the effect of different cooling rates on the stability of amorphous indomethacin. *European Journal of Pharmaceutical Sciences*, 44(3):341–350, 2011. doi: 10.1016/j.ejps.2011.08.010.

[218] P. Karmwar, K. Graeser, K. C. Gordon, C. J. Strachan, and T. Rades. Investigation of properties and recrystallisation behaviour of amorphous indomethacin samples prepared by different methods. *International Journal of Pharmaceutics*, 417(1-2):94–100, 2011. doi: 10.1016/j.ijpharm.2010.12.019.

[219] C. A. Angell. Formation of glasses from liquids and biopolymers. *Science*, 267(5206):1924–1935, 1995. doi: 10.1126/science.267.5206.1924.

[220] S. Bauer, M. Storek, C. Gainaru, H. Zimmermann, and R. Böhmer. Molecular motions in supercooled and glassy ibuprofen: Deuteron magnetic resonance and high-resolution rheology study. *The Journal of Physical Chemistry*, 119(15):5087–5095, 2015. doi: 10.1021/acs.jpcb.5b01072.

[221] C. A. Angell. Entropy and fragility in supercooling liquids. *Journal of Research of the National Institute of Standards and Technology*, 102(2):171–185, 1997. doi: 10.6028/jres.102.013.

[222] L. Carpentier, R. Decressain, S. Desprez, and M. Descamps. Dynamics of the amorphous and crystalline alpha-, gamma-phases of indomethacin. *The Journal of Physical Chemistry*, 110(1):457–464, 2006. doi: 10.1021/jp053545u.

[223] S. Cerveny, A. Alegría, and J. Colmenero. Broadband dielectric investigation on poly(vinyl pyrrolidone) and its water mixtures. *The Journal of Chemical Physics*, 128(4):044901, 2008. doi: 10.1063/1.2822332.

[224] A. Mansuri, M. Völkel, T. Feuerbach, J. Winck, A. W. P. Vermeer, W. Hoheisel, and M. Thommes. Modified free volume theory for self-diffusion of small molecules in amorphous polymers. *Macromolecules*, 56(8):3224–3237, 2023. doi: 10.1021/acs.macromol.2c02451.

[225] A. Mansuri, M. Völkel, D. Mihiranga, T. Feuerbach, J. Winck, A. W. P. Vermeer, W. Hoheisel, and M. Thommes. Predicting self-diffusion coefficients in semi-crystalline and amorphous solid dispersions using free volume theory. *European Journal of Pharmaceutics and Biopharmaceutics*, 190:107–120, 2023. doi: 10.1016/j.ejpb.2023.07.001.

[226] K. F. Kelton. Kinetic and structural fragility—a correlation between structures and dynamics in metallic liquids and glasses. *Journal of Physics - Condensed Matter*, 29(2):023002, 2016. doi: 10.1088/0953-8984/29/2/023002.

[227] C. M. Roland, S. Hensel-Bielowka, M. Paluch, and R. Casalini. Supercooled dynamics of glass-forming liquids and polymers under hydrostatic pressure. *Reports on Progress in Physics*, 68(6):1405–1478, 2005. doi: 10.1088/0034-4885/68/6/r03.

[228] D. Tabor. Micromolecular processes in the viscous flow of hydrocarbons. *Philosophical Magazine A*, 57(2):217–224, 1988. doi: 10.1080/01418618808204511.

[229] M. Vasanthavada, W. Q. Tong, Y. Joshi, and M. S. Kislalioglu. Phase behavior of amorphous molecular dispersions II: Role of hydrogen bonding in solid solubility and phase separation kinetics. *Pharmaceutical Research*, 22(3):440–448, 2005. doi: 10.1007/s11095-004-1882-y.

[230] C. C. Sun. A novel method for deriving true density of pharmaceutical solids including hydrates and water-containing powders. *Journal of Pharmaceutical Sciences*, 93(3):646–653, 2004. doi: 10.1002/jps.10595.

[231] P. J. Marsac, T. Li, and L. S. Taylor. Estimation of drug-polymer miscibility and solubility in amorphous solid dispersions using experimentally determined interaction parameters. *Pharmaceutical Research*, 26(1):139–151, 2009. doi: 10.1007/s11095-008-9721-1.

[232] P. Tong and G. Zografi. Solid-state characteristics of amorphous sodium indomethacin relative to its free acid. *Pharmaceutical Research*, 16(8):1186–1192, 1999. doi: 10.1023/a:1018985110956.

[233] P. J. Marsac, S. L. Shamblin, and L. S. Taylor. Theoretical and practical approaches for prediction of drug-polymer miscibility and solubility. *Pharmaceutical Research*, 23(10):2417–2426, 2006. doi: 10.1007/s11095-006-9063-9.

[234] M. M. Knopp, L. Tajber, Y. Tian, N. E. Olesen, D. S. Jones, A. Kozyra, K. Löbmann, K. Paluch, C. M. Brennan, R. Holm, A. M. Healy, G. P. Andrews, and T. Rades. Comparative study of different methods for the prediction of drug-polymer solubility. *Molecular Pharmaceutics*, 12(9):3408–3419, 2015. doi: 10.1021/acs.molpharmaceut.5b00423.

[235] *VDI-Wärmeatlas*. Springer Berlin Heidelberg, 2006. ISBN 9783540322184.

[236] C. A. Angell and J. C. Tucker. Heat capacity changes in glass-forming aqueous solutions and the glass transition in vitreous water. *The Journal of Physical Chemistry*, 84(3):268–272, 1980. doi: 10.1021/j100440a009.

[237] J. Teng, S. Bates, D. A. Engers, K. Leach, P. Schields, and Y. Yang. Effect of water vapor sorption on local structure of poly(vinylpyrrolidone). *Journal of Pharmaceutical Sciences*, 99(9):3815–3825, 2010. doi: 10.1002/jps.22204.

[238] N. G. Patel and A. T. M. Serajuddin. Moisture sorption by polymeric excipients commonly used in amorphous solid dispersion and its effect on glass transition temperature: I. polyvinylpyrrolidone and related copolymers. *International Journal of Pharmaceutics*, 616:121532, 2022. doi: 10.1016/j.ijpharm.2022.121532.

[239] R. Paus, Y. Ji, L. Vahle, and G. Sadowski. Predicting the solubility advantage of amorphous pharmaceuticals: A novel thermodynamic approach. *Molecular Pharmaceutics*, 12(8):2823–2833, 2015. doi: 10.1021/mp500824d.